The effect of the heating rate on the phase selection in Al/Ni multilayers

Zur Erlangung des akademischen Grades eines
Doktors der Ingenieurwissenschaften (Dr.-Ing.)
von der KIT-Fakultät für Maschinenbau des
Karlsruher Instituts für Technologie (KIT)

genehmigte
Dissertation
von

M.Sc. Tobias Neuhauser

Tag der mündlichen Prüfung:	26.11.2021
Referent:	apl. Prof. Dr.-Ing. Marc Kamlah
Korreferentin:	Prof. Dr.-Ing. habil. Bronislava Gorr

Dedicated to Anne & Willi

Kurzfassung

Die vorliegende Arbeit untersucht den Einfluss von Heizraten bis $10^6\,\mathrm{K\,s^{-1}}$ auf die Bildung von intermetallischen Phasen in Al/Ni-Multilagen. Das Ziel ist ein mechanismenbasiertes Verständnis der Phasenbildungprozessen als Grundlage für die Entwicklung von neuartigen Nano-Kompositmaterialien.

Für diesen Zweck wird eine *in situ* Untersuchungsmethode entwickelt, die eine thermodynamische und strukturelle Charakterisierung während der schnell ablaufenden Reaktionen ermöglicht. Durch die Kombination von chipbasierter Nanokalorimetrie mit Synchrotron-Röntgenbeugung wird eine Zeitauflösung von 15 µs erreicht.

Drei Aspekte von Al/Ni-Reaktionen werden in dieser Arbeit detailliert untersucht: (i) die Festkörperreaktionen bei Heizraten unter $500\,\mathrm{K\,s^{-1}}$, (ii) das Zündverhalten des Materialsystems und (iii) die Phasenbildung bei selbstfortschreitenden Reakionen. In Abhängigkeit von der Heizrate und der Temperatur kann gezielt die Bildung von Al_9Ni_2, Al_3Ni und Al_3Ni_2 iniitiert werden. Erstmalig wird der Zündpunkt von Al/Ni-Multilagen auf thermodynamischer Grundlage bestimmt und darauf basierend ein neues Kriterium für die Zündtemperatur abgeleitet. Es werden drei verschiedene Arten von selbsfortschreitenden Reaktionen beobachtet: (i) Flüssigphasen-Umwandlung, (ii) Flüssigphasen-Umwandlung mit Zwischenschicht und (iii) Festkörper-Umwandlung. Die Letztere kann zum ersten Mal in Multilagenmaterialien nachgewiesen werden.

Abstract

The present study investigates the effect of heating rates up to 10^6 $\mathrm{K\,s^{-1}}$ on the formation behaviour of intermetallic phases in Al/Ni multilayers. The objective is a mechanism-based understanding of the phase formation processes as a basis for the development of new types of nanocomposite materials.

For this purpose, an *in situ* method is developed which allows for a thermodynamic and structural characterisation during the rapid reactions. By combining chip-based nanocalorimetry with synchrotron X-ray diffraction a temporal resolution of 15 µs is achieved.

Three different aspects of Al/Ni reactions are investigated in detail: (i) solid-state reactions at heating rates below 500 $\mathrm{K\,s^{-1}}$, (ii) the ignition behaviour and (iii) the phase formation in runaway reactions. Depending on the heating rate and the temperature, the formation of Al_9Ni_2, Al_3Ni and Al_3Ni_2 can be addressed. For the first time, the ignition point of Al/Ni multilayers is determined on a thermodynamic basis which enables us to derive a new criterion for the ignition. Three different types of self-propagating reactions are observed: (i) liquid-state runaway reactions, (ii) liquid-state runaway reactions with compound layer and (iii) solid-state runaway reactions. The latter are documented in Al/Ni multilayers for the first time.

Acknowledgement

What is the objective of writing a doctoral thesis? In the beginning, I would have answered this question with an 'intellectual challenge'. After more than 4 years of intensive work, I can answer this question in a more differentiated way. Writing a doctoral thesis is: finding the question, being humble with the complexity of nature, getting to know your limits, meeting the brightest minds, being wrong and appreciating helpful people. Especially the last point is essential. For this reason, I want to take the chance to thank some people who have contributed significantly to the success of my doctoral thesis.

First, I want to thank my reviewers apl. Prof. Dr.-Ing. Marc Kamlah and Prof. Dr.-Ing. habil. Bronislava Gorr. I highly appreciate your advice and support regarding my work. A special thanks goes to my group lead Dr. Karsten Woll, for the extensive support in numerous ways. Without your scientific expertise, unconditional support in hard times and the sleepless nights at the synchrotron, the dissertation would not have been possible. I appreciate this very much. Furthermore, I gratefully acknowledge the financial support of the German Research Foundation (DFG) within the Emmy-Noether-Program (funding number: WO 2198/1-1).

Thank you to the IAM-WBM as the best institute in the world. Besides all the great people working here, I want to highlight Prof. Dr. mont. Christoph Kirchlechner and Jana Herzog. Thank you for being helpful all the time and creating this great working environment. Thank you to all my colleagues at the IAM-WBM. Good work is only possible with very good people, and you

are the best. You have the primary responsibility that I had a wonderful time at the institute. Special thanks to Markus Short for all the profound and unbelievably funny conversations with you. Thank you to all technical employees who contributed to the work. With the fabrication of the experimental setup, Ewald Ernst, Klaus Baumann and Peter Schöck made a precious contribution to the success of this doctoral thesis. Thank you, Joris Müller for writing an excellent bachelor thesis in our group.

Thank you to Prof. Timothy Weihs and Shane Quinlan Arlington. The two months at Johns Hopkins University in Baltimore were scientifically and personally very inspiring for me. Thank you for making this possible.

Thank you to all my friends in Karlsruhe. I shared so many great moments with you that I do not want to miss. Thank you for the backing in this sometimes challenging time. Special thanks to Nikolai Zimber whom I can always rely on.

Greatest gratitude goes to my whole family, especially to my mother Margit and my father Dieter. You paved the way for the success of this doctoral thesis in so many ways. Thank you for believing in me for 31 years. Thank you to my brother Bastian not only for the ultra-fast proofreading but also for all your inspiring thoughts.

Finally, I want to thank my wife Anne and my son Willi. Without your love, support and motivation, this work would never have been finished. You are the most important in my life. This work is dedicated to you.

Karlsruhe, September 2021 *Tobias Neuhauser*

Symbols

Symbol	Description
2θ	X-ray diffraction angle
α	Extend of conversion
A	Area
A_c	Area cross-section
A_{ab}	Absorption factor
B_{DW}	Debye-Waller factor
$B_{air,0-1}$	Sensor heat capacity constant $0-1$ (air)
$B_{vac,0-1}$	Sensor heat capacity constant $0-1$ (vacuum)
c	Composition
c_{com}	Composition of the compound phases
c_{eff}	Effective concentration
c_{range}	Fractional concentration of a phase
∇c	Concentration gradient
C_ε	Pyrometer constant
C_P	Heat capacity
$C_{P,rct}$	Heat capacity reaction
$C_{P,sample}$	Heat capacity sample
$C_{P,sensor}$	Heat capacity sensor
$C_{P,total}$	Total heat capacity
d	Thickness sensor membrane
d_{sample}	Thickness sample
ΔG	Gibbs free energy

ΔG_γ	Gibbs free surface energy
ΔG_s	Gibbs free strain energy
ΔG_V	Gibbs free volume energy
ε	Infrared emissivity
E_{beam}	X-ray beam energy
E_X	Extinction factor
$f(\alpha)$	Reaction model
f_{XRD}	X-ray acquisition rate
$\mid F(hkl) \mid^2$	Structure factor
$h(P)$	Kinetic pressure constant
H	Relative number of diffraction planes
$\Delta H_f^{'}$	Effective heat of formation
ΔH_f	Heat of formation
ΔH_{rx}	Heat of reaction
I	Current
I_{hkl}	Diffracted X-ray intensity of the hkl plane
I_0	Incoming X-ray intensity
I^+	Current +
I^-	Current -
I_{XRD}	X-ray peak intensity
j	Diffusion flux
$k(T)$	Kinetic rate constant
K_{cond}	Conductive heat loss coefficient
K_{rad}	Radiative heat loss coefficient
$K_{conv,1-5}$	Polynomial convective heat loss coefficient
K_{XRD}	X-ray diffraction scale factor
$L(\theta)$	Lorentz-factor
λ	X-ray wavelength
Λ	Bilayer thickness
$(\mu/\rho)_i$	Mass attenuation coefficient of phase i
m	Sample mass

$P(\theta)$	Polarization factor
$\dot{Q}_{appl}$	Applied power
$\dot{Q}_{loss}$	Heat losses
$\dot{Q}_{loss,cond}$	Conductive heat losses
$\dot{Q}_{loss,conv}$	Convective heat losses
$\dot{Q}_{loss,rad}$	Radiative heat losses
$\dot{Q}_{rad}$	Radiant power
$\dot{Q}_{rct}$	Reaction power
r	Radius of the nucleus
R	Electrical resistance
R_0	Electrical resistance at room temperature
R_1	1^{st} order electrical resistance constant
R_2	2^{nd} order electrical resistance constant
R_t	Thermal resistance
σ	Boltzmann constant
t	Time
t_{heat}	Heating time
t_{frame}	Duration frame
t_{cool}	Cooling time
T	Temperature
T^2_{coff}	X-ray temperature coefficient
T_M	Melting temperature
T_{max}	Maximum temperature
T_{RT}	Room temperature
$\dot{T}$	Heating rate
ϑ	Generalized time
θ	X-ray diffraction angle
p	Pressure
V	Voltage
V_R^+	Voltage (+) for the sensor resistance measurement
V_I^+	Voltage (+) for the current measurement

V_R^-	Voltage (-) for the sensor resistance measurement
V_I^-	Voltage (-) for the current measurement
$V_{IR,0}$	Pyrometer output voltage (raw)
V_{IR}	Pyrometer output voltage (corrected)
υ_i	Volume concentration of phase i
χ	Angle between incoming X-ray beam and detector normal
ω	Fraction by weight

Contents

1 Introduction

1.1 Motivation

A look in the past shows that progress in technology is often linked to progress in materials science. The knowledge about the mass production of durable steel enabled the industrial revolution in the 18^{th} century. The availability of high temperature resistant Ni-based alloys for aircraft turbines is the backbone of a globalised world [1]. The digital revolution by information technology would not change our everyday life without silicon semiconductors [2]. These are only a few examples, which demonstrate the importance of materials science for innovation. Surprisingly, it's not the discovery of new elements, which drives this progress. It's the continuous expansion of knowledge about controlling and tailoring the so-called microstructure of materials. According to *Herbert Gleiter* [3], the microstructure is "defined by the type, structure, number, shape and topological arrangement of phases and/or lattice defects which are in most cases not part of the thermodynamic equilibrium structure". This makes the microstructure an essential factor influencing the physical and mechanical properties of materials. Understanding how specific microstructures can be generated means understanding how the properties of a material can be tailored. Therefore it is of fundamental interest to understand, control and generate new types of microstructures to obtain novel materials.

From a general perspective, the microstructure of a material is influenced by four factors: (i) the composition, (ii) the initial microstructure and (iii) the thermal history and (iv) the deformation state [4]. Reactive metallic multilayers

based on Al and Ni form a material system where all factors can be specifically addressed to tailor the microstructure. The layered structure comprising two or more metals gives the opportunity to control the sites and the density of newly formed phases. The characteristic exothermic reaction of this type of material allows access to a broad range of heating rates up to 10^7 $\mathrm{K\,s^{-1}}$ [5]. Therefore, a phenomenon called phase selection - the dependence of the type of phases from the heating rate - can be potentially used for microstructure development. Two different approaches are conceivable to heat the multilayers at high rates: (i) extrinsic heating (rapid heating methods) [6, 7] and (ii) intrinsic heating (runaway reactions) [8–10]. If the fundamental processes of nucleation and diffusion based phase growth are understood under these heating conditions, the formation of nanoscale hard-soft composite materials with well-defined properties may be feasible.

Besides their potential for microstructure design, Al/Ni multilayers are an ideal model material to address fundamental questions about phase formation under highly non-equilibrium conditions. The influence of steep concentration gradients in the layered structure on nucleation behaviour is still under debate [11]. Furthermore, the influence of high heating rates on interdiffusion and phase formation is not sufficiently researched [12].

1.2 State of research

While intensively studied at low heating rates ($\dot{T} < 10\ \mathrm{K\,s^{-1}}$) [13–17], there is only a limited understanding of the mechanism driving the reaction of Al/Ni multilayers at intermediate and high heating rates ($10 < \dot{T} < 10^7\ \mathrm{K\,s^{-1}}$) [7, 12]. Especially from a methodical perspective, the thermal and structural investigation at high heating rates is challenging. The low sample thickness of the reactive thin-films in combination with the highly dynamic reaction impeded a detailed analysis of the mechanism driving the reaction in the past [12]. This section focuses on the currently active research fields with regard to phase transformation in Al/Ni mulitlayers at high heating rates. A more comprehensive insight into the fundamentals of phase transformations in metallic multilayers is given in Chapter 2.

Only in the last decade, advanced experimental approaches emerged, enabling us to explore phase transformations under rapid external and internal heating. One group of experiments uses direct resistance heating approaches. *Fritz et al.* [18] used this method to perform uniform heating experiments on Al/Ni multilayer thin-films. The temperature signal of the reaction enables them to derive four reaction stages: heating to the ignition point, low temperature solid-state mixing, high temperature solid-state mixing, and liquid-state mixing. They explained the rapid self-heating at the high temperature solid-state stage by the formation of intermetallic phases. In a related study [6], they compared different ignition techniques including mechanical ignition, uniform heating and local ignition. The findings pointed to the importance of the heat losses to the surrounding and the material volume heated during ignition. They developed a model for the determination of the ignition temperature. Uniform heating was also applied by *Manukyan et al.* [19] to determine the activation energy of the runaway reaction. Here, the Al/Ni multilayers were heated with rates up to $42.3\ \mathrm{K\,s^{-1}}$. They suggest that the formation of intermetallic nuclei is

the rate-controlling process at temperatures below 500 K, while at higher temperatures the process is reaction-limited. Furthermore, high-resolution transmission electron microscope (HRTEM) investigations of quenched samples revealed that Al_3Ni and Al_3Ni_2 are the first phases.

Chip-based nanocalorimetry is an alternative approach to heat thin-film samples with high heating rates [7, 11, 20]. This method not only allows heating samples indirectly but also enables a simultaneous thermodynamic characterisation of the processes during heating [21]. All studies involving nanocalorimetry chose experimental conditions in such a way that a runaway reaction was not initiated. *Swaminathan et al.* [11] were the first to introduce this method to investigate reactive multilayers. The number of exothermic peaks was reduced from three to two exotherms by increasing the heating rate from $2 \cdot 10^4$ $\mathrm{K\,s^{-1}}$ to $3.3 \cdot 10^4$ $\mathrm{K\,s^{-1}}$. They concluded that steeper concentration gradients of the Al/Ni interface, like they are typically observed at high heating rates, lead to a suppression of intermediate intermetallic phases. The underlying mechanism of interdiffusion is presented in Section 2.4. *Grapes et al.* [7] performed a complete kinetic analysis of the solid-state reaction in a heating rate regime between 10^3 $\mathrm{K\,s^{-1}}$ and 10^5 $\mathrm{K\,s^{-1}}$. For this purpose, nanocalorimetry was combined with dynamic transmission electron microscopy (TEM). They proposed a mechanism where Al_3Ni nucleates at the Al grain boundaries and grows laterally until the grains impinge. Grain boundary diffusion was suggested as the controlling mechanism of the reaction.

To explore phase transformations during rapid intrinsic heating with rates up to 10^7 $\mathrm{K\,s^{-1}}$, researchers have developed *in situ* structural characterizations methods. *Trenkle et al.* [22] and *Fadenberger et al.* [23] investigated self-propagating reaction fronts using synchrotron X-ray diffraction. Although the limited temporal and spatial resolution impeded a clear distinction between individual reaction steps, both studies reported the formation of the NiAl phase in the liquid state of the sample.

To study the role of intermixing in the Al/Ni reaction, two different approaches can be found in the literature. *Mann et al.* [24] used thermal annealing to induce intermixing across the Al/Ni interface. They found a reduction of the velocity of the self-propagating reaction front in the case of annealed Al/Ni multilayers. This was explained by a reduction of the total heat of reaction and a lowering of the diffusion gradient across the interface. *Manukyan et al.* [25] used ion beam irradiation to study the effect of intermixing. They observed that at short irradiation times, an amorphous interlayer was formed, which enhances the reactivity of the sample and lowers the ignition temperature. With longer irradiation time, the reactivity decreased due to the formation Al_3Ni. They concluded that an amorphous layer with small Al_3Ni nuclei speeds up Al-Ni intermixing and phase growth.

Besides experimental approaches, molecular dynamic (MD) simulations were performed to reveal the mechanism driving the Al/Ni reaction. A comparative study using TEM investigation and MD simulation of quenched reaction fronts was performed by *Rogachev et al.* [10]. They could identify a two-stage mechanism. In the first stage, an exothermic dissolution of Ni into liquid Al takes place while NiAl nanograins are formed at the solid-liquid interface. The diffusivity of Ni is significantly enhanced in the liquid gaps between the nucleates. In the second stage, NiAl precipitates start to grow until the reactants are entirely consumed. Using a similar MD simulation approach, *Xu et al.* [26] identified different reaction pathways depending on the reaction temperature. They found that with a reduction of the temperature, there is a shift from Fickian interdiffusion to Ni dissolution as the rate-limiting step. At low temperatures, the formation of the AlNi intermetallic compound dominates the reaction.

This first overview of very recent studies shows that while substantial progress in the advanced experimental methods has been made, the state of research lacks a comprehensive understanding of solid-state and runaway reactions in

reactive multilayers. While partial aspects of the reaction are understood, e.g. the phase transformations that drive a propagating reaction front, experimental limitations still impede a mechanism-based knowledge of phenomena, such as the transformations leading to ignition. Phase formation kinetics and phase selection at elevated heating rates are poorly investigated and still under debate. However, such knowledge is crucial and would pave the way for the development of novel microstructure design tools which harness the unique transformations conditions under rapid heating.

1.3 Objective of the work

The objective of this study is the development of a mechanism-based understanding of the structural transitions in nanoscale metallic multilayers. The influence of high heating rates (10 - 10^6 $\mathrm{K\,s^{-1}}$) on the phase formation behaviour is the focus of the research. For this purpose, the reactive Al/Ni multilayer system is used as model material. Based on this, several sub-objectives are derived:

1. Development of a methodical approach for the thermodynamic and structural characterisation of Al/Ni multilayers under various heating rate conditions. A time resolution of less than 1 ms is targeted to resolve the highly dynamic processes driving the runaway reactions ($\dot{T} \approx 10^6$ $\mathrm{K\,s^{-1}}$).

2. It is expected that solid-state reactions allow a controlled transition of Al and Ni into the corresponding product phase. The objective is to set up a quantitative description of the phase formation kinetics as a basis for the adjustment of defined product phase fractions in the multilayer stack.

3. When the ignition point of a reactive material is reached, the reaction turns from a solid-state to a runaway reaction. Thermodynamic characterisation should be used to quantify the ignition point. Besides the impact of the multilayer architecture, special focus will be set on the manipulation of the ignition temperature by external factors, like heat treatment and heat capacity. This may enable us to exploit new kinetic regimes for phase formation.

4. *In situ* investigation of the runaway reaction in Al/Ni multilayers will be conducted. The objective is to evaluate the influence of the solid/liquid state of the sample on the phase formation behaviour. In this context, the relevance of phase formation on the initiation of a runaway reaction is elucidated. Besides this, the role of interdiffusion and metastable phase formation at elevated heating rates should be assessed. Eventually, these findings enable us to set up a mechanism for phase formation under high heating rate conditions.

2 Basics

Reactive metallic multilayers belong to the class of energetic materials. Once ignited by an external source, they release their chemically stored energy within milliseconds. This chapter gives a general introduction to reactive metallic multilayer materials with a particular emphasis on thermodynamic and kinetic aspects of the runaway reaction. The specific material properties, reaction characteristics and potential applications of this material class are summarized in Section 2.1. The study focuses on metallic multilayers comprised of Al and Ni. The corresponding phase diagram and potential product phases are discussed in Section 2.2. In Section 2.3, the concept of ignition and runaway reactions is described. Finally, thermodynamic aspects of nucleation in heterogeneous systems are discussed in Section 2.4.1. The corresponding kinetic aspects, including diffusion, phase growth kinetics and phase selection in metallic multilayers are considered in Section 2.4.2 – 2.4.5.

2.1 Reactive multilayers

Reactive multilayers are thin-films that are able to release a significant amount of stored thermal energy when externally stimulated. In the course of the reaction, the material heats up to peak temperatures of $\sim$1200 °C with heating rates up to $\sim 10^6$ $\mathrm{K\,s^{-1}}$. An essential aspect of reactive multilayers is the high density of interfaces, which is achieved by stacking nanoscale layers of at least two reactants. The driving force behind the exothermic reaction is the

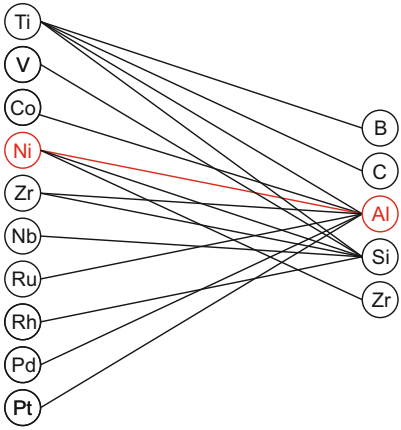

Figure 2.1: Overview of the known binary material combinations which exhibit highly exothermic reactions as they are characteristic of reactive materials [5].

transition of a metastable solid into a low energy product phase. Typically, processes like interdiffusion, compound formation and grain growth in the solid and the liquid state drive the reaction [15]. To date, more than 50 different types of reactive multilayers have been described in the literature [5]. Most of them form aluminide, boride, carbide, silicide, titanide, zirconide or thermite product phases during the reaction. An overview of different types of reactive multilayers is given in Figure 2.1.

Generally, the reactivity of metallic multilayers is determined by the ability of atomic transport across the interface. The atomic exchange is driven by the difference in the chemical potential between the reactant and product phase. To what extent the interface acts as a barrier for the diffusion flux depends on various factors, including the atomic structure at the interface, contamination and the reaction progression [27]. Moreover, the thin-film deposition technique

plays a crucial role in defining the interfacial properties [28]. Besides the interfacial properties, the reactivity of a metallic multilayer system is determined by the bilayer thickness Λ [27]. The overall composition of the multilayer stack is set by adjusting the individual layer thickness of the reactants. Experimental studies show that the formation reaction is completed more rapidly when the thickness is lowered [9]. The reason for this is the reduction of the diffusion distances perpendicular to the interfaces which enhances intermixing between the reactants.

Typically, metallic multilayer materials are fabricated by thin-film deposition techniques like physical vapour deposition (PVD) and chemical vapour deposition (CVD). The majority of the studies in the literature use magnetron sputtering [9, 14, 24, 29] or electron-beam deposition [13, 16, 28, 30]. Both techniques enable the deposition of thin-films with well-defined periodical structures. Interestingly, the fabrication affects the phase formation during heating. For instance, in the case of electron-beam deposition, the suppression of the metastable Al_9Ni_2 phase was observed [28]. This points to the relevance of the microstructural and interfacial properties on the nucleation behaviour of the product phase [28].

The exothermic reaction in reactive multilayers is driven by structural changes, such as interdiffusion and phase formation. Depending on the reaction temperature and the melting point of the elements, these processes take place either in the solid state or the liquid state of the sample. However, in most cases, the reaction is initiated in the solid state of the sample. Figure 2.2 illustrates the major mechanisms, which are driving the reaction in metallic multilayers. Although there is a significant driving force for phase formation, no spontaneous nucleation is observed [31]. This points to the relevance of nucleation barriers. The effect of steep concentration gradients at the interface are discussed in detail in Section 2.4.1. When the sample is completely reacted, either a single-

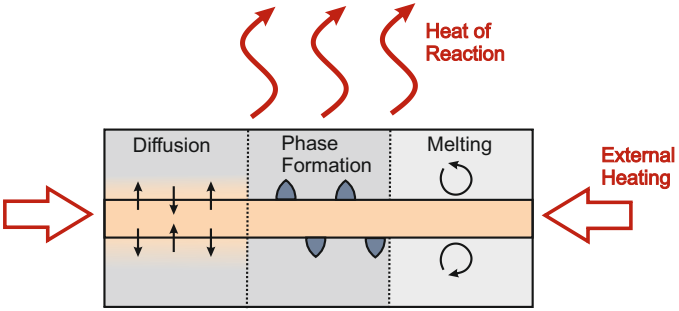

Figure 2.2: Overview of the physical processes which dominate the metallic multilayers reaction. When externally heated, diffusion across the interface is initiated. After a sufficient amount of intermixing, intermetallic phases are able to form. Melting of the reactants may further accelerate the processes of diffusion and phase formation.

or multi-product phase can be formed. The latter is usually caused by an incomplete reaction or the thermodynamic stability of multiple phases [32, 33].

For the ignition of reactive multilayers, a threshold defined by a critical energy or power density has to be overcome. The reaction propagates only without external energy input (= self-sustaining reaction) when the heat release is sufficient to enable further reaction progression [13]. A critical heating rate must be exceeded to ignite a reactive material. The critical rate depends on numerous parameters, like sample geometry, thin-film design and composition [6]. If the heat release falls below a critical limit, the reaction stops and the sample cools down. The temperature profile of a reaction is defined by the kinetics of mass diffusion, chemical reactions, thermal transport and energy-loss mechanisms [5]. Below the ignition threshold, the reaction can only proceed by external heating of the reactive multilayer stack [12].

In recent years, multiple applications for reactive multilayers were introduced. From an economic point of view, the most successful application is joining. For this purpose, Al/Ni(V) multilayer thin-films (NanoFoil ®) are used [34]. Reactive materials are especially advantageous for the joining of dissimilar materials such as metallised ceramics or bulk metallic glasses. The reactive material is used as a heat source in order to melt a tin-based solder layer and form a high strength bond. With this method, the heat-affected zone is significantly reduced compared to traditional methods like welding [35]. Besides joining, there are several applications in the early development stage. For instance, the exothermic reaction power is used for microscale power sources [36], the ignition of propellants [37] or to defeat harmful microorganisms [38]. A relatively new approach is the usage of reactive multilayers as self-healing materials [39]. However, not only the release of exothermic heat can be used but also the product phase which is formed during the reaction. This method is called combustion synthesis or reaction synthesis. This approach is used to synthesise high-melting-point materials, like intermetallic phases or ceramic materials. [40–45]

2.2 The Al/Ni system

The binary Al-Ni system is a well-studied system. Figure 2.3 shows the corresponding equilibrium phase diagram of Al-Ni assessed by *Nash et al.* [46]. Besides Ni and Al, the system is characterized by the presence of five stable intermetallic compounds, namely Al_3Ni, Al_3Ni_2, AlNi, Al_3Ni_5 and $AlNi_3$. The most important physical properties of these intermetallic compounds are summarized in Table 2.1.

Among these phases, AlNi exhibits the highest melting temperature of 1638 °C and the highest homogeneity range between 42 at.% Ni and 69.2 at.% Ni. With

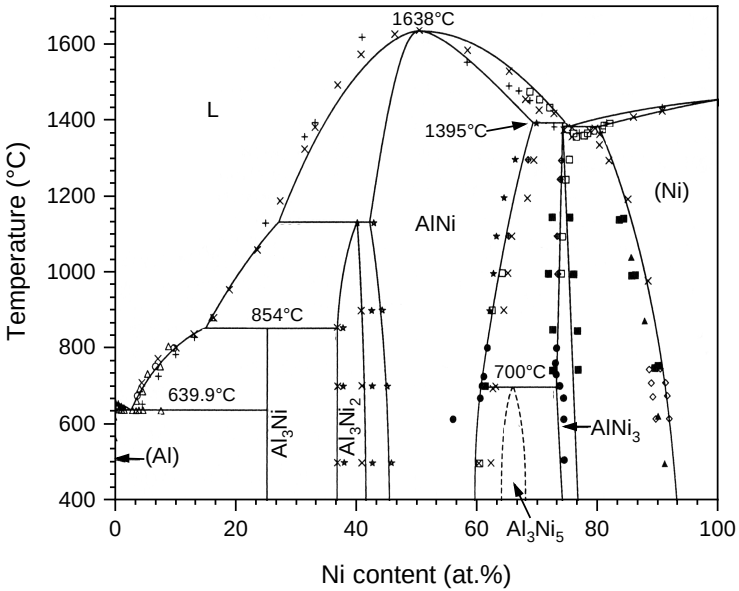

Figure 2.3: Equilibrium phase diagram of the Al-Ni system. Five different thermodynamic stable intermetallic phases, namely Al_3Ni, Al_3Ni_2, AlNi, Al_3Ni_5 and $AlNi_3$, are reported. The highest melting temperature of 1638 °C exhibits the AlNi phase. [46]

660.4 °C in the case of Al and 1455 °C in the case of Ni, the AlNi compound exceeds the melting temperature of the pure elements. The lowest melting temperature (T_m = 639.9 °C) can be found for the eutectic reaction $L \leftrightarrow Al_3Ni + (Al)$ at a composition of 2.7 at.% Ni. At 36.8 at.% Ni and 854 °C the phase diagram exhibits the first peritectic reaction $L + Al_3Ni2 \leftrightarrow Al_3Ni$. The second peritectic reaction $L + AlNi \leftrightarrow Al_3Ni_2$ takes place at 1133 °C and a content of 40 at.% Ni. A further peritectic and eutectic reaction involving Al_3Ni_5 and $AlNi_3$ can be found at the Ni-rich side of the phase diagram. All phases differ significantly in their solubility for Ni and Al. While for the Al_3Ni compound only negligible amounts of Ni and Al can be dissolved, the stoichiometry range of Al_3Ni_2 ranges from 36.8 at.% Ni up to 41.5 at.% Ni. Pure

Al has a very limited Ni solubility of 0.11 at.% at the eutectic temperature, which decreases to 0.01 at.% at 500 °C. In contrast, the solubility of Al in Ni is 7 at.% at 500 °C and extends up to 21.2 at.% at 1385 °C. Besides the equilibrium intermetallic compounds, the formation of the metastable compound Al_9Ni_2 is reported [8, 14, 47–50]. This phase was mainly observed during the heating of Al/Ni multilayers, which were deposited by magnetron sputtering. To the knowledge of the author, no data about the limits of solubility are published for this compound.

The crystal structure of the pure elements Al and Ni is cubic face centred (fcc). The *B*2 phase AlNi crystallizes in a cubic primitive unit cell and the Al_3Ni_2 in a hexagonal primitive unit cell with 5 atoms. The most complex structure with an orthorhombic primitive unit cell and 16 atoms is present in Al_3Ni. Comparing the enthalpy of formation ΔH_f of the individual compounds at an Al:Ni composition of 1:1, the highest absolute value of ΔH_f with -59 kJ (mol at)$^{-1}$ can be found for AlNi. As shown in Figure 2.4, Ni-rich or Al-rich compounds exhibit lower absolute values of ΔH_f. In the case of Al_3Ni_2 the enthalpy of formation is

Table 2.1: Physical properties of Al-Ni intermetallic compounds

	Al_3Ni	**Al_3Ni_2**	**AlNi**	**Al_3Ni_5**	**$AlNi_3$**
Composition (at%)	25	36.8-41.5	42-69.2	64-68	73-76
Form. enthalpy (kJ/mol at)	-38	-57	-59	-51	-41
Max. temperature (°C)	854	1133	1638	700	1385
Space group	Pnma	P-3m1	Pm-3m	Cmmm	Pm-3m
Strukturbericht	$D0_{11}$	$D5_{13}$	*B*2	-	$L1_2$
Prototype	Fe_3C	Al_3Ni_2	CsCl	Ga_3Pt_5	$AuCu_3$

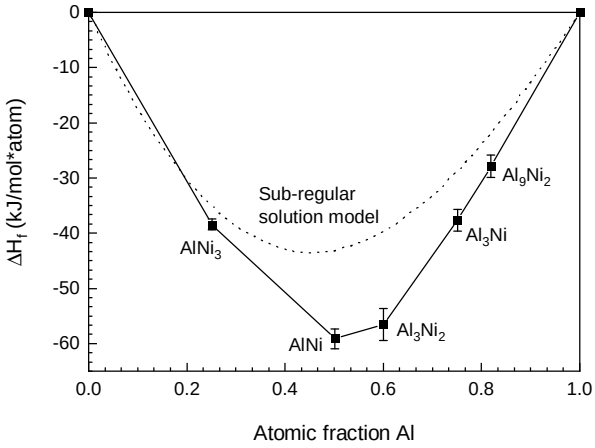

Figure 2.4: Enthalpy of formation versus the composition determined by *Blobaum et al.* [50]. The dashed line indicates the enthalpy for a sub-regular solid solution.

-57 kJ (mol at)$^{-1}$, whereas in the case of Al_3Ni ΔH_f is -38 kJ (mol at)$^{-1}$. Therefore, significantly less exothermic heat is released during compound formation. Based on ΔH_f, the adiabatic reaction temperature of the system can be determined. This quantity is the characteristic temperature when ΔH_f of the product phase is completely transferred into heating of the system in the absence of heat losses to the surrounding. For the composition of the most exothermic AlNi product phase in the Al-Ni system, an adiabatic reaction temperature of 1639 °C was determined [51].

2.3 Ignition and runaway reaction

Ignition is defined as the point where a reaction becomes self-sustaining. To ignite a reactive material, specific thermodynamic conditions have to be fulfilled. Besides theoretical aspects, these conditions are described in this section. Generally, a distinction is made between the two ignition modes: (i) Point ignition

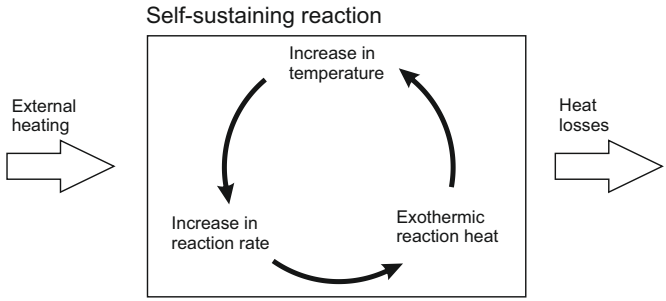

Figure 2.5: Illustration of the thermal ignition process. At a critical temperature, exothermic reactions are initiated. Depending on the amount of heat losses, the temperature of the system raises, causing a further increase in the reaction rate. This is called self-sustaining reaction, which is the basis for thermal ignition.

and (ii) ignition by uniform heating. In the first case, a self-sustaining reaction is triggered by a local discharge of energy [52]. Experimental studies showed that this can either be a mechanical impact, laser irradiation or electrostatic discharge [5, 6]. Point ignition causes a reaction wave propagating through the multilayer sample (= self-propagating reaction). In the case of uniform heating, the whole sample volume is rapidly heated. Several methodical approaches are reported for uniform heating, such as hot plate experiments [18, 53], electrical resistance heating [18], electrothermography [19] and nanocalorimetry [54]. Since the focus of this study is on uniform heating, point ignition is not elaborated in detail.

In most cases, reactives are ignited by external thermal energy. This type of ignition is called thermal (spontaneous) ignition or thermal explosion. The principle of thermal ignition is illustrated in Figure 2.5. Thermal ignition is a self-enforcing process that is initiated by external heating. Once a critical

temperature is reached, the reaction process starts. In the case of metallic multilayers, these reactions are predominantly intermixing and phase formation. Due to the exothermic nature of these processes, heat is released. If the exothermic heat release exceeds the heat losses to the surrounding, the temperature of the system increases. In turn, the temperature rise increases the rate of the exothermic reactions and leads to further heating until finally a runaway reaction or explosion occurs. [52]

Between the point of ignition and the point where a macroscopic temperature increase occurs, a certain amount of time, called the ignition delay, is observed. To understand the ignition delay, it is helpful to consider the adiabatic case of ignition. In this case, heat losses are neglected and, following ignition, there is no temperature increase by further external heating. In the very early stages of the reaction, only a few reaction events occur, resulting in an incremental temperature increase. There is a mutual dependency between the self-heating rate and the number of reaction events. The increase of one quantity leads to the increase of the remaining one. In case of a low self-heating rate, the time which is required to move into the explosive regime (= ignition delay) is long. However, when there is a steep increase in the number of reaction events, the ignition delay can be reduced to milliseconds. One of the most important parameters defining the ignition delay is the heat capacity of the sample. To self-heat a sample with a high heat capacity, a higher amount of reaction power is required for an incremental temperature increase and the ignition delay is increased. [52]

From a theoretical point of view, ignition was first described by *Semenov* [55] in 1935. Although the work of *Semenov* refers to combustible gaseous mixtures, the fundamental aspects are also valid for reactive multilayers. The theory is based on the concept of relating the heat of reaction $\dot{Q}_{rct}$ to the heat

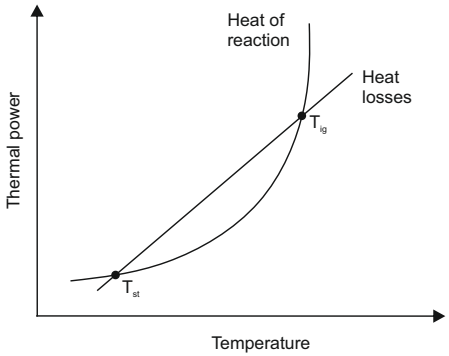

Figure 2.6: Following the theory of *Semenov* [55], thermal ignition occurs when the heat of reaction $\dot{Q}_{rct}$ exceeds the heat losses $\dot{Q}_{loss}$. For $T_{st} < T < T_{ig}$, $\dot{Q}_{loss}$ is dominant. Without external heating, the system cools down to T_{st}. For $T > T_{ig}$, $\dot{Q}_{rct}$ exceeds $\dot{Q}_{loss}$ and the system is self-heating and thermal ignition occurs.

losses $\dot{Q}_{loss}$ in a given system. If the heat of reaction exceeds the losses, the excess thermal energy heats up the sample, which results in a thermal explosion. Based on this, the condition for ignition is defined as

$$\dot{Q}_{rct} > \dot{Q}_{loss} \tag{2.1}$$

This principle is exemplarily illustrated in Figure 2.6. As the temperature rises, both $\dot{Q}_{rct}$ and $\dot{Q}_{loss}$ increase. Above the stationary temperature T_{st}, the system is stable since $\dot{Q}_{rct}$ does not exceed $\dot{Q}_{loss}$. Without external heating, the system cools down to T_{st}. However, if the temperature exceeds the ignition temperature T_{ig}, the ratio between $\dot{Q}_{loss}$ and $\dot{Q}_{rct}$ flips and inequality 2.1 is fulfilled. The sample exhibits self-heating and ignition occurs.

To adapt the theoretical approach of *Semenov* to reactive multilayers, *Fritz et al.* [6] introduced physical descriptions for $\dot{Q}_{rct}$ and $\dot{Q}_{loss}$ for planar multilayers. In the case of $\dot{Q}_{loss}$ only conductive and convective heat losses are assumed:

$$\dot{Q}_{loss} = \frac{1}{d_{sample} R_t} \Delta T^m \tag{2.2}$$

Here, d_{sample} is the multilayer sample thickness, $1/R_t$ is the inverse thermal resistance, ΔT the temperature difference between sample and surrounding. The coefficient m takes the proportion of convective and conductive heat losses into account and ranges from 1.00 to 1.25. For the calculation of the reaction power, a linear dependency of $\dot{Q}_{rct}$ with the growth rate of the product phase dx_{prod}/dt is assumed. This is given by

$$\dot{Q}_{rct} = \frac{dx_{prod}}{dt} \frac{\Delta H_{rx}}{\Lambda/2} \tag{2.3}$$

where ΔH_{rx} is the total heat of formation and Λ is the thickness of a single bilayer. For a complete description of $\dot{Q}_{rct}$, the temperature-dependent growth rate of the product phase is required. For this purpose, *Fritz et al.* used the model developed by *Highmore and Greer* [56] to describe the phase growth in multilayers based on diffusion. Applied to equation 2.3, the $\dot{Q}_{rct}$ is given by

$$\dot{Q}_{rct} = \frac{2 D_0 \Delta H_{rx}}{\Lambda x_{prod}} \left(\frac{c_{range}}{c(1-c)} \right) \exp\left(\frac{E_A}{R T_{ig}} \right) \tag{2.4}$$

Here, c is the composition of one reactant, c_{range} the fractional concentration over which the product phase exists, E_A the activation energy, R the gas constant. By replacing $\dot{Q}_{rct}$ and $\dot{Q}_{loss}$ in equation 2.1, the ignition temperature can be calculated by

$$T_{ig} \propto \frac{E_A/R}{ln\left[\frac{2d_{sample}\Delta H_{rx}D_0R_T}{\Lambda x_{prod}}\left(\frac{c_{range}}{c(1-c)}\right)\right]} \tag{2.5}$$

Although some aspects such as a multi-step type of reaction, product phase and thickness dependent diffusion constants are not included in the model of *Fritz et al.*, the basic dependencies of the ignition temperature are well described. The model predicts a decrease of the ignition temperature with decreasing bilayer thickness which is in good agreement with experimental results [57]. The ignition sensitivity is also affected by diffusion. High values of E_A inhibit the reaction and therefore increase the ignition temperature. Therefore the model gives valuable insights into the fundamental links between material properties and ignition temperature.

2.4 Solid-state phase formation in metallic multilayers

The Gibbs free energy ΔG is a thermodynamic quantity, which allows measuring the favorability of a reaction at constant temperature and pressure. If $\Delta G = 0$, the system is in equilibrium and there is no thermodynamic driving force for phase transitions. By changing parameters like the composition, temperature or pressure, the system is pushed away from the equilibrium condition. Reactive metallic multilayers provide an extreme example where a thermodynamically highly unstable system is created by manufacturing. Here, ΔG is negative and there is a high driving force to rebalance the system. If not kinetically suppressed, this could be attained by phase transitions upon heating. In the case of Al/Ni multilayers, intermetallic compounds are formed. Generally, phase formation is described by nucleation and subsequent growth. Hence, this

section gives a short introduction to classical nucleation theory adapted to the particular case of metallic multilayers, where steep concentration gradients act as a thermodynamic barrier for nucleation.

2.4.1 Nucleation in a composition gradient

Phase transitions often start with a nucleation event, which is driven by the reduction of ΔG. The formation of a small region of a thermodynamically more stable phase results in a change of the free energy by crystallisation ΔG_V. The driving force for this transition is the change of the chemical potential. This process creates an interface between the newly formed phase and the parent phase, which requires the surface free energy ΔG_γ. In the case of heterogeneous nucleation, ΔG_γ is reduced by nucleation on a preexisting interface or surface. Here, for simplification, only the homogeneous case is considered. Besides the surface energy, in the solid-state the strain energy ΔG_s caused by volume changes between parent and product phase have to be taken into account. By aggregating the individual contributions, the free energy change of homogeneous nucleation is given as [58]

$$\Delta G_{hom} = (\Delta G_V + \Delta G_s) + \Delta G_\gamma \tag{2.6}$$

$$= \frac{4\pi r^3}{3v_l}(\Delta g^{\alpha\beta} + \Delta p g_s) + 4\pi r^2 \gamma \tag{2.7}$$

where r is the radius of the nucleus, v_l the volume of an atom, γ the specific surface energy and Δg the individual free energy contribution per atom. For small r, the endothermic surface energy overcompensates the chemical free energy. As a result, the nucleus is not stable and dissolves again. For nucleation, the agglomeration of atoms has to exceed r^* to form a stable nucleus. The simplified case without strain is plotted with a solid line denoted by $\nabla c = 0$ in Figure 2.8.

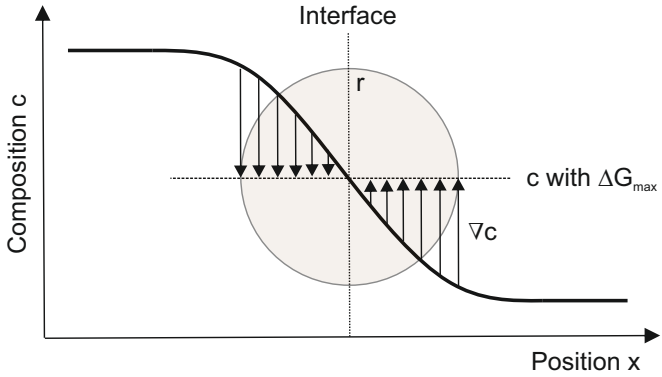

Figure 2.7: Nucleation in a symmetrical concentration gradient. With increasing size, the nucleus overlaps with regions with deviating composition. This results in a lowering of the driving force for nucleation.

In the classical nucleation theory, kinetic considerations are not taken into account. The composition of the initial phase is equivalent to the product phase. The situation is different when nucleation takes place in a region with a nonuniform composition, like it is the case at the interfaces of multilayer materials. Nucleation in a symmetric concentration profile is illustrated in Figure 2.7. Typically, concentration gradients lower the energy release by nucleation. The reason for this is the deviation of the matrix composition from the composition of the nucleus. The driving force for nucleation is maximized when the original matrix exhibits the same composition as the equilibrium composition of the product phase. In Figure 2.7, this optimum composition is marked with a dashed line. Depending on the size of the nucleus, there are regions where the composition deviates from the optimum. Since the free energy is lowered with increasing deviation from the optimum composition, nucleation is less favourable in these regions from a thermodynamic point of view. This is especially

true if the size of the nucleus is in the same order as the extension of the concentration gradient (x-axis in Figure 2.7) [59]. *Gusak et al.* [60] and *Desré et al.* [32] proposed a model which describes the lowering of the free energy of formation by

$$\Delta G_{grad} = \Delta G_{hom} + \zeta (\nabla c)^2 r^5 \tag{2.8}$$

Here, ΔG_{hom} is the Gibbs free energy change by homogeneous nucleation, ζ a (positive) constant, ∇c the concentration gradient and r the radius of the nucleus. Equation 2.8 covers two particular nucleation modes: (i) polymorphic nucleation, which is characterised by a structural change without a compositional change [60] and (ii) the transversal nucleation mode, where the atomic transport is perpendicular to the concentration gradient (parallel to the x-axis in Figure 2.7) [32, 33]. Both nucleation modes differ in the possibility of atomic transport. While there is enough time for chemical redistribution in the case of transversal nucleation, no diffusion occurs in the case of polymorphic nucleation. Complementarily, it should be noted that there is a third longitudinal nucleation mode, which is described in detail in the work of *Hodaj et al.* [61]. The effect of a concentration gradient on the free formation energy is shown in Figure 2.8. In case of homogeneous nucleation ($\nabla c = 0$, $\Delta G_s = 0$), the nucleus is stable beyond r^*. With increasing ∇c the nucleus becomes metastable. With increasing r, the growth of the nucleus becomes more and more thermodynamically unfavourable because additional energy is required. With further increase of ∇c, ΔG rises continuously and nucleation is completely suppressed.

In conclusion, reactive metallic multilayers exhibit a high driving force for the nucleation of intermetallic phases. However, steep composition gradients, like they occur at interfaces, may suppress nucleation. Therefore, flattening of the composition gradient is required prior to nucleation. Interdiffusion must precede nucleation to form thermodynamic stable nuclei [62].

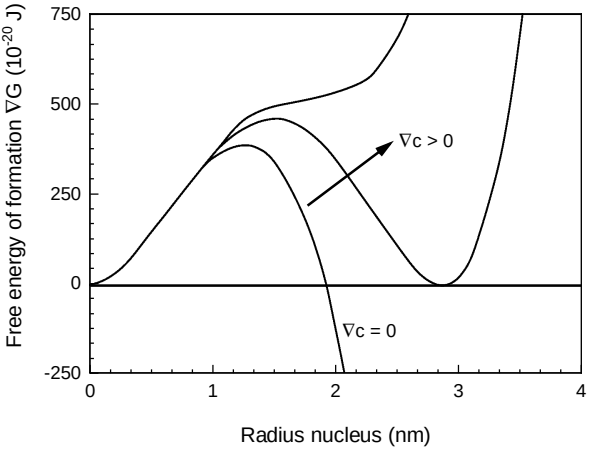

Figure 2.8: Dependency of the free energy of formation ΔG of the composition gradient ∇c. In the case of a constant composition, the nucleus is thermodynamically stable when the critical size r^* is exceeded. With increasing ∇c a metastable state is reached where growth is unfavourable. Finally, the formation of a nucleus is completely suppressed in the case of high ∇c. [33]

2.4.2 Diffusion in metallic multilayers

As already stated in the previous section, phase formation is only possible when diffusion precedes. This was also theorized by *Thompson* [62]. Diffusion is not only crucial for phase nucleations in metallic multilayers but also for the location of phase formation and the growth rate. In consequence, the morphology of the newly formed phase is predominantly determined by diffusion fluxes in the microstructure. In crystalline solids, atomic transport can take place in structurally different ways. While lattice diffusion is the dominating transport mechanism in single-crystal materials, in nanoscale multilayers the lattice defects are the major sites for diffusion. The high density of grain boundaries, dislocations and free surfaces in thin-films act as high-diffusivity pathways in the microstructure (often called diffusion short circuits). The distortion of the lattice facilitates atomic transport. For example, the lower local density of a

high-angle grain boundary enhances the diffusion of atoms [63, 64]. In general, diffusion can be described by the Arrhenius equation

$$D = D^0 \exp\left(\frac{E_a}{RT}\right) \tag{2.9}$$

Here, D^0 is the pre-exponential factor, E_a the activation energy, r the ideal gas constant and T the temperature. Depending on the type of defect, the value of the diffusivity D varies [65]:

$$D_S \geq D_{GB} \geq D_D \gg D_L \tag{2.10}$$

Surface diffusion D_S exhibits the highest diffusivity, followed by grain boundary diffusion D_{GB} and dislocation diffusion D_D. The lowest diffusivity is generally found for lattice diffusion D_L. This is mainly caused by differences in activation energy. The pre-exponential factor is constant in a first approximation [64]. According to the exponential temperature dependency in equation 2.9, the differences between the individual diffusion mechanisms are more pronounced at low temperatures.

At the melting temperature of the material, the value of grain boundary diffusivity is approximately 4 orders of magnitude higher compared to lattice diffusion. This phenomenon explains why nucleation in metallic multilayers starts at grain boundary triple junctions. Referring to equation 2.8, the critical composition gradient for nucleation is first reached at triple junctions. The corresponding high-diffusivity pathways are illustrated in Figure 2.9. Diffusion is dominant at the original α-β interface as well as the α_1-α_2 grain boundary. When the nucleus is formed, the newly created α-γ interface is an additional fast diffusion path [66]. As a consequence, nucleation kinetics strongly depends on the microstructure of the material. The average grain size defined

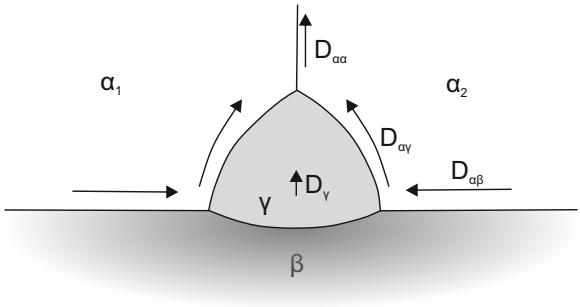

Figure 2.9: Grain boundary triple junctions are preferred sites for nucleation in metallic multilayers. The main reason for this are high-diffusivity pathways along the α-β and the α-γ interface. Lattice diffusion through the γ phase is negligible. [66]

by manufacturing, layer thickness and temperature treatment (e.g. recrystallization through annealing), defines the nucleation site density in metallic multilayers [8, 15].

In metallic multilayers, diffusion across the interface is not necessarily symmetric. In the case of Al/Ni multilayers, Ni acts as a fast diffusor, which leads to an asymmetric diffusion flux [67]. Since there is only a very limited amount of solubility of Ni in Al in equilibrium condition (see Figure 2.3), the reason for the fast diffusion of Ni is still an open question. Possible explanatory approaches are the isostructural crystal lattice, favouring supersaturation of Ni [14] or excess vacancies formed during sputter deposition [30].

2.4.3 Phase growth kinetics

In metallic multilayers, it is generally observed that the type of the first product phase is independent of the overall composition [68]. This is an indication that the phase sequence is determined by processes at the interface. *Goesele and Tu* [69] were the first to propose a model which describes the competitive nucleation and growth of phases by diffusion fluxes at the interface. For this purpose, two reactants α and β separated by a planar compound layer γ are assumed. The schematic of the model is shown in Figure 2.10. The reactant phases α and β are solid solutions. By initial interdiffusion the equilibrium concentration of the α interface $c^{eq}_{\alpha\gamma}$ and of the β interface $c^{eq}_{\beta\gamma}$ were reached. Correspondingly, the equilibrium composition of the γ interface is given by $c^{eq}_{\gamma\alpha}$ and $c^{eq}_{\gamma\beta}$. The resulting composition gradient in γ is illustrated with a dashed line. The equilibrium composition at the interfaces was derived using the tangents rule of the Gibbs free energy. This procedure will not be discussed in detail here. For more detailed information, it should be refereed to *Nucleation in Condensed Matter: Applications in Materials and Biology* [59].

Two different cases are considered. In the first case, no interdiffusion fluxes (= constant composition) inside the α and β phases are assumed. In the second case, the impact of interdiffusion (= non-uniform composition) is considered. Two assumptions are made for simplification in both cases: (i) volume changes due to phase transitions are neglected and (ii) the coefficient of diffusion D is assumed to be concentration-independent. In the first case, the difference between $c^{eq}_{\gamma\alpha}$ and $c^{eq}_{\gamma\beta}$ generates an interdiffusion flux through the γ phase in order to balance the difference in compositions. The presence of three phases is thermodynamically not a stable condition.

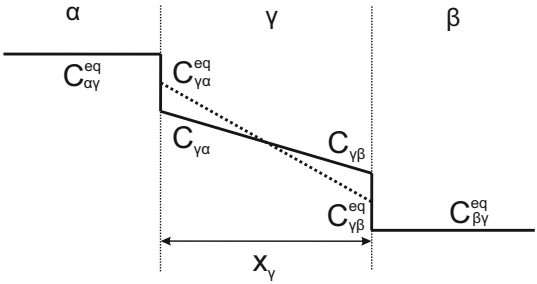

Figure 2.10: Composition profile of two solid solutions α and β with a γ product phase at the interface. $c^{eq}_{\alpha\gamma}$ and $c^{eq}_{\gamma\alpha}$ denote the equilibrium composition at the α-γ and the β-γ interface. Interfacial dissolution processes lead to deviations of the equilibrium composition, denoted with $c_{\gamma\alpha}$. The composition gradient in γ is the driving force for interdiffusion fluxes, which thickens the γ product layer. [69]

According to Fick's law, the diffusion flux in γ can be described with

$$j_\gamma = -D_\gamma \left(\frac{dc}{dx}\right)_\gamma \tag{2.11}$$

where D_γ is the interdiffusion coefficient of the γ phase and $(dc/dx)_\gamma$ the composition gradient. In order to supply the diffusion flux though γ, the α and β phase must be dissolved. The dissolution process takes place by atomic rearrangement at the interface. Due to this, the compositions at the interface $c_{\gamma\alpha}$ and $c_{\gamma\beta}$ deviate from the equilibrium values. The solid line in Figure 2.10 illustrates this difference in composition. The diffusion flux generated by dissolution is given by

$$j_\gamma = \kappa_{\gamma\alpha}(c^{eq}_{\gamma\alpha} - c_{\gamma\alpha}) = \kappa_{\gamma\beta}(c^{eq}_{\gamma\beta} - c_{\gamma\beta}) \tag{2.12}$$

where $\kappa_{\gamma\alpha}$ and $\kappa_{\gamma\beta}$ are dissolution rate constants at the γ-α and γ-β interface and $c_{\gamma\alpha}$, $c_{\gamma\beta}$ are the interfacial concentrations in the γ phase. Based on equation 2.11 and 2.12 the velocity of the α-γ and γ-β interfaces is given as

$$\frac{dx_{\alpha\gamma}}{dt} = \frac{-j_\gamma}{c^{eq}_{\alpha\gamma} - c_{\gamma\alpha}} \quad \text{and} \quad \frac{dx_{\gamma\beta}}{dt} = \frac{-j_\gamma}{c_{\gamma\beta} - c^{eq}_{\beta\gamma}} \tag{2.13}$$

where $dx_{\alpha\gamma}/dt$ and $dx_{\gamma\beta}/dt$ are the interface velocities. Now, on the basis of the interface velocities the thickening rate of the γ phase can be defined by

$$\frac{dx_\gamma}{dt} = \frac{dx_{\gamma\beta}}{dt} - \frac{dx_{\alpha\gamma}}{dt} \tag{2.14}$$

$$= j_\gamma \left(\frac{1}{c^{eq}_{\alpha\gamma} - c_{\gamma\alpha}} - \frac{1}{c_{\gamma\beta} - c^{eq}_{\beta\gamma}} \right) = H_\gamma j_\gamma \tag{2.15}$$

Using the equation for diffusion 2.9 and for dissolution 2.12 the basic description of γ phase thickening rate can be written as

$$\frac{dx_\gamma}{dt} = \frac{H_\gamma \kappa_\gamma (c^{eq}_{\gamma\alpha} - c^{eq}_{\gamma\beta})}{1 + (x_\gamma \kappa_\gamma / D_\gamma)} \tag{2.16}$$

$$\text{with} \quad \frac{1}{\kappa_\gamma} = \frac{1}{\kappa_{\gamma\alpha}} + \frac{1}{\kappa_{\gamma\beta}} \tag{2.17}$$

where x_y is the product phase layer thickness and κ_γ is the effective rate based on the dissolution constants at the α-γ and γ-β interface. A critical thickness x^*_γ can be derived where the growth kinetics change. This is given by $x^*_\gamma = (D_\gamma/\kappa_\gamma)$. For a better understanding of equation 2.16, two limiting cases are considered: (i) a thin product layer $x^*_\gamma \ll x_\gamma$ at the initial stage of the reaction and (ii) a thick product layer $x^*_\gamma \gg x_\gamma$ at later stages of the reaction. [69]

In the case of a thin product layer, growth is limited by the reaction at the interface so that $x_\gamma \ll (D_\gamma/\kappa_\gamma)$. Thus, the thickening rate of γ is given by

$$\frac{dx_\gamma}{dt} = H^\gamma \kappa_\gamma (c^{eq}_{\gamma\alpha} - c^{eq}_{\gamma\beta}) \Rightarrow x_\gamma \propto t \tag{2.18}$$

Thus, the thickening rate of γ is proportional to κ_γ, the reaction rate at the interface. The difference between $c_{\gamma\alpha}$ and $c_{\gamma\beta}$ from their equilibrium values is substantial. The temporal integration shows that the thickness of γ is directly proportional to the reaction time. If κ_γ remains constant, the rate of phase formation is constant. In addition, equation 2.18 gives some evidence on which types of phases are favoured to form first. These are phases which exhibit a high interfacial reaction rate κ_γ and a broad composition range, which is equivalent to a high value of $(c^{eq}_{\gamma\alpha} - c^{eq}_{\gamma\beta})$. These conditions are especially true for amorphous phases or solid-solutions, which are often observed in experimental investigations [28].

This is different in the case of a thick product phase layer. Here, $x_\gamma \gg (D_\gamma/\kappa_\gamma)$ can be assumed. Based on equation 2.16, the thickening rate of γ is given by

$$\frac{dx_\gamma}{dt} = \frac{H_\gamma (c^{eq}_{\gamma\alpha} - c^{eq}_{\gamma\beta}) D_\gamma}{x_\gamma} \Rightarrow x_\gamma \propto t^{1/2} \tag{2.19}$$

The thickening rate of γ is proportional to D_γ and inversely proportional to the product layer thickness x_y. With increasing thickness of γ, the growth rate slows down. Therefore, the thickness of γ is proportional to $t^{1/2}$, which is typically observed for diffusion-controlled processes.

One major conclusion of the theoretical approach of *Goesele and Tu* [69] is the formation of the product phase in two separated stages. *Coffey et al.* [70] were the first to experimentally validate this phenomenon in Al/Nb and amorphous-Si/Ni multilayers. For Al/Ni multilayers, *Ma et al.* [27] found a mechanism

based on the two-stage formation of the Al_3Ni phase. In both studies, two distinctive exotherms were observed using differential scanning calorimetry (DSC), which could be assigned to the formation of only one phase. Figure 2.11 illustrates the two growth stages. In the first stage, the product phase nucleates at the interface, typically at triple junctions of grain boundaries [27]. Since the nuclei are isolated and the interface is not fully covered, the process is interface controlled and can be described with equation 2.18. With further reaction progression, the nuclei grow parallel to the interface since the diffusion length of Ni and Al is the shortest. The first stage is finished when the nuclei impinge and the reaction rate decreases. In a second step, the product phase layer grows perpendicular to the interface. This process is diffusion-controlled and can be described with equation 2.19. With the increasing thickness of the product phase, the diffusion flux slows down and the growth rate decreases until the reactants are consumed.

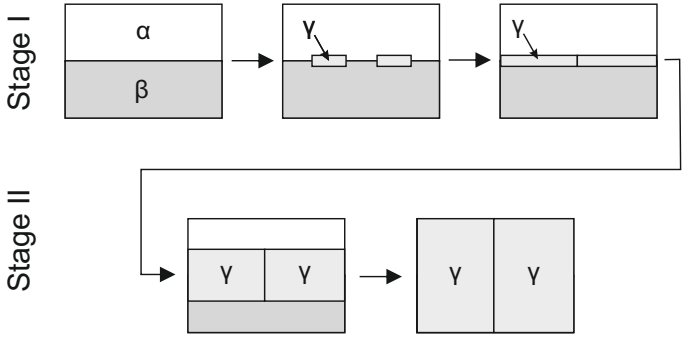

Figure 2.11: Under slow heating rate conditions, the product phase grows in two separated stages. In the first stage, the product phase γ nucleates and grows parallel to the interface until the individual grains impinge. In the second stage, the growth perpendicular to the interface dominates the phase transition. [70]

2.4.4 Parametrization of the growth kinetics

Generally, the kinetics of a chemical reaction, like phase formation, can be described with the reaction rate $d\alpha/dt$. Here, α describes the extent of conversion and takes on values between 0 and 1. Experimentally, α is determined by the fraction of a physical quantity, which changes during the reaction related to the overall change. Examples of such a physical quantity can be the exothermic heat in the case of calorimetry or the phase fraction in the case of X-ray diffraction experiments. For a thermally activated process, the reaction rate can be parametrized by [71]

$$\frac{d\alpha}{dt} = k(T)f(\alpha)h(P) \tag{2.20}$$

where $k(T)$ is the rate constant as a function of the temperature T, $f(\alpha)$ the reaction model and $h(P)$ a term which contributes to the pressure dependence. If no gaseous reactants are involved in the reaction, the pressure dependence $h(P)$ is negligible. For a single-step reaction, equation 2.20 is simplified to

$$\frac{d\alpha}{dt} = k(T)f(\alpha) \tag{2.21}$$

Therefore, the reaction rate is only dependent on the variables T and α. A reaction does not necessarily comprise only one reaction step. Instead, the reaction rate is described by the sum of the individual reaction rates in the case of multiple reaction steps. To account for the temperature dependence, $k(T)$ is described with an Arrhenius equation comparable to equation 2.9

$$k(T) = A\exp\left(\frac{E_a}{RT}\right) \tag{2.22}$$

Table 2.2: Kinetic models for solid-state reactions [72]

Code	**Reaction model**	$f(\alpha)$	$g(\alpha)$
A2	Avrami-Erofeev	$2(1-\alpha)[-ln(1-\alpha)]^{1/2}$	$[-ln(1-\alpha)]^{1/2}$
D1	1D-diffusion	$1/2\alpha^{-1}$	α^2
D2	2D-diffusion	$[-ln(1-\alpha)]^{-1}$	$(1-\alpha)ln(1-\alpha)+\alpha$
D3	3D-diffusion	$\frac{3/2(1-\alpha)^{2/3}}{1-(1-\alpha)^{1/3}}$	$[1-(1-\alpha)^{1/3}]^2$
F0	Zero-order reaction	1	α
R2	Contracting cylinder	$2(1-\alpha)^{1/2}$	$1-(1-\alpha)^{1/2}$
R3	Contracting sphere	$3(1-\alpha)^{2/3}$	$1-(1-\alpha)^{1/3}$

where A is the pre-exponential factor, E_a the activation energy, R the general gas constant and T the temperature. The reaction model $f(\alpha)$ describes the reaction rate dependent on the reaction progression. It is a mathematical description based on a mechanistic assumption that describes the observation in

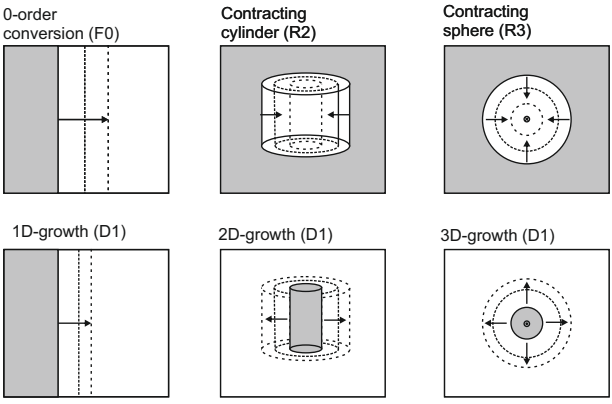

Figure 2.12: Illustration of selected solid-state kinetic models of Table 2.2.

the experiment. Depending on the geometrical shape of the product phase and potential anisotropic diffusion behaviour, a large number of reaction models are available [72]. All reaction models can be classified into three major types: accelerating, decelerating and sigmodal models. A selection of reaction models relevant for this study are summarized in Table 2.2. Both the differential notation $f(\alpha)$, parametrizing the $d\alpha/dt$ (compare equation 2.20) and its integral notation $g(\alpha)$ are listed. Besides,a schematic illustration of the models is shown in Figure 4.9 [73].

2.4.5 Phase formation sequence

To predict the phase formation sequence in solid-state reactions, *Pretorius et al.* [74] proposed a concept which is based on the so-called effective heat of formation of the individual phases. A basic assumption is that the system wants to minimize the Gibbs free enthalpy ΔG. In consequence, phases with the highest heat of formation ΔH_f are favoured. In the case of the Al-Ni system, all values for the heat of formation are summarized in Table 2.1. However, the maximum value of ΔH_f is only reached when the composition of the multilayer thin-film sample equals the composition of the compound phase. If the composition deviates, the heat release is governed by the limited element. Then, the effective heat of formation $\Delta H_f^{'}$ is given by

$$\Delta H_f^{'} = \Delta H_f \times \frac{c_{eff}}{c_{com}} \tag{2.23}$$

where ΔH_f is the heat of formation, c_{eff} the effective concentration of the limiting element and c_{com} concentration of the limiting element in the compound. Here, c_{eff} is the predominant concentration at the interface. This composition may deviate from the total composition of the multilayer stack. The heat of formation is reduced when the effective concentration does not match the composition of the compound phase. Therefore, the effective concentration of the

limiting element determines the heat release. Figure 2.13 plots the effective $\Delta H_f^{'}$ as a function of the composition for all compounds in the Al-Ni system. However, considering the heterogeneous structure of a multilayer sample, the determination of the effective concentrations is difficult. Processes at the interface take place under highly non-equilibrium conditions and are influenced by numerous factors. For simplification, *Pretorius et al.* choose to take the composition with the highest mobility of Al and Ni atoms and, therefore, the most effective mixing. According to *Brown and Ashby* [71], the activation energy for diffusion in solids is lowest at the composition with the lowest melting temperature. Transferred to the Al-Ni system, this is the eutectic composition at 3.5 at.% Ni (see phase diagram in Figure 2.3). *Pretorius et al.* conclude that the first phase which is formed is the phase with the lowest value of $\Delta H_f^{'}$ at the composition of the eutectic with the lowest temperature.

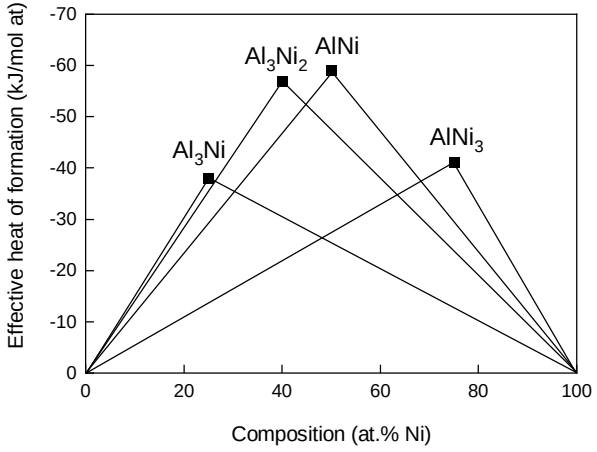

Figure 2.13: The effective heat of formation $\Delta H_f^{'}$ for the compound phases in the Al-Ni system. For the calculation equation 2.23 was used. The $\Delta H_f^{'}$ decrease proportional to the effective concentration of the limiting element related to the concentration of the limiting element in the compound phase. [74]

In the case of Al-Ni, this is the Al_3Ni phase, which is in good agreement with experimental results [13, 16, 17]. The next phase is formed at the Al_3Ni/Ni interface. The effective concentration moves further in the direction of the unreacted element, which is Ni. According to Figure 2.13, the next phase with the most negative heat of formation, which is richer in Ni, is the Al_3Ni_2 phase. This continues until the equilibrium AlNi phase is reached.

3 Methods

From an experimental point of view, the investigation of runaway reactions in reactive multilayer materials is challenging [5]. The combination of high heating rates (up to $\sim 10^6$ $\mathrm{K\,s^{-1}}$) and the low sample thickness of the reactive multilayer thin-films (less than 2 µm) impeded a detailed analysis in the past [12]. Therefore, like outlined in Section 1.1, the objective of this study is a comprehensive thermodynamic and structural characterisation of runaway reactions in Al/Ni multilayers. Conventional methods for thermal characterisation, like differential thermal analysis (DTA) or differential scanning calorimetry, lack the maximum heating rate, which is typically limited to < 5 $\mathrm{K\,s^{-1}}$ [75]. In the framework of this study, nanocalorimetry was chosen. This is a chip-based method that allows for heating samples at rates that are close to runaway conditions while a thermodynamic characterisation is realised [76]. For structural characterisation, methods based on X-ray or electron beam diffraction were considered. Dynamic transmission electron microscopy (TEM) was successfully combined with nanocalorimetry to characterise Al/Ni multilayers [20, 77]. However, limitations in the sensitivity of determining low amounts of phases did not allow for the quantification of the phase formation behaviour during rapid reactions [7]. Synchrotron X-ray diffraction studies of self-propagating reaction fronts could demonstrate an improved resolvability of product phases at heating rates up to 10^6 $\mathrm{K\,s^{-1}}$ [23, 78]. A major drawback of this methodical approach is the uncontrolled heating during the reaction. Based on these considerations, the combination of nanocalorimetry and synchrotron X-ray diffraction was evaluated as the most appropriate approach for characterising runaway reactions in Al/Ni multilayers. This method was already applied

to polymer materials [79–83] and metal-based materials [84–87]. Since the measurement frequency in these studies was limited to 50 Hz [81], a significant improvement of the temporal resolution is necessary for the application to reactive materials. Besides the adaption to reactive material, the focus was put on the increase of the temporal resolution to the µs-range to get more detailed insights into the reaction mechanisms. Since large parts of the method are self-developed, this section gives a detailed description of the technical implementation. First, the methodical aspects of nanocalorimetry are described in Section 3.1. The implementation of nanocalorimetry measurement at a synchrotron beamline is shown in Section 3.2. Finally, the microscopical methods used for *ex situ* microstructure analysis are described in Section 3.3.

3.1 Nanocalorimetry and adaption to reactive materials

Nanocalorimetry was developed to perform thermal characterization at heating rates > 10^3 $\mathrm{K\,s^{-1}}$ [76]. The first applications were the investigation of the melting point of nanometer-scale metallic thin-films [88–90]. This method was further extended to polymeric materials [91, 92], carbon-based materials [93] and reactive materials [11, 20]. Chip-based nanocalorimetry sensors are heated resistively while the temperature is tracked. The comparison with a reference measurement allows for the extraction of thermodynamic quantities like the heat capacity C_P or the reaction power $\dot{Q}_{rct}$. The main task in this study was the development and implementation of a nanocalorimetry setup that meets the requirements set by reactive materials, which are summarized in Table 3.1. These are a µs-time resolution, a maximum temperature of 1200 °C and heating rates up to 10^6 $\mathrm{K\,s^{-1}}$. It should be noted that also low heating rates down to 10 $\mathrm{K\,s^{-1}}$ are accessible. However, in this regime, the nanocalorimetry sensor can be only used for heat treatment of materials since the methodical-related lower

limit of measurement range is 10^3 $\mathrm{K\,s^{-1}}$. Besides this, the compatibility to *in situ* synchrotron XRD measurements and an openly accessible data processing were the main reasons for a decision against commercially available instruments, like the Flash DSC 2+ (Mettler Toledo, Columbus, USA). Based on these requirements, a non-differential, quasi adiabatic nanocalorimetry setup, which uses the sensor design of *Allen et al.* [88], was developed in-house.

Table 3.1: Specifications of the nanocalorimetry setup

Type	non-differential, quasi-adiabatic
Sensor design	based on *Allen et al.* [88]
Source mode	current controlled
Temperature accuracy	< 5 K
Measurement range	temperature: 25 - 700 °C
	heating rate: $10^3 - 10^6$ $\mathrm{K\,s^{-1}}$
Heating rate	controlled: $10 - 10^5$ $\mathrm{K\,s^{-1}}$
	uncontrolled: 10^6 $\mathrm{K\,s^{-1}}$
Data acquisition rate	200 kHz
Atmosphere	air, vacuum, inert gas
Other	compatibility to *in situ* synchrotron XRD

First, the nanocalorimetry sensors and the hardware are described in Sections 3.1.1 and 3.1.2. Section 3.1.3 provides a detailed description of the measurement principle and the post-measurement data treatment. Crucial for later investigations is a reliable calibration of the device. The temperature calibration and the thermodynamic calibration procedure is described in Section 3.1.4 and Section 3.1.5, respectively. Finally, an overview of the samples investigated and their fabrication is given in Section 3.1.6.

3.1.1 Nanocalorimetry sensor

The centrepiece of the nanocalorimetry measurement device is the sensor. The sensor combines two major functions: (i) controlled heating of the specimen and (ii) measurement of the specimen temperature. In this study, a sensor geometry based on the design of *Allen et al.* [88] was chosen. The schematic sketch of the sensor is depicted in Figure 3.1 (a). For detailed technical informations, refer to Appendix A.1.
The basis of the sensor is a 500 µm-thick silicon frame. This serves as a support structure for a free-standing SiN_x membrane with the Pt heating strip on the top. The membrane acts as an electrical insulator between heater and specimen and ensures quasi-adiabatic measurement conditions. The latter one is achieved by the low thermal conductivity of the SiN_x and the low thickness of the membrane. The sensor is heated resistively by applying a current pulse $I(t)$ to the 75 nm-thick Pt heating strip. The thermal power input is given by $\dot{Q}_{app} = \Delta V \cdot I$, where ΔV is the voltage drop along the heating strip and I the applied current. For electrical contact, the four pads on the side of the sensor are used. The temperature of the heating strip is determined via the temperature dependency of the electrical resistance $R(T)$ of the heating strip. A four-point measurement enables an accurate determination of the sensor resistance. For this purpose, the voltage drop ΔV along the Pt heater is measured with two voltage probes [94]. Hence, the resistance is given by $R(T) = \Delta V / I$. With the aid of an initial resistance-temperature calibration (see Section 3.1.4), the temperature can be determined. Since the temperature between the voltages probes is measured, this area is called *active area*.

The design of the sensor exhibits two major advantages: (i) a large active area of 0.5×3.7 mm^2 and (ii) well-known sensor characteristics due to the extensive use in research [95]. On the one side, the size of the active area enables the temperature calibration using optical infrared (IR) pyrometry [96]. On the

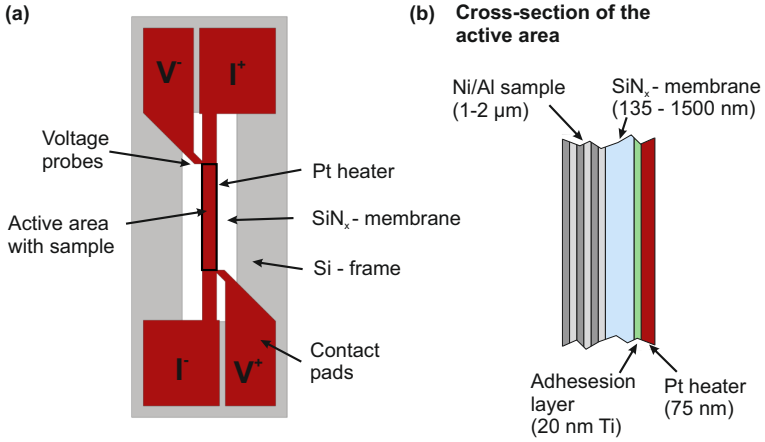

Figure 3.1: Schematic illustration of a nanocalorimetry sensor based on the design of *Allen et al.* [88]. (a) Top view of the sensor with the main components: SiN_x membrane, Pt heater and voltage probes for the resistance measurement. (b) Cross-section through the active area of the sensor. The Pt heater is electrically isolated from the Ni/Al multilayer specimen.

other side, the heater design is well suited for *in situ* X-ray diffraction experiments. An enlarged exposure area enhances the diffracted X-ray intensity and therefore lowers the resolution limit for phase detection.

Besides the geometrical aspect of the sensor, the material selection is crucial for the performance of the method. Sensor parameters like the sensitivity, temperature stability, mechanical stability and maximum heating rate are mainly determined by the materials [97]. Various metals like Ni, Ag, Au and Pt were tested in the past as a material for the heating strip [94]. In respect to the requirements in this study, Pt with a Ti adhesion layer was selected. The main reason for this is the superior temperature and oxidation stability of Pt [98]. The high melting temperature prevents the heating strip from microstructural

changes. Besides this, the value of the optical emissivity in the infrared spectrum $\varepsilon_{Pt} \approx 0.2$ is higher compared to the other metals [99–102]. This enhances the accuracy of the temperature measurement via IR pyrometry during calibration. Finally, the comparatively high specific resistance of 10.7 $\mu\Omega\,cm^{-1}$ of Pt is preferential since a lower magnitude of the current pulse is required. Thus, transient effects at the beginning and the end of the current pulse are reduced [94, 103]. A Ti adhesion layer was used to prevent delamination of the heater from the SiN_x membrane. It is reported that Ti is vulnerable to interdiffusion and oxidation [98, 104]. This was tackled by controlling the annealing process, which resulted in a stable microstructure. For the membrane, amorphous SiN_x was selected. The combination of decent mechanical strength, good heat conductivity (= 3.2 $W\,m^{-1}\,K$ [20]) and the electrical insulating properties make SiN_x the best suitable material for the membrane. For a more detailed discussion about the influence of the sensor geometry and the material selection, refer to related literature [76, 94, 105].

Table 3.2: Nanocalorimetry sensor layer thickness of SiN_x, Ti and Pt. The actual thickness values determined after the deposition deviate slightly from the targeted values.

SiN_x membrane (nm)		**Heating strip (nm)**	
Target	**Actual**	**Pt**	**Ti**
150	143	75	20
300	304	75	20
600	592	75	20
1000	–	75	20
1500	1494	75	20

To ensure consistent characteristics, the sensors were fabricated in a standardized photolithographic process in cooperation with the Department of Microsystems Engineering (IMTEK, Albert-Ludwigs-Universität Freiburg, Germany). All process steps are based on the NIST (National Institute of Standards and Technology, Gaithersburg, USA) recommendations for nanocalorimetry sensor production *Yi et al.* [95]. As the first step, a double-sided polished silicon wafer (d = 500 µm) was used as substrate material for the thermal growth of SiN_x on the front- and backside of the wafer. Next, the front side of the wafer was patterned in a photolithographic process to prepare the heater and contact pad structure. Ti and Pt were deposited on the top of SiN_x via E-beam evaporation. After a lift-off step, the backside of the wafer was patterned with the geometry of the sensor cavities. The free-standing SiN_x was fabricated by a two-step etching procedure. First, SiN_x was removed by reactive-ion etching (RIE) using CH_3. Second, Si was removed by potassium hydroxide (KOH) etching. As a final step, the sensors were glued on a supporting wafer for transportation and separated with a diamond saw cutting. Six different types of nanocalorimetry sensors were fabricated. An overview of the sensor types is given in Table 3.2. For all sensors the thickness of Pt and Ti was held constant at 75 nm and 20 nm respectively. The SiN_x membrane thickness was varied between 150 nm and 1500 nm to tailor the sensor characteristics. As listed in Table 3.2, the actual thickness of the SiN_x deviates slightly from the target value. Since the difference is negligible, the target values are used in the text to identify the type of sensor (e.g. a 300 nm–sensor).

After fabrication, all sensors passed through a cleaning and annealing process. For an accurate temperature measurement by IR pyrometry, a high surface quality of Pt is required. Contamination of the surface would alter the IR emissivity ε_{Pt}, which would result in a temperature error in the sensor calibration.

In order to avoid contamination, a defined sequence of cleaning steps were applied:

1) Removal of the sensors from the support wafer (24 h in acetone)
2) Separation of the sensors
3) Dissolution of the remaining adhesive (3 h in acetone)
4) Cleaning with isopropanol (3 h)
5) Cleaning with deionized water (3 h)
6) Drying of the sensor in an airstream

All steps were conducted in a laboratory hood to minimize dust contamination. After cleaning, all sensors were annealed. For optimal measurement conditions, a stable microstructure of the Pt heater has to be ensured. Changes in the electrical resistance during a nanocalorimetry scan by metallurgical effects, like grain growth, would cause unfavourable errors in the temperature measurement. *Yi et al.* [104] could show that the best results in terms of surface quality and electrical resistance are archived when the sensors are annealed at 700 °C for 1 h in air. The quality of the Pt surface topology was verified using scanning electron microscopy (SEM). Figure 3.2 (a) shows a decent surface roughness indicating Ti oxidation at the surface. Oxidation is desirable since this process stabilizes the surface condition. The cross-section of the Pt heater prepared by focused ion beam (FIB) is depicted in Figure 3.2 (b). Void formation and irregularities in the Ti-Pt interface results from interdiffusion and consequent oxidation of Ti.

The stability of the Pt heater membrane was validated by electrical characterisation of the sensor. Figure 3.3 plots V as a function of I of 10 individual sensors with a SiN_x thickness of 150 nm. Only minor variations were found between individual sensors. At a low current level below 9 mA, the voltage increases linearly with the current, which is characteristic for ideal ohmic behaviour. In this regime, a room temperature resistance R_0 of $15.62 \pm 0.29\ \Omega$ was

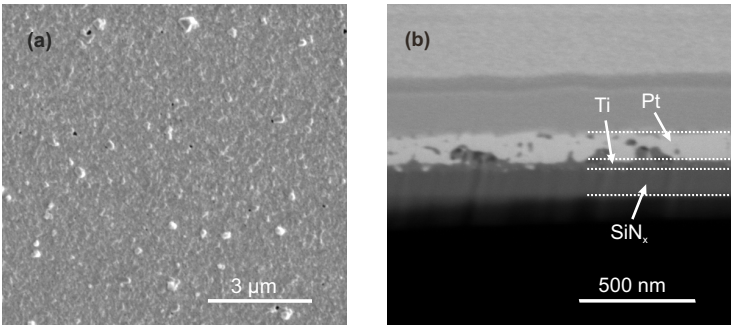

Figure 3.2: (a) Surface of the Pt heating strip after annealing at 700 °C for 1 h in air. Extrusions indicate oxidation of Ti. (b) Cross-section of the Pt heating strip with the SiN_x membrane at the bottom and the Ti adhesion layer in between. Void formation can is attributed to the diffusion and oxidation of Ti.

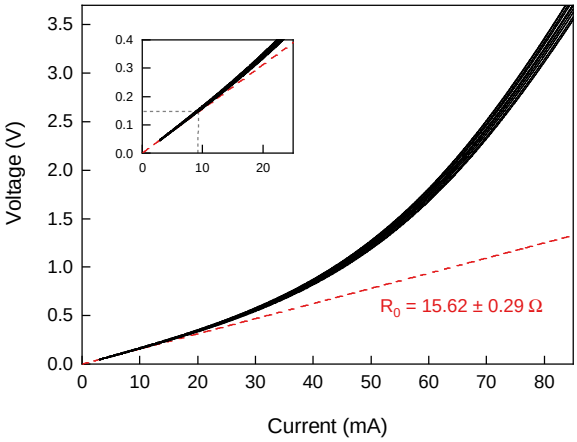

Figure 3.3: Voltage vs. current of 10 individual nanocalorimetry sensors with a membrane thickness of 150 nm. The ideal ohmic behaviour is represented with a dashed red line. Deviations from the linear behaviour are attributed to the resistance increase by self-heating of the sensor.

determined. Above 9 mA the slope of the $V-I$ curve (= sensor resistance) constantly increases. This is caused by self-heating of the nanocalorimetry sensor and the associated increase of the resistance. This principle is later used for temperature measurement. All resistance values of the sensors are summarised in Table 3.3. Depending on tshe membrane thickness, R_0 varies between 15 Ω and 25 Ω. It can be expected that there is no direct influence of the membrane thickness on R_0. However, parameters like the Pt thickness may vary between individual fabrication batches.Within one batch, the standard deviation of the resistance is typically less than 0.5 Ω.

Table 3.3: Room temperature resistance of the nanocalorimetry sensors

Membrane	**Batch # 1** R_0 (Ω)	**Batch # 2** R_0 (Ω)	**Batch # 3** R_0 (Ω)
150 nm	15.48 ± 0.37	15.62 ± 0.29	16.0 ± 0.33
300 nm	15.95 ± 0.34	15.85 ± 0.38	16.16 ± 0.35
600 nm	19.85 ± 0.68	–	–
1000 nm	16.02 ± 0.67	–	–
1500 nm	25.94 ± 1.12	–	–

A necessary condition for the reproducibility of nanocalorimetry measurements are stable $V-I$ characteristics for multiple successive measurements. By applying 20 current pulses up to 80 mA, the electrical stability was evaluated. Figure 3.4 plots the relative error of the resistance for successive pulses. Discrete current values of 5, 20, 40 and 80 mA were selected for comparison. For all current values, the corresponding resistance remains stable independent of the number of experiments. Only stochastic scattering of less than 1% was found. The more pronounced scattering at 5 mA is caused by the increased noise vulnerability of the setup at low current values. This corroborates the stable conditions of the Pt heater after annealing.

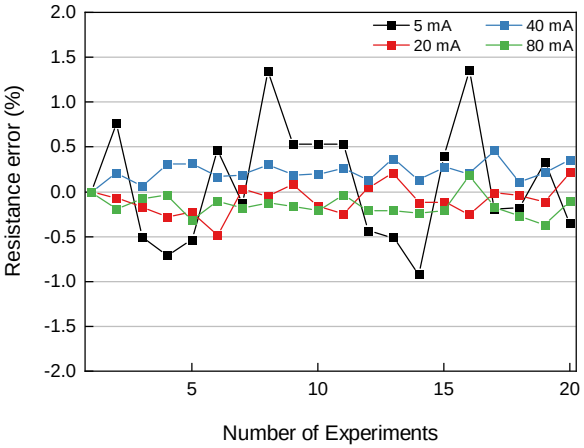

Figure 3.4: The electrical stability of nanocalorimetry sensors. The voltage error based on the first measurement was evaluated by multiple heating of one sensor. For all current values, the error remains independent from the number of experiments below 1%.

3.1.2 Nanocalorimetry setup

The main components of the nanocalorimetry setup are: (i) the sensor, (ii) the sensor XYZ-stage, (iii) the infrared pyrometer, (iv) the electronics and (v) the vacuum chamber. A schematic illustration of the setup is depicted in Figure 3.5. To perform experiments under different atmospheric conditions (e.g. air, vacuum or inert gas), all components besides the electronics are located inside the vacuum chamber. The sensor is attached upside-down at the sensor stage. The Pt heater is facing the IR pyrometer optics, which are located below the stage. This enables a temperature measurement directly on the heating strip, which is important for sensor calibration. The XYZ-stage allows the manual alignment of the sensor to the focal point of the infrared pyrometer optics. The Kleiber KG 740 – LO (Kleiber Infrared GmbH, Germany) broadband IR device is used as a pyrometer. The spectral range between 1.58 µm and 1.80 µm allows measurement of the temperature between 300 °C and 1400 °C.

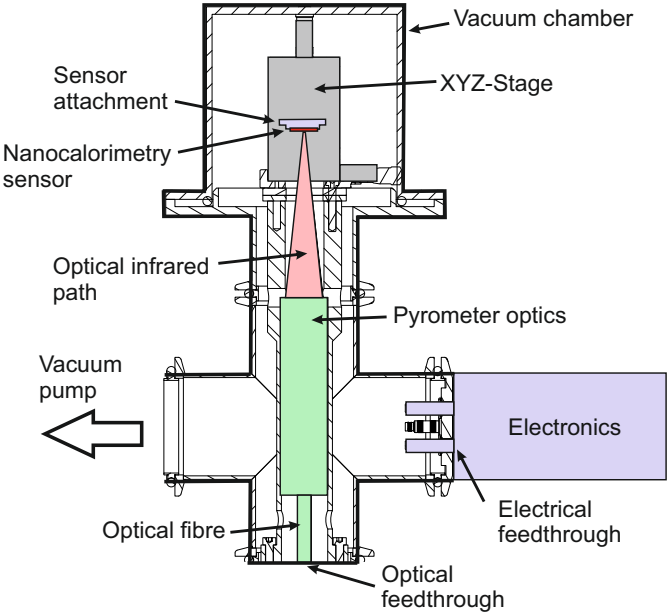

Figure 3.5: Schematic drawing of the nanocalorimetry setup. The main components are the nanocalorimetry sensor, the infrared pyrometer, the electronics and the vacuum chamber.

One key advantage of the pyrometer is the maximum measurement frequency of 167 kHz (= 6 µs). Thus, rapid temperature changes like they are characteristic for Al/Ni multilayer reaction can be resolved. Another key aspect is the small measuring spot diameter of 260 µm. The focal point can be positioned on the Pt heater (width = 500 µm) without capturing erroneous IR radiation from the surrounding. The pyrometer design allows the placement of the IR optics (Kleiber LVA 25 S - 3) inside the vacuum chamber. The connection to the auxiliary pyrometer electronics is realized with an optical fibre.

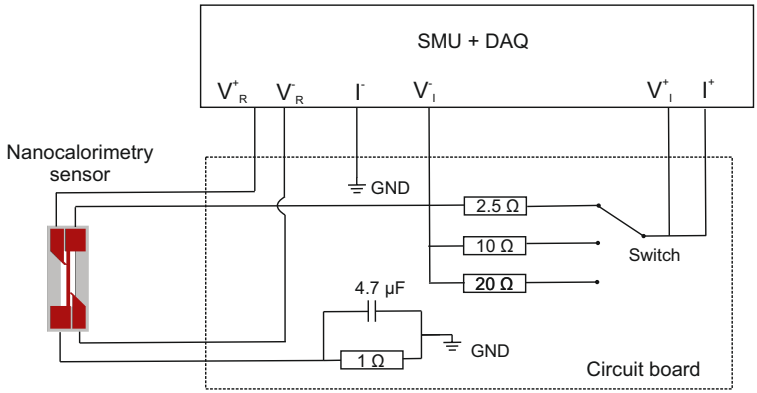

Figure 3.6: The electric circuit of the nanocalorimetry setup.

The standardized KF40 tubing was chosen for the vacuum chamber to ensure compatibility with other experimental setups, like X-ray diffraction. A turbopump in combination with a membrane pump (HiCube 80 Eco, Pfeiffer Vacuum Technology AG, Germany) is used to generate a vacuum with a pressure of less than $6.3 \cdot 10^{-5}$ mbar. However, measurements can also be conducted under atmospheric conditions.

The electric circuit that controls and reads out the data from the sensor is illustrated in Figure 3.6. To perform a nanocalorimetry scan, a current pulse is generated with a source measuring unit SMU (PXIe-4138, National Instruments, USA). The device operates in current-controlled mode with a peak current of 3 A (at 4 V), which is equivalent to 12 W. Current pulses with arbitrary shape are generated with a maximum output frequency of 20 kHz (= 50 µs). The sensor resistance is recorded with a four-channel 24 bit data acquisition module DAQ (PXIe 4464, National Instruments, USA). This is done by measuring

the voltage drop between V_R^+ and V_R^- in a 4-point measurement. The remaining two channels V_I^+ and V_I^- of the DAQ are used for the current measurement via a shunt resistor of either 2.5 Ω, 10 Ω or 20 Ω ($R_{error} = 0.1 - 0.5$ %). The voltage data are recorded with a maximum frequency of 200 kHz (= 5 µs). SMU and DAQ are installed in a rack equipped with a measurement computer (PXIe 8820, National Instruments, USA). Both devices are internally synchronized. The electrical contacting of the nanocalorimetry sensor is realized using spring pins (F708-11-B-085-G-80; Feinmetall GmbH, Germany). The spring deflection was held constant to ensure a reproducible contact resistance. Single-wire coaxial shielded cables connect the spring pins with the circuit board to prevent interference with external electromagnetic fields.

To perform experiments, a software program based on National Instruments LabVIEW 2014 was developed. Figure 3.7 provides an overview of the individual software functionalities, namely (i) configuration of the temperature pulse, (ii) import of the calibration data files, (iii) data acquisition and (iv) export of the result data file. The corresponding graphical user interface (GUI) is shown in Appendix A.2. Prior to each experiment, the user defines the shape of the temperature pulse by selecting the peak temperature, the heating time and the cooling time. By entering a sensor identifier, values for the temperature calibration $T(R)$, heat loss data $\dot{Q}_{loss}$ and the heat capacity of the sensor C_P (compare equation 3.1) are imported from a .xlsx file. Based on this, the current $I(t)$ for the predefined temperature pulse is computed. The system is designed to be externally triggered. This allows synchronisation with additional measurement devices. The experiment is started when an externally generated digital edge signal is detected. After the experiment, the collected U, I, R and T data are automatically exported into a .txt file.

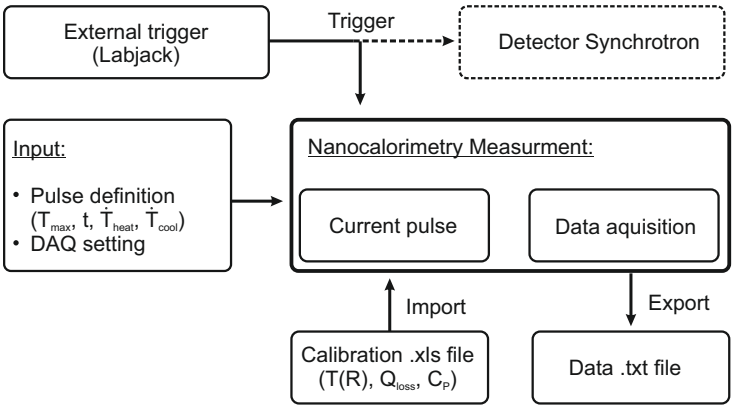

Figure 3.7: Organizational scheme of the nanocalorimetry software comprising: (i) configuration of the temperature pulse, (ii) import of the calibration data files, (iii) data acquisition and (iv) export of the result data file. After defining the temperature pulse and the sensor identifier, the calibration parameters are loaded and the current pulse is calculated.

3.1.3 Principle of measurement

Nanocalorimetry enables us to determine the fundamental thermodynamic quantities of interest, namely the heat capacity C_P and the reaction power $\dot{Q}_{rct}$ and characterizing a reaction pathway. The relation between these two quantities is given by the basic equation of the heat balance

$$C_P \cdot \dot{T} = \dot{Q}_{appl} + \dot{Q}_{loss} + \dot{Q}_{rct} \tag{3.1}$$

Here, $\dot{T}$ is the temperature rate, $\dot{Q}_{appl}$ the applied power and $\dot{Q}_{loss}$ the heat losses to the surrounding. The right side of the equation summarizes all types

of heat fluxes in the system. If $\dot{Q}_{appl} + \dot{Q}_{loss} + \dot{Q}_{rct} = 0$, the heat fluxes are balanced and the temperature of the system remains constant ($\dot{T} = 0$). Conversely, if an exothermic reaction takes place, $\dot{Q}_{appl} + \dot{Q}_{loss} + \dot{Q}_{rct} > 0$ and the temperature increases. The $\dot{Q}_{appl}$ in equation 3.1 can be directly determined in a nanocalorimetric scan via the current and the voltage signal $V = V_R^+ - V_R^-$. It is given by

$$\dot{Q}_{appl} = V \cdot I \tag{3.2}$$

The $\dot{Q}_{loss}$ in non-differential nanocalorimetry is determined by a nanocalorimeter scan at low heating rates, less than 20 $\mathrm{K\,s^{-1}}$ [7]. The basic idea is that at low heating rates, the left side of equation 3.1 approaches zero because $\dot{T} \approx 0$. In the absence of endothermic or exothermic reactions, like it is the case for reacted samples, $\dot{Q}_{rct}$ equals zero and the heat losses are given by

$$\dot{Q}_{loss} = \dot{Q}_{appl} \tag{3.3}$$

It is assumed that $\dot{Q}_{loss}$ is not a function of the heating rate, which is valid in the given heating rate regime.

The following analysis considers two cases. In the first case, a non-reactive sample is considered where $\dot{Q}_{rct} = 0$ and C_P is the only quantity unknown. In the second case of a reactive sample, both quantities of interest $\dot{Q}_{rct}$ and C_P are unknown and have to be determined simultaneously.

Non-reactive case: $\dot{Q}_{rct} = 0$

In the absence of endothermic and exothermic reactions, equation 3.1 is simplified and C_P is directly given by

$$C_P = \frac{\dot{Q}_{appl} - \dot{Q}_{loss}}{\dot{T}} \tag{3.4}$$

This case applies if there is no phase transition in the sample present or if an empty nanocalorimetry sensor is tested. An example of the latter case is presented in Figure 3.8 and 3.9. A 300 nm sensor was heated with a constant rate of 4,830 $\mathrm{K\,s^{-1}}$ to a peak temperature of 673 °C. The corresponding temperature signal (black line) and heating rate (red line) signal is shown in Figure 3.8 (a). The $\dot{Q}_{loss}$ and $\dot{Q}_{appl}$ vs. T data are plotted in Figure 3.8 (b). The difference between both power contributions is attributed to the thermal power which is required to fill up the heat capacities.

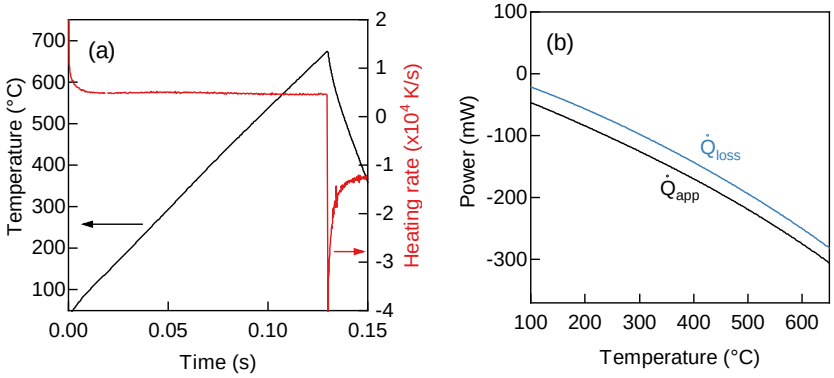

Figure 3.8: Determination of the heat capacity in the non-reactive case. (a) An empty sensor is heated with 4,830 $\mathrm{K\,s^{-1}}$ to a peak temperature of 672 °C. (b) The heat losses $\dot{Q}_{loss}$ are characterized by a subsequent second nanocalorimetry scan at 20 $\mathrm{K\,s^{-1}}$.

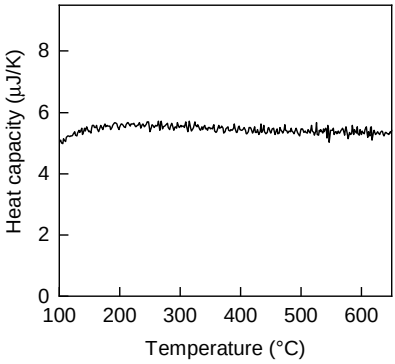

Figure 3.9: Heat capacity of an empty nanocalorimetry sensor with a membrane thickness of a 300 nm.

By applying equation 3.4, the heat capacity of the empty sensor can be calculated. The resulting C_P vs. T signal is plotted in Figure 3.9. The heat capacity is nearly constant over the whole temperature range, which is reasonable since no transition is expected. The transient regime below 150 °C is caused by deviations of the heating rate from the set value at low temperatures.

Reactive case: $\dot{Q}_{rct} \neq 0$

In the case of reactive samples, the previously described methodical approach has to be modified. To determine C_P and $\dot{Q}_{rct}$ simultaneously, a new method was developed [54]. A schematic overview of the method is given in Figure 3.10. The basic idea is that the heat capacity can be split into individual components:

$$C_P = C_{P,sensor} + C_{P,sample} + C_{P,rct} \tag{3.5}$$

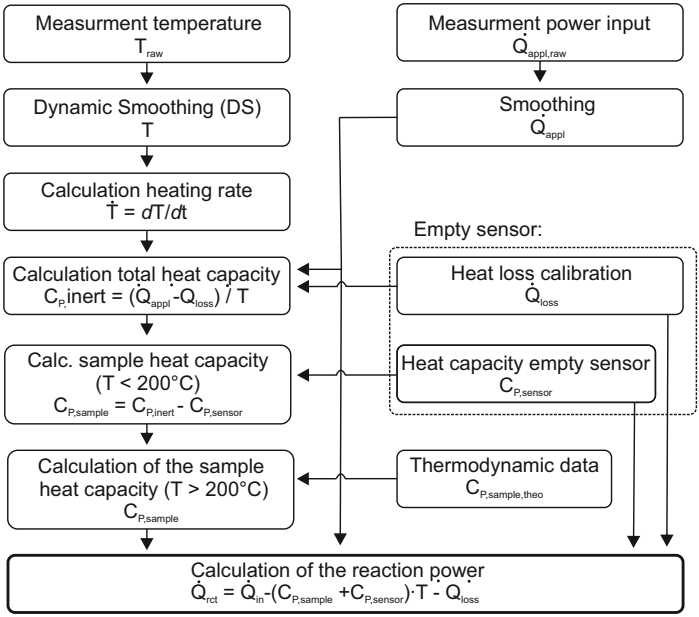

Figure 3.10: Overview of the nanocalorimetry data analysis procedure developed in his study. According to equation 3.1, C_P and $\dot{Q}_{rct}$ cannot determined simultaneously. In the first step, the quantities $\dot{Q}_{loss}$ and $C_{P,sample}$ are measured by applying an additional nanocalorimetric scans. In a second step, C_P is determined in a temperature regime where no reactions take place ($T < 200$ °C). Finally, $\dot{Q}_{rct}$ is calculated.

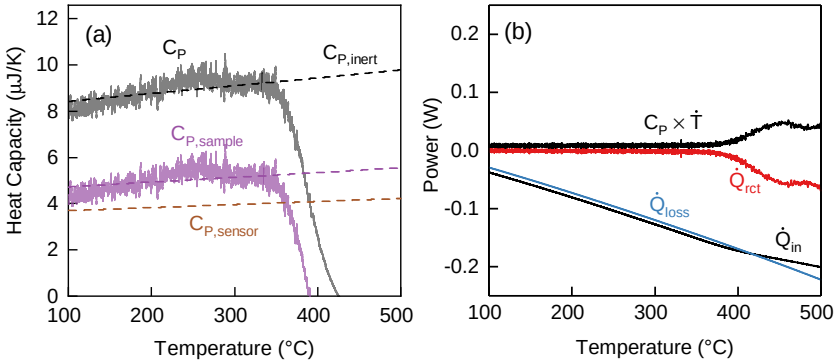

Figure 3.11: Heat capacity and power calculations in an exemplary nanocalorimetry experiment with a 10 at.% Ni sample heated with 10^3 $\mathrm{K\,s^{-1}}$. (a) To calculate the $C_{P,inert}$ (dashed black line) the signal is splitted into the $C_{P,sensor}$ and $C_{P,sample}$ components. Based on this, $C_{P,inert}$ is calculated for the whole temperature regime. (b) By applying equation 3.6 the $\dot{Q}_{rct}$ (red line) is calculated. The remaining power contribution $\dot{Q}_{loss}$, $\dot{Q}_{appl}$ and $C_P \cdot \dot{T}$ are plotted for comparison

Here, $C_{P,sensor}$ is the heat capacity of the nanocalorimetry sensor, $C_{P,sample}$ is the heat capacity of the sample and $C_{P,rct}$ the heat capacity change associated with exothermic or endothermic reactions. By defining the reaction-independent heat capacity $C_{P,inert}$, the reaction power can be calculated based on the heating rate signal:

$$\dot{Q}_{rct} = \dot{Q}_{appl} - C_{P,inert} \cdot \dot{T} - \dot{Q}_{loss} \tag{3.6}$$

with

$$C_{P,inert} = C_{P,sample} + C_{P,sensor} \tag{3.7}$$

To determine $C_{P,inert}$, a new approach is presented where different temperature regimes of the reaction are used. Below a critical temperature no exothermic reactions are expected and $C_{P,inert}$ can be measured directly. In case of Al/Ni reactive samples this temperature is below 200 °C [7, 11, 20, 77]. The heat capacity can be directly determined using the non-reactive equation 3.4. A typical C_P curve for a 2 µm sample with a Ni content of 10 at.% on a 150 nm sensor is shown in Figure 3.11 (a). The solid black line represents C_P, whereas the dashed black line represents $C_{P,inert}$. Above temperatures of 200 °C, $C_{P,inert}$ is not directly accessible because of the influence of exothermic reactions, which causes an additional contribution $C_{P,rct}$. To get $C_{P,inert}$ in this temperature regime the curve characteristics are calculated based on the physics of the system. Because of the non-linear temperature dependency of $C_{P,inert}$, a simple numerical extrapolation may cause a significant error. Therefore, the equation 3.7is used to determine $C_{P,inert}$ on the base of $C_{P,sensor}$ and $C_{P,sample}$. First, $C_{P,sensor}$ is measured by a separate nanocalorimetric scan of a similar sensor without sample. The resulting $C_{P,sensor}$ curve is illustrated with a dashed brown line in Figure 3.11 (a). To exclude an erroneous influence of the heating rate on the heat capacity, the equal temperature curve as in the nanocalorimetric scan with a sample is applied. Second, the temperature-dependent curve characteristics (slope) of $C_{P,sample}$ (dashed purple line) is calculated using thermodynamic literature data of Ni and Al [106]. For a complete description of $C_{P,sample}$ the y-axis interception (= weight-dependant heat capacity) is required. Therefore, the y-axis interception is determined by adjusting the calculated $C_{P,sample}$ curve to the experimental data in the non-reactive temperature regime (T < 200 °C). Based on $C_{P,sample}$ and $C_{P,sensor}$, $C_{P,inert}$ can be calculated for the whole temperature regime. Finally, equation 3.6 can be applied to calculate $\dot{Q}_{rct}$ in dependence of the temperature. The resulting $\dot{Q}_{rct}$ signal is shown as a red line in Figure 3.11(b). The reaction starts at 350 °C, indicated by a decrease of the reaction power. Beside $\dot{Q}_{rct}$, the remaining power contributions $\dot{Q}_{appl}$ (black line), $\dot{Q}_{loss}$ (blue line) and $C_P(T) \cdot \dot{T}$ (black line) are complementary plotted in Figure 3.11.

It has to be noted that an alternative method is reported in the literature which exploits the non-reversibility of the Al/Ni reaction. By performing a nanocalorimetric scan after the reaction (baseline scan), $\dot{Q}_{rct}$ can be determined [11, 91]. Since the irreversible reaction is completed after the first heating scan, $\dot{Q}_{rct} = 0$ in a subsequent temperature scan. The difference ΔT between both scans allows to cancel out $\dot{Q}_{loss}$ and C_P and calculate $\dot{Q}_{rct}$. However, the high heating rates of runaway reactions in the present study induce the rupture of the sensor membrane during the reaction. This impedes the measurement of a post-reaction baseline scan. Most likely, this can be attributed to residual stresses arising in the comparatively thick samples of 1-2 µm.

Postprocessing of the raw data is crucial for the determination of C_P and $\dot{Q}_{rct}$ in a nanocalorimetry measurement. In particular, the determination of $\dot{T}$ is highly sensitive to measurement noise. Smoothing routines are therefore crucial to maintain sufficient data quality. Since the smoothing of data always entails the loss of information, a certain effort has been made to optimize the process in this study. A standard Moving Average (MA) smoothing algorithm is compared to an optimized Dynamic Smoothing (DS) procedure. The main focus was the reduction of the measurement noise, while fast variations of the signal like they are characteristic during runaway reactions are reproduced accurately. Figure 3.12 shows a representative data set with a gradual increase of the temperature at the beginning, followed by a steep increase. It is evident that the MA algorithm fails at rapid temperature changes. Even for a reduced window size of 25 points, MA cannot reproduce the temperature data. The smoothed temperature curve is shifted to higher values and errors up to 20 °C occur. This makes an alternative approach inevitable. DS is based on a moving average algorithm, with a dynamically adjustable window size:

$$T_{DS}(t) = \frac{1}{n}\sum_{i=0}^{n-1} T(t-i) \quad with \quad \Delta T \leq T_{crit} \cup \Delta t \leq t_{crit}\,. \tag{3.8}$$

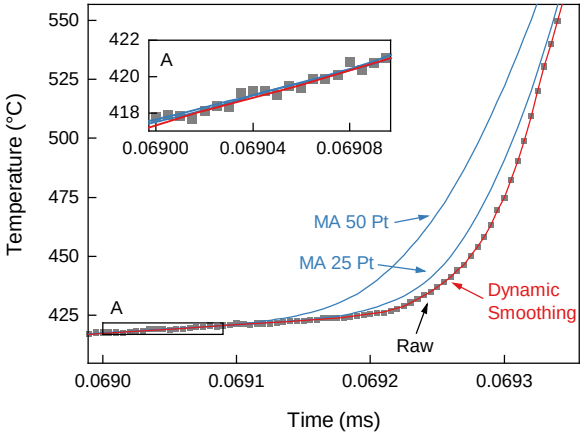

Figure 3.12: Smoothing of a nanocalorimetry temperature data set. A dynamic smoothing algorithm with adjustable window size (DS) is compared to a standard moving average (MA) procedure. Whereas DS shows a good performance for low heating rate regimes as well as rapid temperature changes, MA fails in the case of the latter one.

Here T is the temperature, n the dynamically adjustable window size, T_{crit} the maximum temperature change and t_{crit} the maximum duration per smoothing window. T_{crit} is defined so that it is well above the typical measurement noise. Below this limit, data points in a fixed time interval of typically 30 µs are averaged. If the limit is exceeded, the window is reduced to maintain the temperature criteria. In the case of very fast changes in the signal, all data points are taken to prevent the loss of information. Figure 3.12 proves the superiority of DS (red curve) at low heating rate regime as well as at fast temperature changes compared to ordinary smoothing procedures like MA.

3.1.4 Temperature calibration

The accuracy of the nanocalorimetry device is mainly dependant on the accuracy of the temperature measurement. Since the temperature is measured via the sensor resistance, the $T(R)$ calibration curve has to be determined. For this purpose, IR pyrometry was used to measure the heating strip temperature of the sensor [96]. Pyrometry was chosen since alternative methods like Raman spectroscopy [107] or calibration in a furnace [108] have the disadvantage of a low temperature accuracy or high time effort for calibration. This section first describes the calibration of the IR pyrometer, followed by the determination of the $T(R)$-sensor calibration curve. All calibration steps are summarized in Figure 3.13.

In the first step, the IR pyrometer device was calibrated. This is required since pyrometry is based on the measurement of the IR radiant power emitted from the material surface. The relation between radiant power $\dot{Q}_{rad}$ and T is given by the Stefan-Boltzmann law of radiation

$$\dot{Q}_{rad} = \varepsilon(T) \cdot \sigma \cdot A \cdot T^4 \tag{3.9}$$

where $\varepsilon(T)$ is the emissivity as a function of the temperature, σ the Stefan-Boltzmann constant and A the emitting surface area. Based on findings from the literature, the Pt emissivity is about 0.2 [99, 101, 102]. However, numerous parameters like surface roughness, surface contamination or oxidation may influence $\varepsilon(T)$. This impedes the usage of a general value for ε and makes calibration inevitable. In the following, instead of the physical quantity $\dot{Q}_{rad}$, the output voltage $V_{IR,0}$ of the pyrometer is used.

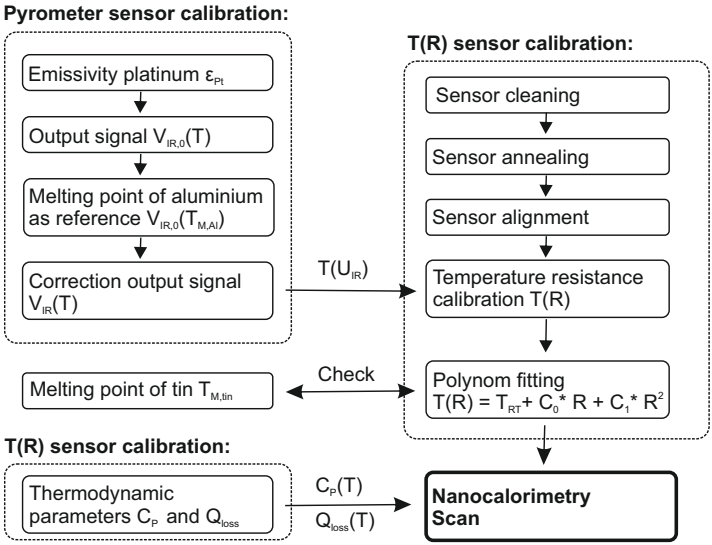

Figure 3.13: Overview of the calibration procedure for nanocalorimetry sensors. The $T(R)$ calibration is done by infrared pyrometry. Since pyrometry is vulnerable to surface conditions, an initial calibration of the pyrometer is performed.

The relation between $V_{IR,0}$ and temperature is given by

$$V_{IR,0} \sim C_\varepsilon \cdot T \quad \text{with} \quad C_\varepsilon = \varepsilon(T) \cdot \sigma \cdot A \tag{3.10}$$

where the coefficient C_ε summarizes all material and measurement parameters. The calibration setup shown in Figure 3.14 (a) was used to determine C_ε. The pyrometer optics is located above a custom-made heating stage. The sensor is placed on the top of the stage, covered by a metal plate to minimize temperature inhomogeneities. As shown in Figure 3.14 (c), a metal shielding with a centred hole is placed between the heating stage and optics. The temperature of the

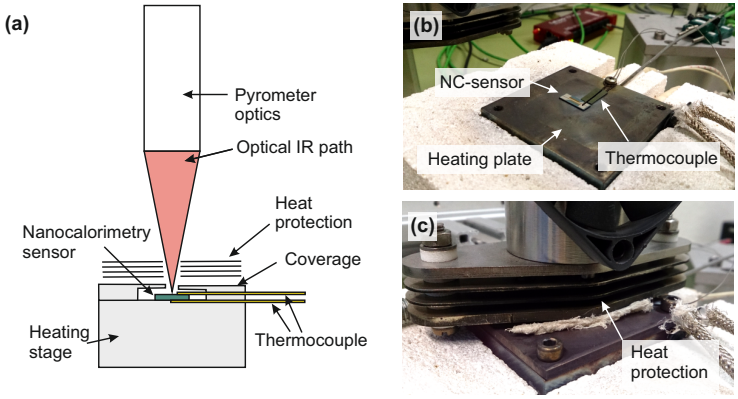

Figure 3.14: Experimental setup for the IR pyrometer calibration. (a) The pyrometer optics is placed above a nanocalorimetry sensor on the heating stage. The focal distance is equivalent to the application in the nanocalorimetry setup. (b) Two thermocouples at the top and the bottom of the sensor are used to record the sensor temperature. (c) To avoid heating of the pyrometer optics metal sheets are placed above the heating stage.

sensor is measured with two Ni-Cr (Type K) thermocouples. As depicted in Figure 3.14 (b), the thermocouples are placed below and above the sensor. Care was taken that the thermocouples were in direct contact with the sensor surface to minimize temperature errors. Since the thermocouples are placed in a hot surrounding, dissipation of heat through the sensor wiring and thereby a wrong temperature measurement can be excluded. Prior to the calibration run, the Pt heating strip of the sensor was carefully aligned with the focal point of the pyrometer.

For each calibration run the temperature of the heating stage was increased with a rate of 2-3 $\mathrm{K\,s^{-1}}$ to a peak temperature of 700 °C. The resulting $T(V_{IR,0})$ signal (black line) of the Pt heating strip is plotted in Figure 3.15. Above 400 °C, there is a almost linear dependency between T and $V_{IR,0}$. A slight oscillation

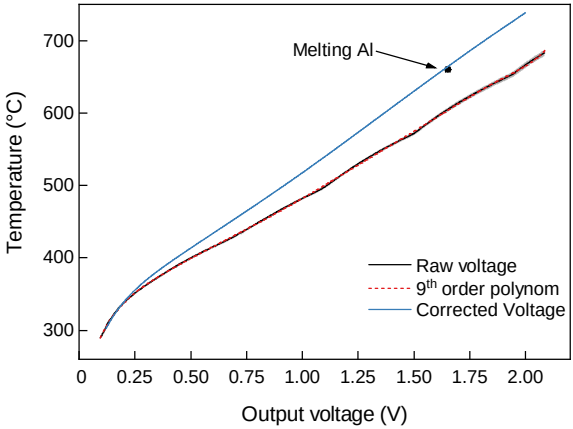

Figure 3.15: The temperature vs. the output voltage of the Pt heating strip obtained by IR pyrometry. The raw data (black line) is approximated by a 9th-order polynomial function (dashed red line). To compensate for the deviation from the reference measurement (= melting point of Al nanoparticles with T_m = 660 °C) the polynomial function was linearly corrected (blue line).

of less than 2 °C was observed. Most likely, this was caused by the non-linear characteristics of the pyrometer electronics. For further data processing, the dataset was approximated with a 9th-order polynomial function ($R^2 = 0.99987$). Tests have shown that a high-order polynomial function is most suitable to reproduce the device-specific waviness of the calibration curve. All sensors were calibrated in a temperature range between 290 °C and 700 °C. It was found that the majority of the sensor types have equivalent $T(V_{IR,0})$ characteristics. Only sensors with a membrane thickness of 1000 nm showed a 1.7% higher output voltage. To take this into account, this type of sensor was calibrated with a separated set of fitting parameters. Next, the obtained $T(V_{IR,0})$ was validated by melting experiments of Al nanoparticles (purity: 99.99%; d = 100–150 nm). In Figure 3.15 the resulting output voltage at 660 °C is marked with a black circle. It is evident that the melting temperature of Al is underestimated by

55 °C. To compensate for this error, the linear term of the polynomial function was corrected to match the melting temperature of Al. With a linear correction, the temperature error at the melting point of tin was found to be the lowest (see Figure 3.13). The resulting calibration curve is shown as a blue line in Figure 3.15. This systematic error is most likely caused by the size of the pyrometer focal point, which is considerably larger than the manufacturer's specifications. The corresponding measurements are shown in Appendix A.7.

Followed by the pyrometer calibration, the sensor $T(R)$ calibration is determined. For this purpose, the nanocalorimetry setup as shown in Figure 3.5 is utilized. The sensor is heated by a current pulse with a duration of 0.4 s, while the temperature is tracked in the measurement range of the pyrometer between 285 °C and 700 °C. For better statistics, three consequent heating scans were applied. The resulting T-R curve of an 300-nm-sensor is plotted in Figure 3.16(a). Prior to each scan, the sensor was aligned with the focal point of the pyrometer optics using the XYZ-stage. As shown in Appendix A.6, A.7 and A.8, misalignment in the x-,y- or z-direction may cause a significant temperature error. The dataset is fitted with a 2^{nd}-order polynomial function with a complementary boundary condition of R_0 at T_{RT} (green line). Compared to the linear fitting (R^2 = 0.966) represented by a red line, the 2nd-order poly fitting shows a a better match with the dataset (R^2 = 0.994). Non-linear $T(R)$ behaviour was also observed in other studies where an equivalent sensor design was used [95, 96]. This $T(R)$ calibration is performed on each sensor. Variations in the MEMS fabrication process (e.g. the Pt film thickness) result in deviations in the electrical response of the sensors.

The accuracy of the final T_{RT} was validated by melting experiments of Sn nanoparticles. Particles with a purity of 99.5% Sn and a particle diameter of <100 nm were chosen. For this purpose, 6 randomly selected nanocalorimetry sensors with a SiN_x membrane thickness between 135 nm and 1000 nm were taken. The nanoparticles were manually positioned in the active area

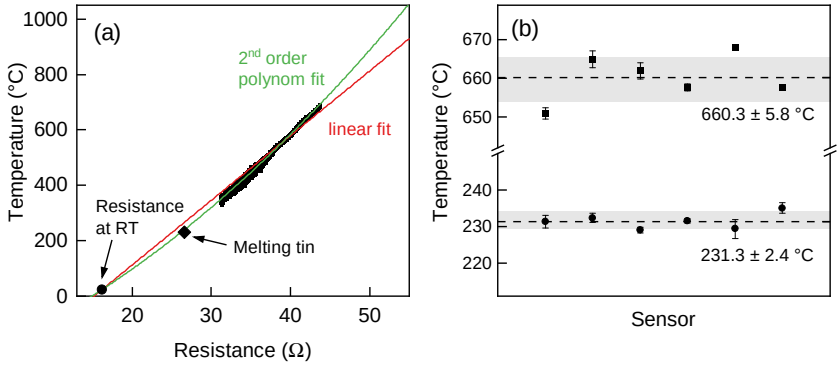

Figure 3.16: (a) The resistance-temperature calibration of a nanocalorimetry sensor (SiN_x = 300 nm). The black rectangle represent the IR pyrometry temperature data. (b) The temperature accuracy of 6 randomly selected sensors with a membrane thickness of 150 - 1000 nm were evaluated. For this purpose reference melting temperatures of Sn (T_m = 231.9 °C) and Al (T_m = 660.3 °C) nanoparticles were taken. A maximum stochastic error of 5.8 °C for Al was determined. The systematic error is less than 0.6 °C.

of the sensor. Care was taken that the particles were evenly distributed for a uniform melting behaviour. Prior to the calorimetric scan, the sensor was carefully heated in vacuum to melt the nanoparticles. Fast heating in air would provoke exothermic oxidation leading to a failure of the sensor membrane. The resulting melting temperature determined by nanocalorimetry is shown in Figure 3.16 (b). The Al melting experiments are also included. For Sn (T_m = 231.9 °C), an average melting temperature of 231.3 ± 2.4 °C was measured. For melting of Al (T_m = 660.3 °C) the temperature was 660.3 ± 5.8 °C. This is an excellent match with the literature values ($\triangle T < 0.6$°C). In both cases, the stochastic error depicted with the grey shaded area is less than 5.8 °C. This might be explained by the temperature resolution of the IR pyrometer and minor variations of the surface conditions of the Pt heater.

3.1.5 Thermodynamic characterization of the nanocalorimetry sensors

For an accurate thermodynamic investigation of the transformation behaviour of a sample, the sensors have to be thoroughly characterized. The demands on accuracy in the case of non-differential nanocalorimetry are mainly related to an accurate assessment of the heat losses. A 'heat leak', which describes an undetected heat flow in the system, must be excluded [109]. Additionally, the thermodynamic quantities of the sensor are required to calculate the temperature pulse used for the experiment. To ensure a nanocalorimetric scan at a constant heating rate, $\dot{Q}_{loss}$ and C_P of sensor and sample have to be precisely determined. Aside from these methodical aspects, the latter can be used to understand how alterations of the sensor, e.g. membrane thickness, will potentially affect the transformation kinetics of reactive materials [110]. The adjustment of the thermodynamic boundary conditions by the membrane thickness is one pathway to study this phenomenon and potentially tailor the reaction kinetics. The first part of the section deals with the heat losses of nanocalorimetry sensors. The second part focuses on the characterization of the heat capacity.

First, the influence of the sensor membrane thickness on the total $\dot{Q}_{loss}$ was characterized. This was done by heating and cooling the sensor at a low heating rate of 20 $\mathrm{K\,s^{-1}}$ so that $\dot{Q}_{appl} = \dot{Q}_{loss}$ (compare Section 3.1.3). In this study, three subsequent temperature ramps were performed to guarantee a sufficient database for $\dot{Q}_{loss}$. To avoid errors, only sensors of the same fabrication batch were taken to determine $\dot{Q}_{loss}$. For further processing, the raw $\dot{Q}_{loss}$ data were parametrized using a 4^{th}-order polynomial function.

Figure 3.17 (a) plots the heat losses as a function of temperature in vacuum ($p \leq 10^{-5}$ mbar). The sensor membrane thickness varies between 150 nm and 1500 nm. Each curve is based on the $\dot{Q}_{loss}$ data of three different sensors.

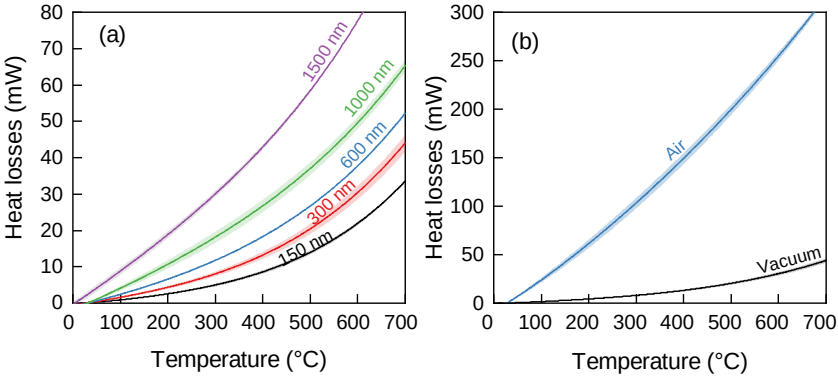

Figure 3.17: (a) The heat losses $\dot{Q}_{loss}$ of nanocalorimetry sensors in vacuum. The membrane thickness was varied between 150 nm and 1500 nm. $\dot{Q}_{loss}$ increase with membrane thickness. Above a temperature of 300 °C the $\dot{Q}_{loss}$ deviates from linear behaviour. (b) The heat losses of a 300 nm-thick sensor in air compared to vacuum. For each curve, three measurements were taken. The heat losses in air are about 10 times higher compared to vacuum.

It was found that for all membrane thicknesses under consideration, $\dot{Q}_{loss}$ increases with temperature. At low temperatures, there is a linear increase of $\dot{Q}_{loss}$. If the sensors exceed a temperature of ∼300 °C, $\dot{Q}_{loss}$ deviates from the linear behaviour, indicating the activation of an additional heat loss mechanism. With increasing sensor membrane thickness, higher values for $\dot{Q}_{loss}$ were found. This points to a correlation between membrane thickness and heat losses.

Figure 3.17 (b) plots $\dot{Q}_{loss}$ of a 300 nm-thick sensor in vacuum and in ambient air (T_{air} = 25 °C). It was found that $\dot{Q}_{loss}$ in air is about 10 times higher than under vacuum conditions. Especially at temperatures < 200 °C the differences between both atmospheres are pronounced. This corroborates that the heat losses of nanocalorimetry sensors are dominated by the atmospheric conditions.

For a more detailed understanding, the heat losses were split into their individual components. In general, there are three different heat loss mechanisms in nanocalorimetry sensors: (1) heat conduction through the membrane, (2) emission of infrared radiation and (3) convection by the surrounding atmosphere [92, 111–114]. The overall heat losses are given by

$$\dot{Q}_{loss} = \dot{Q}_{cond} + \dot{Q}_{rad} + \dot{Q}_{conv} \tag{3.11}$$

where $\dot{Q}_{cond}$ are the conductive heat losses, $\dot{Q}_{rad}$ are the radiative heat losses and $\dot{Q}_{conv}$ the convective heat losses. The individual components themselves can be described physically or numerically. The conductive heat losses are given by

$$\dot{Q}_{cond} = K_{cond} \cdot \Delta T = (k_{cond} \cdot A_c) \cdot \Delta T \tag{3.12}$$

where k_{cond} is the thermal conductivity of the material, A_c the cross-sectional membrane area surrounding the active area of the sensor and K_{cond} the thermal conductivity coefficient. The radiative heat losses are given by the Stefan-Boltzmann law

$$\dot{Q}_{rad} = K_{rad} \cdot T^4 = (\sigma_B \cdot A_s \cdot \varepsilon) \cdot T^4 \tag{3.13}$$

where σ_B is the Stefan-Boltzmann constant, A_s the area of the emitting surface, ε the surface emissivity and K_{rad} the average emissivity coefficient of the surface. In the case of the convective heat losses, a numerical description with a 4^{th} order polynomial equation was chosen. The reason for this is the complex nature of convection in air, which can only be described inadequately by analytical equations [109]. The convective heat losses are given by

$$\dot{Q}_{conv} = K_{conv,1} + K_{conv,2} \cdot \Delta T + K_{conv,3} \cdot \Delta T^2 + K_{conv,4} \cdot \Delta T^3 + K_{conv,5} \cdot \Delta T^4, \tag{3.14}$$

where $K_{conv,1}$–$K_{conv,5}$ are numerical convection coefficients and ΔT the relative temperature difference between sensor and surrounding. To split $\dot{Q}_{loss}$ into their components, $\dot{Q}_{cond} + \dot{Q}_{rad}$ (equation 3.12 and equation 3.13) was fitted to the vacuum heat loss dataset. This is based on the assumption that $\dot{Q}_{loss}$ in vacuum is only composed of conductive and radiative components, which is reasonable at a pressure below 10^{-5} mbar. In a second step, the experiments were repeated in air. To determine the convective heat losses, the previously determined conductive and radiative heat losses were subtracted:

$$\dot{Q}_{conv} = \dot{Q}_{loss} - \dot{Q}_{cond} - \dot{Q}_{rad}. \tag{3.15}$$

The individual components of $\dot{Q}_{loss}$ for nanocalorimetry sensors with a membrane thickness between 150 nm and 1500 nm are shown in Figure 3.18 (a)-(c). Each curve is based on three randomly selected sensors. The corresponding values for K_{cond}, K_{rad} and K_{conv} are summarized in Table 3.4. The radiative heat losses in Figure 3.18 (a) show no systematic dependence on the sensor membrane thickness. This finding is in good agreement with equation 3.13, which states that $\dot{Q}_{rad}$ is independent of the membrane thickness. Instead, $\dot{Q}_{rad}$ scales only with the size of the heated surface area and the temperature. Up to a temperature of 300 °C there is almost no contribution of radiation to $\dot{Q}_{loss}$. At elevated temperatures, the radiation contribution increases rapidly with a T^4-dependency. Between different membrane thicknesses, only minor differences of $\dot{Q}_{rad}$ were found. In contrast, $\dot{Q}_{cond}$ plotted in Figure 3.18 (b) shows a systematic influence of the membrane thickness of the sensor. Since the lateral dimensions are equal for all types of sensors, only the increase in thickness

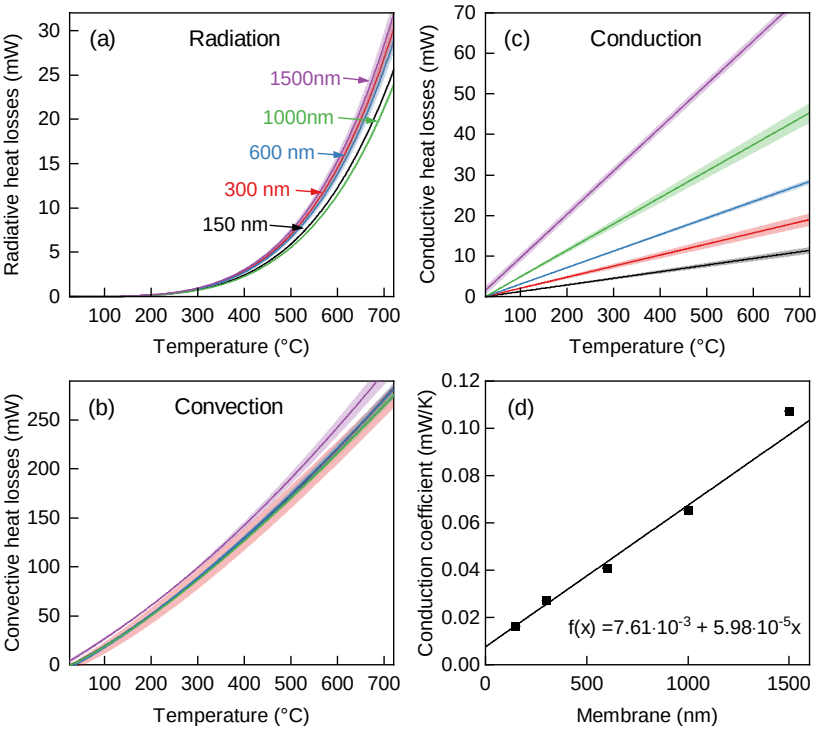

Figure 3.18: The individual heat loss components of nanocalorimetry sensors with a membrane thickness between 150 nm and 1500 nm. (a) The radiative heat losses show a T^4-dependency of the temperature. (b) In contrast, the conductive heat losses increase with membrane thickness. (c) The convective heat losses are not dependent on the membrane thickness. (d) The slope of the conductive heat loses scale linearly with the membrane thickness.

Table 3.4: Conductive, convective and radiative heat loss coefficients of nanocalorimetry sensors with different SiN_x membrane thicknesses d.

Heat loss mechanism	**Coefficient**	**Value**
Radiative	K_{rad}	$(9.88 \pm 0.0000143) \times 10^{-11}$
Conductive	$K_{cond,1}$	$(7.61 \pm 1.67) \times 10^{-3}$
	$K_{cond,2}$	$(5.98 \pm 0.35) \times 10^{-5} \times d$
Convective	$K_{conv,1}$	$(-7.12 \pm 2.81) \times 10^{-7}$
	$K_{conv,2}$	$(2.18 \pm 0.389) \times 10^{-8}$
	$K_{conv,3}$	$(4.20 \pm 0.000000158) \times 10^{-4}$
	$K_{conv,4}$	$(-3.65 \pm 0.000000237) \times 10^{-7}$
	$K_{conv,5}$	$(1.75 \pm 0.000000117) \times 10^{-10}$

contributes to the heat losses (compare equation 3.12). By plotting the slope as a function of the membrane thickness, as shown in Figure 3.18 (d), the linear dependency of the thickness is obvious. Because the membrane thickness can be accurately controlled in the manufacturing process, this parameter is most suitable to tailor the heat losses of nanocalorimetry sensors. Finally, the convective heat losses depicted in Figure 3.18 (c) begin to rise from T_{RT} on. The linear coefficient $K_{conv,2}$ in equation 3.14 dominates the functional dependence of $\dot{Q}_{conv}$. Within the standard deviation, no differences between the various membrane thicknesses could be identified. For all types of heat losses, the standard deviation within one membrane thickness batch lies within the measurement uncertainty of the method. This confirms the reproducibility of the experimental conditions under air.

For a better visualization, the fractions of $\dot{Q}_{rad}$, $\dot{Q}_{cond}$ and $\dot{Q}_{conv}$ of the total $\dot{Q}_{loss}$ are shown in Figure 3.19. Here, exemplarily a 150 nm sensor was chosen. As shown in Figure 3.19 (a), the heat losses under vacuum conditions are dominated by conduction through the sensor membrane. Below 300 °C, $\dot{Q}_{rad}$ hardly

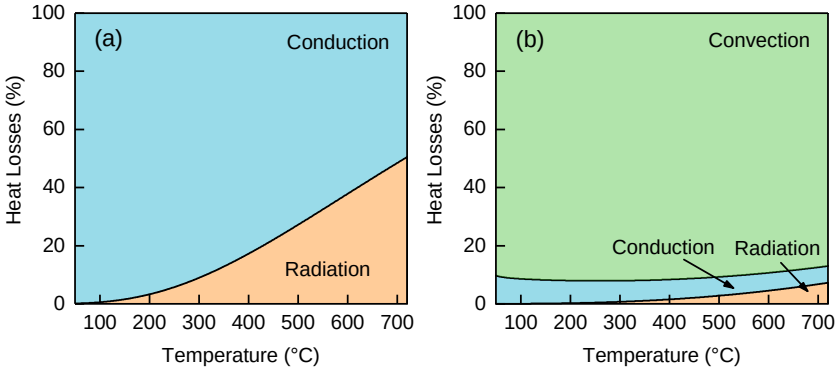

Figure 3.19: The proportion of the conductive, convective and radiative heat loss components exemplary for a 150 nm-thick nanocalorimetry sensor. (a) Conductive heat losses are dominating in vacuum. (b) In air, conduction and convections have a minor impact and hardly exceed 20% of the total heat losses.

exceeds 10%. The proportion is rising up to ∼50% at a temperature of 700 °C. The same measurement in air is depicted in Figure 3.19 (b). The comparison reveals the minor role of conduction as well as radiation when convection is present. Over the whole temperature regime, both components hardly exceed 20% of the total losses. The air circulation by convection is an efficient way for the heat transport from the sensor to the surrounding.

Besides the heat losses, the second thermodynamic quantity which characterizes nanocalorimetry sensors is the heat capacity. Nanocalorimeric scans at a constant heating rate of $5 \cdot 10^3$ K s^{-1} were performed to determine C_P. For this purpose, the non-reactive analysis (empty sensor or non-reactive sample with $\dot{Q}_{rct} = 0$) procedure described in Section 3.1.3 was applied. Since the C_P signal in Figure 3.9 shows only a negligible temperature dependency, a representative value of C_P was determined by averaging between 200 °C and 700 °C. The resulting heat capacity as a function of the membrane thickness is plotted in Figure 3.20. The blue rectangles represent the heat capacity of the sensor in

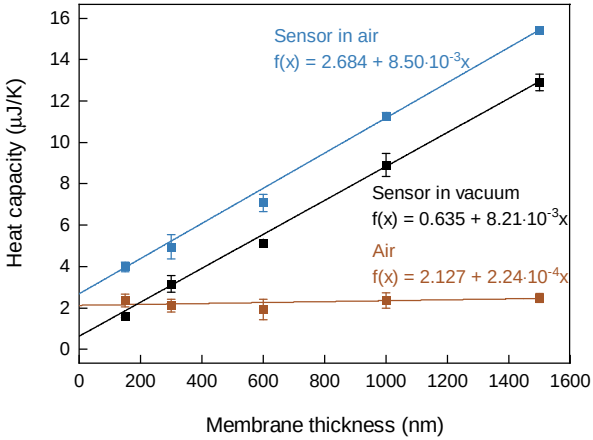

Figure 3.20: Heat capacity $C_{P,sensor}$ of nanocalorimetry sensors as a function of the membrane thickness. A linear increase of the $C_{P,sensor}$ is detected with increasing thickness of the sensor membranes. In case of air, $C_{P,sensor}$ is increased of about $2.2 \pm 0.2\ \mu J\,K^{-1}$. This can be attributed to the heat capacity of the surrounding air.

air $C_{P,sensor,air}$ and the black rectangles represent the heat capacity in vacuum $C_{P,sensor,vac}$. Each data point is calculated using individual C_P values of three different sensors. Each data set was approximated by linear curve fitting. The y-axis intercept B_0 and the slope B_1 of the fitting curves are summarized in Table 3.5. Independent of the atmospheric conditions, C_P scales linearly with the membrane thickness. Hence, the heat capacity increases proportionally to the volume of the active area of the sensor. In the case of air, $C_{P,sensor,air}$ is shifted to higher values.

The difference between $C_{P,sensor,air}$ and $C_{P,sensor,vac}$ plotted in brown rectangles shows a behaviour independent from the membrane thickness. A heat capacity of C_P of $2.2 \pm 0.2\ \mu J\,K^{-1}$ was determined. The most likely explanation is that the surrounding air, which is in direct contact with the sensor, is also heated causing an additional contribution of C_P. Since C_P defines the thermal inertia

of the sensor (see equation 3.1), thinner membranes enable higher heating rates. Practically, even for membrane thickness of 1,500 nm and a sample thickness of 2 µm (see Section 3.1.6), heating rates well above 10^4 $\mathrm{K\,s^{-1}}$ were archived. It should be noted, that no temperature dependency of C_P was observed. As it can be seen from the C_P signal shown in Figure 3.9, the heat capacity is almost constant over the entire temperature range.

Table 3.5: Heat capacity coefficients

Atmosphere	**Coefficient**	**Value**
Air	$B_{0,air}$	2.68 ± 0.17
	$B_{1,air}$	$(8.50 \pm 0.28) \cdot 10^{-3}$
Vacuum	$B_{0,vac}$	0.64 ± 0.12
	$B_{1,vac}$	$(8.21 \pm 0.12) \cdot 10^{-3}$

Besides empty sensors, sensors with samples were calibrated. The results are not shown here since the sample has only a negligible influence on the heat losses. The relationships, as shown in Figure 3.18, are also valid for sensors with a sample. However, the temperature ramps to determine $\dot{Q}_{loss}$ were slightly modified. First, the sample was heated to 700 °C to ensure that the reaction of Al/Ni is completed and no $\dot{Q}_{rct}$ affects the measurement. Second, a lower limit of the temperature ramps of 150 °C was set to prevent the sensor membrane from failure. The failure of the sensor membrane during cooling was typically observed during the calibration of sensors with samples. Most likely, this is caused by intrinsic stresses inside the reacted Al/Ni sample.

3.1.6 Sample deposition

The Al/Ni multilayer samples were deposited using magnetron sputtering. This physical vapour deposition technique allows the fabrication of thin-films with a defined layer thickness directly on the nanocalorimetry sensors. A detailed description of the method can be found in *Kiyotaka et al.* [115]. Most of the samples in this study were fabricated in cooperation with the Institute for Applied Materials-Applied Materials Physics (IAM-AWP, Karlsruhe Institute of Technology KIT, Karlsruhe). For this purpose, a Leybold Z 550 magnetron sputter coater (Leybold GmbH, Germany) was applied. The corresponding deposition parameters are summarized in Table 3.6. In the deposition process, Al and Ni targets with a purity of 99.999% were used. High purity Ar with a base pressure of $2{\cdot}10^{-4}$ Pa served as sputter gas. The Al and Ni layers were deposited with a growth rate of 0.35 $\mathrm{nm\,s^{-1}}$ for Al and 0.65 $\mathrm{nm\,s^{-1}}$ for Ni. Figure 3.21 shows a optical microscopy image of an Al/Ni sample deposited on a 150 nm-thick nanocalorimetry sensor. The sample is deposited on the backside of the sensor to avoid electrical contact with the Pt heating strip. Care was taken that the sample size was restricted to the 'active area' of the sensor. For this purpose, a shadow mask was developed. Prior to all deposition runs, the deposition rate was calibrated with a Si wafer as a substrate material to ensure the accuracy of the thin-film thickness. Besides the deposition at the IAM-AWP, selected multilayers were fabricated in cooperation with the Weihs group at the Johns Hopkins University (JHU, Baltimore, USA). These samples differ in chemical composition. For fabrication reasons, instead of pure Ni, Ni with 7 wt.% V was used as target material. Since 7 wt.% V may have an impact on the reaction mechanism, this type of multilayer was only used for investigations of the heat losses on the reaction kinetics. The deposition parameters used are summarized in Table 3.21.

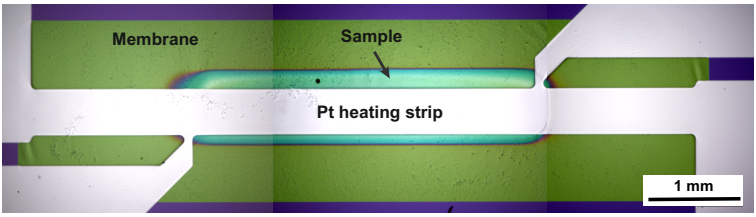

Figure 3.21: Optical microscopy image of an Al/Ni multilayer sample deposited on a nanocalorimetry sensor. For positioning of the sample a shadow mask was used.

Table 3.6: Parameters for the magnetron sputter deposition of the Al/Ni multilayer samples

Parameter	**IAM-AWP** [a]	**JHU**[b]
Device	Leybold Z 550	Custom-build
Target size	8 in	10×5 in
Materials	Ni, Al	Ni(V), Al
Power	Al: 250 W	Al: 570 W
	Ni: 300 W	Ni(V): 250 W
Base pressure	$2 \cdot 10^{-4}$ Pa	$3.3 \cdot 10^{-4}$ mbar
Ar pressure	$4 \cdot 10^{-1}$	$2.3 \cdot 10^{-2}$ Pa

[a] KIT, Institut für Angewandte Materialien - Angewandte Werkstoffphysik (IAM-AWP)
[b] Johns Hopkins University, Mechanical Engineering, Weihs Lab

The overall composition of the Al/Ni multilayers was varied between 5 at.% and 25 at.% Ni. At 25 at.% Ni, the concentration is equivalent to the stoichiometric composition of the $L1_2$ Al_3Ni compound with a formation enthalpy of -38 kJ (mol at)$^{-1}$ [74]. With this composition, a critical energy density of about $1 \cdot 10^3$ kJ cm^{-3} [6] for ignition of the sample was targeted. The Ni content was gradually reduced to 5 at.% Ni, to control the reaction kinetics and to reduce the peak temperature of the reaction. In this way, the phase formation kinetics can be potentially changed.

To study the influence of the multilayer geometry, the total film thickness and bilayer thickness were systematically varied. An overview of the sample parameters is given in Table 3.7. The first row shows the composition of the sample. The corresponding thickness of the individual Al and Ni layer is given in the second row. In the first column, the nanocalorimetry membrane thickness is enlisted. In the other rows, the total sample thickness in nm is given. Samples indicated with an * symbol were deposited using a Ni(7 wt.% V) sputter target. Samples with either pure Ni and Ni(7 wt.% V) are indicated with an $^\diamond$ symbol. All samples were deposited with a total thickness of either 1 µm or 2 µm. This is equivalent to a sample mass of 7–14 µg. This brings two advantages compared to other nanocalorimetric studies [7, 11, 20, 77] where the sample thickness is 7–20 times lower. First, the exothermic heat of the reaction is sufficient to initiate a runaway reaction of the Ni/Al sample. Second, since *in situ* synchrotron experiments are performed (see Section 3.2), thicker samples enhance the diffracted X-ray intensity and allow measurements with increased temporal resolution in X-ray experiments. The thickness of the Ni layer was either 15 nm or 30 nm. Thinner layers would cause peak broadening in X-ray diffraction studies [48]. With regard to the overall sample composition, this results in a bilayer thickness Λ = 448 nm (= 5 at.% Ni), 220 nm (= 10 at.% Ni), 144 mm (= 15 at.% Ni), and 166 nm (= 25 at.% Ni). In addition, samples were prepared with Λ = 83 nm (= 25 at.% Ni) to study the effect of the bilayer thickness. Figure 3.22 shows a representative image in cross section of a Al/Ni

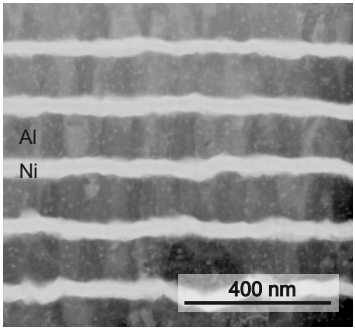

Figure 3.22: Cross-section (scanning transmission electron microscopy) of a 25 at.% Al/Ni multilayer sample with a Ni layer thickness of 30 nm and an Al layer thickness of 136 nm. The sample was deposited by magnetron sputtering.

multilayer sample on a nanocalorimetry sensor (here 30 nm Ni, 136 nm Al, 15 at.% Ni). The bright layers represent Ni and the dark layers Al.

In order to restrict the lateral sample size to the active area of the sensor, a shadow mask was developed. A non-magnetic stainless steel disc with a diameter of 150 mm serves as a baseplate. As shown in Figure 3.23 (a) 24 cavities for the positioning of the sensors are radially arranged on the backside of the plate. On the front side of the plate, openings for the incoming ion flux are provided. The geometry of the opening is illustrated in Figure 3.23 (b). It was found that the incidence angle of the incoming ion flux is $43 \pm 4°$. In order to restrict the lateral dimension of the sample to the size of the active area of the sensor (3.7×0.5 µm), the distance between the opening of the mask and sensor membrane had to be minimized. However, the contact between mask and membrane has to be excluded to avoid failure of the membrane. This problem was solved by spot welding 100 µm-thick metal sheets onto the baseplate. The sheet openings with a width of 500 µm were fabricated by sink erosion. As

Table 3.7: Overview of all Al/Ni multilayer samples deposited on the nanocalorimetry sensors. All values are given in nm

Membrane thickness	**5 at.% Ni** (Al:433 / Ni:15)	**10 at.%** (Al:205 / Ni:15)	**15 at.%** (Al:129 / Ni:15)	**25 at.%** (Al:68 / Ni:15)	**25 at.%** (Al:136 / Ni:30)
150	2000	2000	2000		500 *
					1000 *
					2000 ◇
300	2000	2000		1000 ◇	500 *
					1000
					2000 ◇
600					500 *
					1000 *
1000					2000
1500					500 *
					1000 *
					2000 *

* Samples with Ni(V)
◇ Two different sample types with Ni and Ni(V)

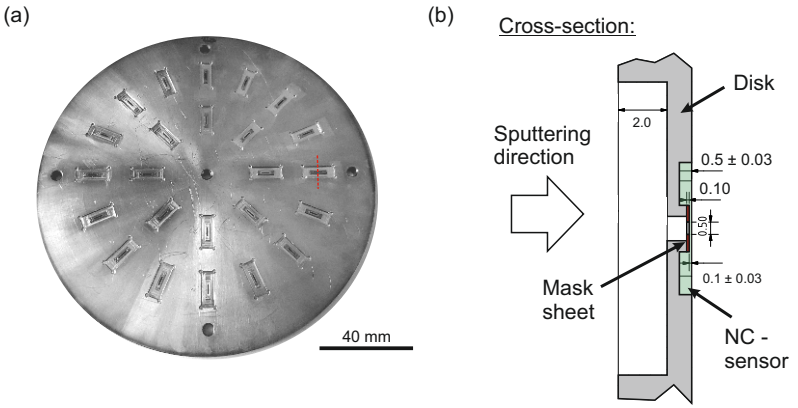

Figure 3.23: Shadow mask for nanocalorimetry sample deposition. (a) The shadow mask plate has 24 radially arranged cavities for sensor positioning. (b) Cross-section of the mask opening. The lateral dimension of the sample is restricted to the heating strip of the sensor. The technical drawing of the shadow mask is shown in Appendix A.3.

a result, a constant distance of 121 $\pm$ 30 µm between membrane and mask was achieved. Prior to deposition, each sensor was optically aligned to the mask opening and mounted with Kapton tape.

In summary, for the first time, nanocalorimetry has been adapted to the special requirements posed by runaway reactions in reactive multilayers (see Section 3.1.1). This includes a modular setup, which enables the adaption to *in situ* synchrotron measurements (see Section 3.1.2) and the extension of the method to µm-thick samples (see Section 3.1.6). A new analysis method, especially for non-reversible runaway reactions, was developed (see Section 3.1.3). Additionally, an extensive temperature (see Section3.1.4 and thermodynamic characterisation (see Section 3.1.5) was carried out to ensure the reliability of the method.

3.2 *In situ* synchrotron X-ray diffraction

Nanocalorimetry is used for a full thermodynamic characterisation of the transformations in the Al/Ni multilayers. One major goal of the present study is the *in situ* correlation of the thermodynamic analysis with the underlying structural mechanism. Due to the ms time scale where the transformations are expected to occur, this correlation represents a major challenge of the present study. For this purpose, nanocalorimetry was combined with synchrotron X-ray diffraction. Calorimetric quantities like exothermic heat can be directly correlated with the underlying structural transition. Comparable experimental setups were successfully used for polymeric materials [79–82, 82, 83, 116] and metallic glasses [84, 85, 87, 117–120]. However, for the very rapid reactions in reactive metallic multilayers ($\dot{T} > 10^7$ K s^{-1}) a time resolution in the µs-range is required. Up to now, the minimum attainable acquisition time was limited to 20 ms [81]. Therefore the major task in this study was the reduction of the acquisition time to resolve the transformations underlying the runaway reactions in Al/Ni multilayers. The section is structured as follows: first, the nanocalorimetry setup for synchrotron XRD is presented in Section 3.2.1. Section 3.2.2 is dedicated to the characteristics of the beamline and the X-ray detector. Finally, the post-experimental XRD data analysis is described in Section 3.2.3.

3.2.1 Experimental setup

The *in situ* XRD setup is based on the nanocalorimetry device described in Section 3.1. The nanocalorimetry sensor is positioned so that a transmission geometry of the X-ray beam is realized. The active area of the sensor is centred on the X-ray beam. The schematic drawing in Figure 3.24 illustrates the diffraction geometry. The focussed X-ray beam enters the vacuum chamber and is diffracted at the sensor and the sample. The sensor and the auxiliary electronics are identical to the *ex situ* setup. However, the vacuum chamber and sensor attachment was modified to perform simultaneous X-ray diffraction.

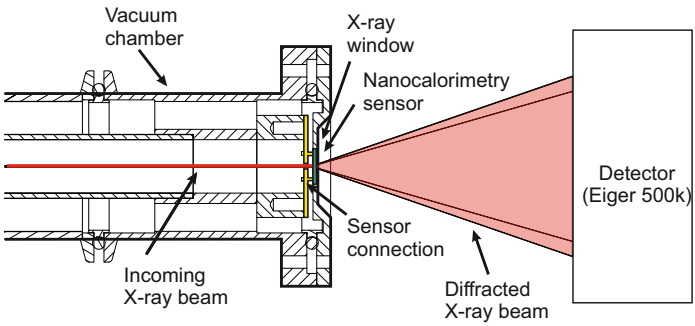

Figure 3.24: Schematical drawing of the nanocalorimetry setup for the *in situ* synchrotron X-ray diffraction experiments. The X-ray beam enters the vacuum chamber from the left side and is diffracted at the nanocalorimetry sensor placed in the sample holder. The diffracted X-ray intensities are recorded in an angular range between 13° and 31.5° by an 2D area detector.

The vacuum tubing is directly attached to the beamline optics. The sensor itself is placed in a sample holder, which is attached to the front end of the chamber. For experiments under vacuum conditions, a 150 µm thick Polyetherimide (Ultem®) foil, which is transparent for X-ray radiation seals the opening. Since most of the experiments were conducted in air, the window was skipped in order to decrease the XRD amorphous background signal for an improved signal-to-noise ratio.

The synchrotron beamline X04SA of the Swiss Light Source (SLS) at the Paul Scherrer Institute (PSI) in Villigen, Switzerland [121], was selected to perform the experiments. As an X-ray detector, the PSI developed 2D single-photon counting detector (Eiger 500k) was deployed. The detector was placed with an angular offset behind the setup to capture an angular range of 13° to 31.5°. The whole setup in operation is shown in Figure 3.25. A beam stop is placed

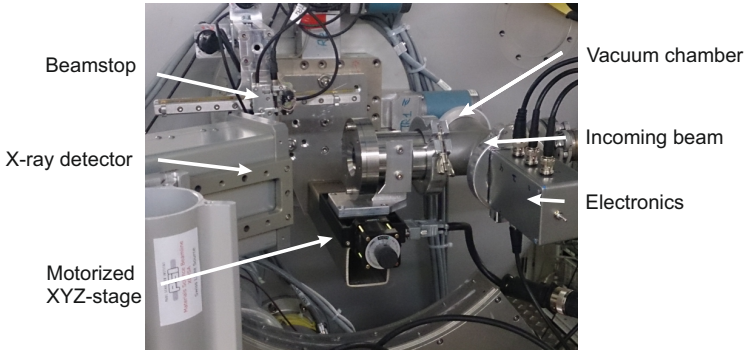

Figure 3.25: The *in situ* nanocalorimetry setup in operation at the X04SA powder diffraction beamline (SLS, PSI, Schwitzerland),

between sensor and detector to avoid damage to the detector by the incoming beam. Prior to all nanocalorimetric scans, the sensors are carefully aligned to the X-ray beam using a motorized XYZ stage.

3.2.2 Beamline and detector

The specification of the X04SA beamline of the Swiss Light Source (PSI, Switzerland) are summarized in Table 3.8 [121]. For all experiments, hard X-ray radiation with a beam energy of 12.6 keV (λ = 0.984 Å) was used in transmission geometry. This wavelength was chosen with respect to the X-ray absorption edge of Ni, Al and Pt since the X-ray beam passes through the Pt-heating layer of the nanocalorimetry sensor and Ni and Al of the multilayer sample. Typically, the beamline provides a constant flux of $> 10^{13}$ photons s^{-1}

at an energy resolution of $\Delta E/E = 1.4 \cdot 10^{-4}$ [121]. The beam size was restricted to the width of the sensor heating strip (D = 500 µm) to optimize the diffracted X-ray intensity.

Besides the photon flux of the X-ray source, the maximum temporal resolution of the setup is primarily defined by the detector. The specifications of the 2D area detector Eiger 500k (PSI, Villigen, Switzerland) are summarized in Table 3.9 [122, 123]. The detector was operated at an acquisition rate up to 23 kHz (t_{frame} = 45.5 µs). Depending on the experimental conditions, the acquisition was reduced to optimize the signal-to-noise ratio. The dead time was less than 5 µs, which allows quasi-continuous data acquisition. Measurements were recorded in a range of $13° < 2\theta < 31.5°$ with an angular resolution of 0.036° per pixel. Driven by the required high temporal resolution of Al/Ni runaway reactions, the detector performance was further improved by *Tinti et al.* [124]. This was done by reading out only selected areas of the detector. In this way, an acquisition rate of 73 kHz could be achieved. This is an improvement by the factor of 10^3 compared to other *in situ* nanocalorimetry experiments [81]. Beyond reactive materials, this development enables new methodical opportunities in various fields of research.

Table 3.8: Specifications of the X04SA beamline

Parameter	**Value**
Photon energy	12.6 keV
Flux at 12 keV	$> 10^{13}$ photons s^{-1} [121]
Energy resolution $\Delta E/E$	$1.4 \cdot 10^{-4}$ [121]
Focused spot size	500 µm × 500 µm

Table 3.9: Specifications of the Eiger 500k X-ray detector [122, 125]

Parameter	**Value**
Type	single photon counting, hybrid pixel detector
Pixel size	75×75 µm^2
Pixel array	$256 \times 256 = 65536$
Chip size	19.3×20 µm^2
Frame rate	23 kHz (73 kHz with detector area restriction)
Dead time	5 µs
Pixel counter	configurable (4, 8, 12 bit mode), binary, double buffered for continuous readout

The signal-to-noise ratio was evaluated for an empty nanocalorimetry sensor to evaluate the performance of the XRD setup. As reference, the Pt (200) diffraction peak at $2\Theta = 28.95°$ was taken. The diffracted signal in dependence of the acquisition rate f_{XRD} is shown in Figure 3.26 (a). The level of background noise is significantly increased at high f_{XRD}. At rates above 2 kHz, the Pt diffraction peak cannot be distinguished from the background noise. This points to the relation between the acquisition rate and the lowest amount of phase which can be detected. The resulting signal-to-noise ratio is plotted in Figure 3.26 (b). A continuous decrease with an increasing acquisition rate is observed. At a critical signal-to-noise ratio, a peak can no longer be distinguished from the background. Experience indicates that a signal-to-noise ratio of 3 is the lower limit for robust peak detection. In the case of the Pt(200) peak, this results in a maximum measurement frequency of 10 kHz.

In the next step, the phase resolution of Al_3Ni is considered. The Al_3Ni compound phase is of great importance for Al/Ni multilayer reactions [126]

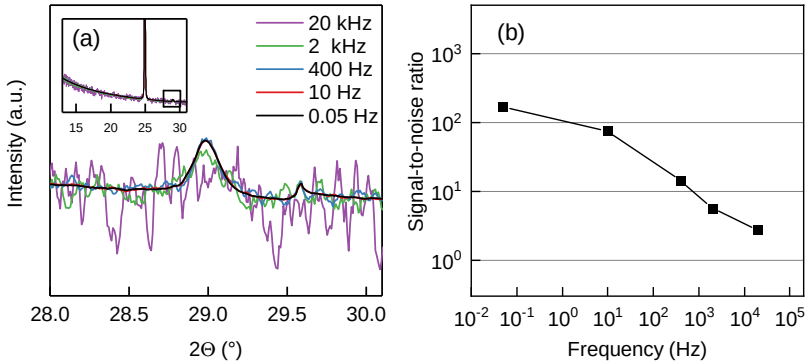

Figure 3.26: Signal-to-noise ratio as a funvtion of the detector frequency. (a) The Pt ($2\Theta_{Pt(200)}$ = 28.95°) peak of an empty nanocalorimetry sensor in dependency of of the detector acquisition rate f_{XRD}. Above 2 kHz the peak is hardly detectable. (b) The signal-to-noise ratio of the Pt peak decrease within increasing f_{XRD}. Below a ratio of 3, the peak is no longer detectable which is equivalent to a maximum frequency of f_{XRD} = 10 kHz.

and plays a central role in the kinetic analysis of phase formation (see Section 4.1.2). For the calculation, the Al_3Ni(111) peak, which is one of the most intensive peaks in the investigated spectra, was taken. To correlate the XRD peak intensity with the actual compound phase thickness, partly reacted samples were investigated. For this purpose, scanning transmission electron microscopy (STEM) was used to analyse cross-sections of post-reacted samples. As shown in Figure 3.27, based on the phase contrast in the high-angle annular dark-field image (HAADF), the amount of intermetallic phase was determined by graphical analysis.

Since the conditions for phase formation are consistent in the whole sample, the area of the intermetallic phase correlates directly with the volume fraction. Now, the integrated X-ray peak intensity can be correlated with the volume fraction of Al_3Ni. As outlined in detail in Section A.5, in this case it is a valid assumption that the peak intensity is equivalent to the amount of phase

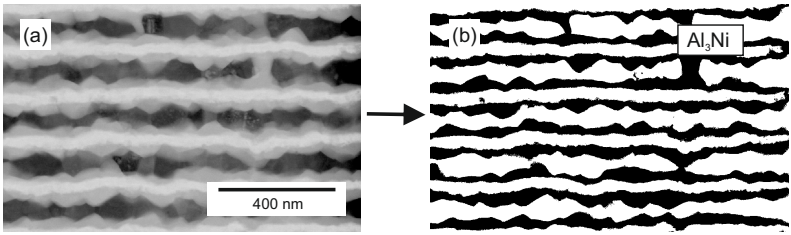

Figure 3.27: (a) Scanning transimission electron microscopy image of Al/Ni mulitlayer cross-sections. The sample was annealed at 317°C for 300 s. (b) Based on the phase contrast the amount of intermetallic phase (Al_3Ni) is determined.

in the sample. At a signal-to-noise ratio of 3, the minimum detectable peak height was computed. Broadening of the diffraction peak was taken into account using the Scherrer equation [127]. For this purpose a grain size equal to the compound phase thickness (10 nm < d_{Al_3Ni} < 75 nm) was assumed. The resulting lowest thickness of detectable Al_3Ni phase is plotted in Figure 3.28. At an acquisition time of 20 s ($f_{XRD} = 0.05$ Hz) a compound phase thickness below 2 nm can be resolved. This increases up to 9 nm for f_{frame} = 2 kHz. For the highest acquisition rate of 20 kHz, the lower limit increases significantly to a value above 23.4 nm. Therefore, for frame rates > $5 \cdot 10^3$ Hz a reduced phase resolution has to be taken into account.

3.2.3 Synchrotron data analysis

The raw XRD data was analysed using a self-developed Python script. The procedure includes: (i) radial count integration, (ii) data binning, (iii) X-ray intensity correction, (iv) background subtraction and (v) diffraction peak identification and fitting. Since a single experiment comprises between 600 and

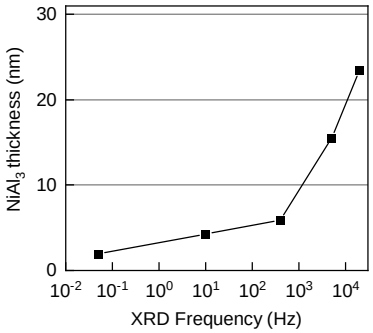

Figure 3.28: Calculated results of the lowest amount of Al_3Ni phase detectable with synchrotron XRD. For measurements with an acquisition time of 20 s (= 0.05 Hz) a Al_3Ni phase thickness less than 2 nm can be detected. At 20 kHz the deteacable Al_3Ni phase thickness is lowered to 23.4 nm.

4000 individual diffractograms, an automated routine was required. In the following, the individual steps of the analysis are described in detail.

Radial count integration

The conversion of 2D to 1D diffraction data was done by radial count integration. For this purpose, the *PyFAI* [128] based *Bubble* [129] software was used. A geometrical calibration using the diffracted signal of LaB_6 was performed prior to each beam time to take the detector position into account. Exemplarily, the azimuthal angle vs. the 2θ angle for an Al/Ni sample during a reaction is shown in Figure 3.29 (a). The white arrows indicate Al_3Ni peaks, whereas the red arrows indicate Al. Except for Pt which is excluded in the experimental analysis, the diffraction peak intensity is evenly distributed along the azimuthal angle. This is important since only the azimuthal angle range of 33° and 148° is recorded and not the complete Debye-Scherrer ring. A detailed description of the X-ray intensity correction step can be found in Appendix A.5.

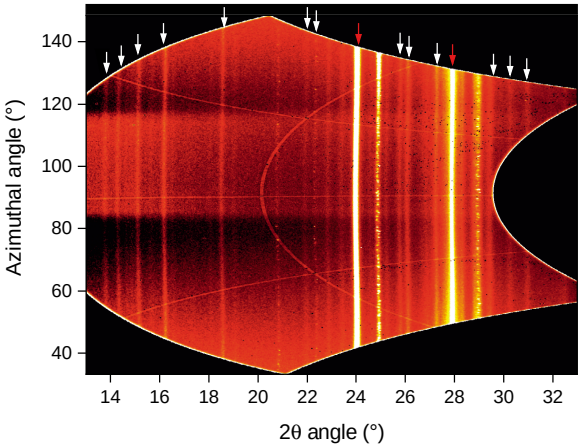

Figure 3.29: Diffracted X-ray intensity as a function of the azimuthal and the 2θ angle. The peak intensity of Al_3Ni (white arrows) and Al (red arrows) is evenly distributed over the diffraction ring.

Binning

Especially at high frame rates > 5 kHz, binning was performed to reduce the measurement noise. Although this results in a decrease in the temporal resolution, the gain in phase resolution and the reduction of computation time outweigh the disadvantages. The number of frames for binning was adjusted for each experiment in dependence on the required phase or temporal resolution.

Background removal

The diffraction peaks are superimposed by background signal caused by diffusive scattering at the nanocalorimetry sensor membrane and air. Prior to peak fitting, the background was removed. Exemplarily, this is shown in Figure 3.30 (a). The background is approximated by a 5^{th}-order polynomial function. Only diffractograms of the early stages of the reaction were taken. The background was fitted only in 2θ regions where no peaks are present.

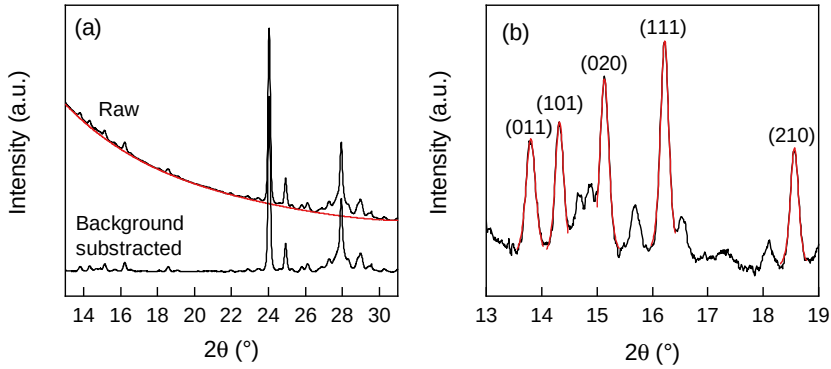

Figure 3.30: (a) The amorphous background of the diffracted signal is determined by fitting and subtraction of a 5th-order polynomial function. (b) To quantify the XRD results, peaks (in this case Al_3Ni) are fitted by using a Voigt function.

Peak fitting In a final step, peaks were fitted using a Voigt function. This allows the determination of quantities like peak position, peak broadness, peak area and peak height. These parameters are fundamental for the structural characterisation of the samples. An example of the fitting procedure is shown in Figure 3.30 (b). To avoid errors, only well-separated Al_3Ni peaks were taken.

3.3 Electron microscopy

For the microstructure characterisation of the Al/Ni multilayers, electron microscopy was used. In particular, the Al/Ni interfaces and the morphology of the precipitating intermetallic phases were the focus of the investigations. For this purpose, scanning electron microscopy (SEM) and scanning transmission electron microscopy (STEM) was used. Electron-transparent lamellas of the multilayer cross-section were prepared by SEM and focussed ion beam (FIB) technique. In detail, the standard "lift-out" technique was applied with the

FEI NanoLab (Thermo Fisher Scientific, USA). In a first step, the nanocalorimetry sensor with the Al/Ni sample on the top of the membrane was attached with conductive varnish to a FIB sample holder. The sensor was positioned so that the Pt heater was upturned. After deposition of Pt on the heating strip, a $\sim$3 µm thin lamella was cut using the Ga ion beam and the electron beam. The ion current was reduced gradually from 20 nA to 7 nA and 1 nA. The lamella was transferred to a TEM sample grid and thinned to a final thickness of 50-100 nm. A detailed description of the process can be found in *Overwijk et al.* [130] and *Giannuzzi et al.*[131]. The preparation and the microscopy were mostly performed at Laboratorium für Elekotronenmikroskopie (LEM) at the Karlsruhe Institut of Technology (KIT).

4 Results and Discussion

The first objective of this study was the development of an experimental approach to characterize rapid reactions in Al/Ni multilayers. As outlined in Chapter 3, a heating rate regime of > 10 $\mathrm{K\,s^{-1}}$ and a temporal resolution of the structural characterisation of 45.5 µs was reached by combing nanocalorimetry and synchrotron XRD. This enables us in the second part of the study to explore Al/Ni multilayer reactions under runaway conditions. Besides the identification of the phase selection mechanism, the kinetics of phase formation and the thermodynamic quantification of the ignition point are the main objectives of the study (compare Section 1.3). The findings are discussed in the context of the heating rate and the solid or liquid state of the constituents. In Section 4.1, phase formation under slow and intermediate heating rates of $10 \leq \dot{T} \leq 10^3$ $\mathrm{K\,s^{-1}}$ are investigated. In Section 4.3, the runaway reaction triggered by fast heating at $10^3 \leq \dot{T} \leq 10^6$ $\mathrm{K\,s^{-1}}$ is evaluated. The transition between the solid-state and the runaway reaction is defined by ignition, which is the main focus of Section 4.2.

4.1 Slow and intermediate heating rates: Solid-state reactions

First, the phase transformations of Al/Ni multilayers were characterized at a heating rate regime between 10 $\mathrm{K\,s^{-1}}$ and 10^3 $\mathrm{K\,s^{-1}}$. For the phase formation in Al/Ni multilayers, it is generally accepted that phase formation occurs via phase nucleation and subsequent growth [31]. In the course of this section,

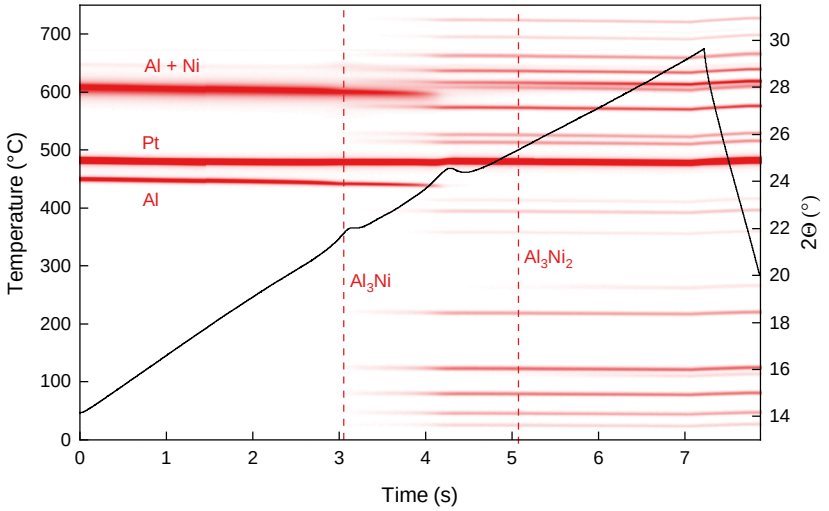

Figure 4.1: *In situ* heating of Al/Ni multilayers with 100 $\mathrm{K\,s^{-1}}$. Synchrotron X-ray diffraction (red) reveals that the two exothermic temperature peaks (black curve) are correlated with the formation of Al_3Ni.

both processes are considered separately. The influence of the heating rate and the bilayer thickness on the nucleation behaviour are studied in Section 4.1.1. Here, two questions are specifically addressed: (i) At which temperature does the new phase start to form? (ii) What type of phase is formed first? In Section 4.1.2, the subsequent growth behaviour is characterized. *In situ* X-ray diffraction is utilized to quantify the growth kinetics of the individual phases. Based on these results, a mechanism for phase formation in Al/Ni multilayers is proposed in Section 4.1.3. For a broader understanding in all investigations, the multilayer composition was varied between 5 at.% Ni and 25 at.% Ni.

In order to get a general understanding of the structural processes that take place during heating, a Al/Ni multilayer sample with 25 at.% Ni was heated at 100 $\mathrm{K\,s^{-1}}$. Nanocalorimetry was used to heat the sample linearly to a peak

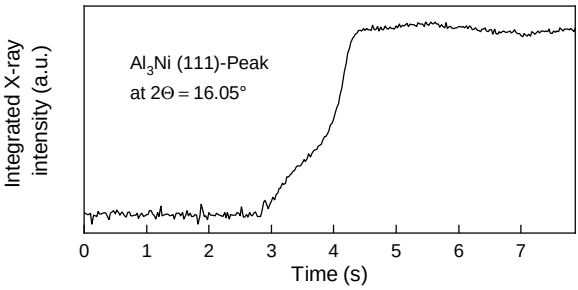

Figure 4.2: Integrated peak intensity of the Al_3Ni (111) peak shown in Figure 4.1.

temperature of 674 °C. The resulting temperature profile in combination with the time-resolved X-ray diffractograms (plotted in red) are shown in Figure 4.1. There is a linear increase of temperature with the exception of two temperature peaks at 325 °C and 430 °C. At the beginning of the experiment, four distinctive diffraction peaks are identified. The peaks can be assigned to Al ($2\theta_{Al(111)}$ = 24.15°), Pt ($2\theta_{Pt(111)}$ = 24.96° and $2\theta_{Pt(200)}$ = 28.97°) and an overlapping peak comprised of Ni and Al ($2\theta_{Al(111)+Ni(200)}$ = 28.02°). The Pt peak is caused by the sensor heating strip and is not involved in the reaction. For temperatures up to 325 °C, the diffractograms show no indications of new phases. Only a shift of the peak position is observable, which is attributed to thermally induced lattice expansion. Once the first temperature peak at 325 °C is measured with nanocalorimetry, multiple diffraction peaks are observed between 13.79° < 2θ < 30.92°. These peaks are characteristic for the Al_3Ni intermetallic phase. With further heating, the Al_3Ni peaks grow in intensity. The increase in intensity becomes even more apparent when plotting the integrated peak intensity of the Al_3Ni (111)-peak. In Figure 4.2 a second temperature peak is observed at 430 °C. This is correlated with a steep increase of the integrated intensity in Figure 4.2 at about 4 s. This phase formation behaviour indicates two separated formation stages. The characteristics of this so-called 'two-stage phase formation' process are shown in detail in

Section 2.4. Simultaneously, the intensity of the Al and Ni peak decrease significantly. Since the transition is well below the melting temperature of all constituents ($T_{m,Al}$ = 660°C and $T_{m,Ni}$ = 1455 °C), we conclude that Al and Ni is consumed to form Al_3Ni. Only well above 430 °C (second nanocalorimetry peak), new diffraction peaks at 15.81° and 19.60° are observed, which can be attributed to the Al_3Ni_2 intermetallic phase. Here, no temperature peak is detected via nanocalorimetry. The transition does not provide enough reaction power to increase the sample temperature. This could either be explained by a low exothermic heat release or low conversation rate of the reaction. At higher temperatures as well as during cooling, all peaks remain unchanged, which indicates that the reaction is completed. The example of the Al_3Ni_2 formation demonstrates the advantages of the *in situ* approach. Although the phase transition is not detectable by nanocalorimetry at this rate, synchrotron XRD allows to resolve it. Therefore, measurements below the operation heating rate of nanocalorimetry are accessible.

4.1.1 Formation of intermetallic phases

In the next step, the influence of the bilayer thickness and heating rate conditions on the phase sequence is systematically investigated. For this purpose, Al/Ni multilayers with a compositional range of 5-25 at.% Ni were tested. In case of 5-15 at.% Ni, the individual Ni layer thickness is 15 nm (Λ = 448, 220, 144 nm). In the case of 25 at.% Ni, the layer thickness is 30 nm (Λ = 166 nm). Depending on the sample composition, the heating rate was gradually increased from 10 $K s^{-1}$ up to 1000 $K s^{-1}$ to evaluate the phase transitions in the Al/Ni multilayers. In Figure 4.3, the temperature profiles of the reactions are plotted as functions of heating rate and composition. Only experiments with a solid-state reaction are shown. In case of 15 at.% Ni and 25 at.% Ni, there is a change in the reaction mode at heating rates above 500 $K s^{-1}$. Instead of a

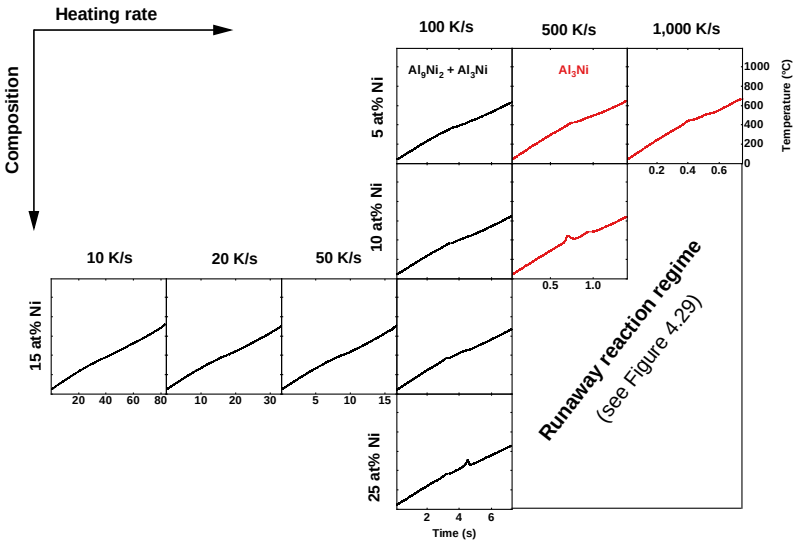

Figure 4.3: Overview of the heating experiments in the solid-state reaction regime. A heating rate regime of 10 $\mathrm{K\,s^{-1}} \leq \dot{T} \leq 10^3\ \mathrm{K\,s^{-1}}$ and 5 at.% Ni $\leq c \leq$ 25 at.% Ni was investigated. Temperature profiles plotted in black represent reactions where Al_9Ni_2 and Al_3Ni are formed. In the case of red temperature profiles only Al_3Ni was formed.

solid-state reaction, a runaway reaction with a significant temperature increase occurs. These types of reactions are covered in Section 4.3.1. Low heating rates down to 10 $\mathrm{K\,s^{-1}}$ were only investigated for the 15 at.% Ni multilayer samples. All multilayers tested show only minor temperature peaks. Hence, the ignition of the sample did not take place under these experimental conditions. At low heating rates and low Ni content, the temperature follows linear heating predefined by the nanocalorimetry sensor. Specimens with 10 at.% Ni heated with 500 $\mathrm{K\,s^{-1}}$ and 25 at.% Ni heated with 100 $\mathrm{K\,s^{-1}}$ show two subsequent peaks with alternating peak heights. The colour of the temperature profiles marks the type of the first phase. Independent of the composition up to 100 $\mathrm{K\,s^{-1}}$ the Al_9Ni_2 in combination with Al_3Ni phase (black line) is

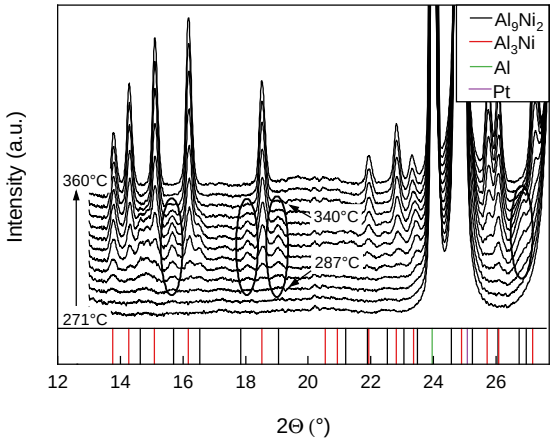

Figure 4.4: *In situ* X-ray diffractograms during heating of Al/Ni multilayers with 7.4 $\mathrm{K\,s^{-1}}$. Besides Al_3Ni, Al_9Ni_2 is formed in this heating rate regime.

formed. As discussed in detail later in the chapter, there is an almost simultaneous formation of Al_9Ni_2 and Al_3Ni. At higher heating rates, this changes to Al_3Ni (red line). In all cases, Al_9Ni_2 is not stable at elevated temperatures and decomposes while the amount of Al_3Ni increases. The heating rate regime above 100 $\mathrm{K\,s^{-1}}$ was found to be the upper limit where Al_9Ni_2 is formed. At elevated heating rates of 500 $\mathrm{K\,s^{-1}}$ and 1,000 $\mathrm{K\,s^{-1}}$, solely Al_3Ni is formed.

For a more detailed investigation of the Al_9Ni_2 phase formation process, the heating rate was reduced to targeted 10 $\mathrm{K\,s^{-1}}$. The actual heating rate was 7.4 $\mathrm{K\,s^{-1}}$ and therefore deviates slightly from the target value. Figure 4.4 plots the temporal sequence of diffractograms captured during the initial stages of the phase transition. At the given heating rate of 7.4 $\mathrm{K\,s^{-1}}$, the temperature increases about 7-8 °C per diffractogram. First evidence of phase formation is observed at 287 °C. Peaks start to form at 2θ = 13.72°, 14.83°, 15.65°, 18.05° and 19.04°. The first two peaks correlate with the Al_3Ni phase (PDF: 01-071-5885 [132]) indicated by red lines. The remaining three peaks

are in good agreement with the Al_9Ni_2 phase (PDF: 01-071-5664 [132]) indicated by black lines. With further heating to 294 °C, further peaks of Al_3Ni start to form. Initially, the intensity of both phases continuously increases with temperature. At 315 °C, this behaviour change and the peak intensity of Al_9Ni_2 starts to decrease while Al_3Ni further increases. From this temperature on, the formation of Al_3Ni starts to accelerate. Already at 340 °C, the Al_9Ni_2 peaks are no longer detectable. This reveals that at 7.4 $K\,s^{-1}$ the formation of Al_3Ni is accompanied by the Al_9Ni_2 phase. For the most part, both phases are formed in parallel. This contradicts observations in the literature where a phase sequence of Al_9Ni_2, followed by Al_3Ni is reported [14, 30, 50]. With further reaction progression, the amount of Al_3Ni continuously increases, whereas the Al_9Ni_2 is only stable in a narrow temperature regime between 287 °C and 340 °C.

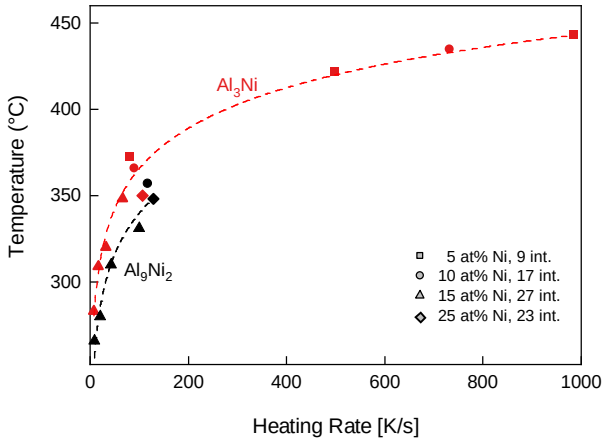

Figure 4.5: The onset temperature of the Al_9Ni_2 and Al_3Ni phase formation vs. the heating rate. The onset was determined by *in situ* XRD. For both phases, the nucleation temperature is shifted to higher values with increasing heating rate. Al_9Ni_2 formation was only observed for heating rates less than $\sim$100 $K\,s^{-1}$.

The systematic analysis of the onset of phase formation reveals that the phase formation temperature increases with heating rate. The onset of phase formation is defined as the temperature at which an X-ray diffraction peak can be clearly distinguished from the background signal. Figure 4.5 plots the temperature at which the formation of Al_9Ni_2 and Al_3Ni was first observed. For both phases, the phase formation temperature increases with the heating rate, whereas the slope of the curve decrease continuously. In case of Al_3Ni the phase formation temperature is shifted from 283 °C to 443 °C by increasing the heating rate from 10 Ks^{-1} to 1,000 Ks^{-1}. At 100 Ks^{-1}, there is scattering in the temperature data. This is attributed to different bilayer thicknesses, which result in a varying number of Al/Ni interfaces. Because interfaces are preferred locations for phase formation, a higher number of interfaces enhance the phase sensitivity of XRD. The formation temperatures for Al_9Ni_2 and Al_3Ni are almost equal. Partially, as with the heating rate of 100 Ks^{-1}, the values are overlapping. Nevertheless, the systematic analysis of all heating rates (dashed lines) suggests that Al_9Ni_2 tends to form first. However, due to the slight difference between both curves of less than 20 °C, it is questionable whether the proposed phase sequence $Al_9Ni_2 \rightarrow Al_3Ni$ is valid for all experimental conditions [14, 30, 50].

The Kissinger analysis enables the quantification of the activation energy E_a for thermally activated processes [133]. The basis for this is the shift of the reaction rate maximum (= exothermic peak) with increasing heating rate. The underlying equation is given by [133]

$$\ln\left(\frac{\dot{T}}{T_{peak}^2}\right) = \ln\left(-\frac{AR}{E_A}f'(\alpha)\right) - \frac{E_a}{RT_{peak}} \tag{4.1}$$

where T_{peak} is the temperature at the maximum reaction rate and $f'(\alpha) = df(\alpha))/d\alpha$. A detailed description of the Kissinger approach is given in

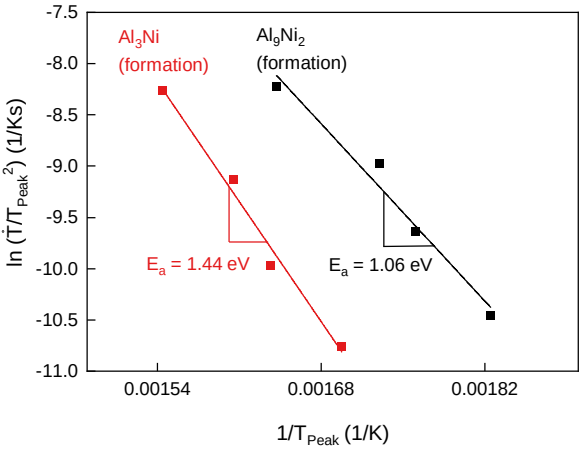

Figure 4.6: Kissinger analysis of the formation of Al_9Ni_2 and Al_3Ni. For the formation of Al_9Ni_2 a activation energy of 1.06 ± 0.12 eV is determined. In the case of Al_3Ni the activation energy is 1.44 ± 0.13 eV.

Vyazovkin et al. [73]. By plotting $ln(\dot{T}/T^2_{peak})$ as a function of $1/T_{peak}$, the activation energy can be determined by the slope of the curve. Figure 4.6 plots the Kissinger analysis of Al_9Ni_2 and Al_3Ni. As already noted, the Kissinger equation is derived under the condition of maximum reaction rate. As shown later in Figure 4.9 (b) and (d), in the cases of Al_9Ni_2 and Al_3Ni, the maximum reaction rate occurs at $\alpha = 0.2$. Therefore, based on the XRD and nanocalorimetry signal, the temperature at $\alpha = 0.2$ was derived. Since the beginning of the reaction is excluded, the different phase sensitivity at different XRD frame rates is compensated. The XRD signal is advantageous for the Kissinger analysis since overlapping processes like diffusion and phase formation can be well separated. Only multilayers with a constant number of interfaces were used for the Kissinger analysis to avoid an erroneous influence of the interface density.

Table 4.1: Activation energies in the Al/Ni system

Type	**Reference**	**Activation energy [eV]**
Interdiffusion	Schnabel [134]	1.1
	Liu [135]	0.83 - 0.95
	Grieseler [136]	1.24
	Grapes [110]	1.08
	Grapes [7]	1.17
	Joress [137]	0.35
Al_9Ni_2	Blobaum [50]	1.58
	Da Silva Bassani [68]	1.33 - 1.51
	This study	1.06 ± 0.12
Al_3Ni	Michaelsen [31]	1.47 [1] & 1.63 [2]
	Michaelsen [29]	1.64 - 1.76
	Grapes [7]	1.42
	Barmak [48]	1.26–1.54 [1]& 1.64–1.75 [2]
	Blobaum [50]	1.9
	Ma [67]	1.49[1] & 1.44[2]
	This study	1.44 ± 0.13 [1]

[1] First stage, [2] Second stage

For the nucleation of Al_3Ni, an activation energy of 1.44 ± 0.13 eV was determined. A lower value of 1.06 ± 0.12 eV was calculated for the formation of Al_9Ni_2. This suggests that the formation Al_9Ni is the thermodynamically favoured process since the energy barrier for formation is lower. In Table 4.1, the activation energies determined in this study are compared to literature values. Generally, it is found that the activation energy for Al_3Ni formation agrees well with the literature values. Deviations of E_a may be explained by the difference in the sample deposition technique. In case of Al_9Ni_2 formation, there is only a limited database available [50, 68]. However, the value determined in

this study tends to be lower than in the literature. In fact, E_a for Al_9Ni_2 formation is much closer to reported values for interdiffusion between Al and Ni. This may suggest that atomic movement defines the thermodynamic barrier for Al_9Ni_2 formation. This is discussed in detail in Section 4.1.3.

4.1.2 Phase growth in later transformation stages

After nucleation, the growth kinetics of the intermetallic phases were characterized. For this purpose Al/Ni multilayer samples with a Ni content of 10 at.% were isothermally heated at temperatures of 220 °C, 250 °C, 276 °C and 298 °C for either 300 s or 600 s. Figure 4.7 plots the extent of conversion α of the Al_9Ni_2 and Al_3Ni phase versus the normalized time $t/t_{0.5}$. To quantify the phase content, XRD was used. Under certain conditions, the integrated diffracted peak intensity is proportional to the amount of phase in the sample. To ensure a linear correlation between the integrated peak intensity and the amount of phase, several factors like the temperature dependency, X-ray absorption, incoming beam intensity are considered in Appendix A.5. A sufficient number of peaks were taken to reduce the potential influence of variations in the grain orientation. A detailed description of the implementation of the peak integration process can be found in Section 3.2.3. Finally, the resulting integrated peak intensity was used to quantify the extent of conversion:

$$\alpha = \frac{I_{XRD}}{I_{XRD,max}} \tag{4.2}$$

Here, I_{XRD} is the integrated and $I_{XRD,max}$ the maximum XRD peak intensity at a given time of the experiment.

For better comparability, the data were normalized to $t_{0.5}$. This is the point of time, where α equals 0.5 (see Appendix A.6). This facilitates the comparison of experiments with different temperatures and durations. As outlined in

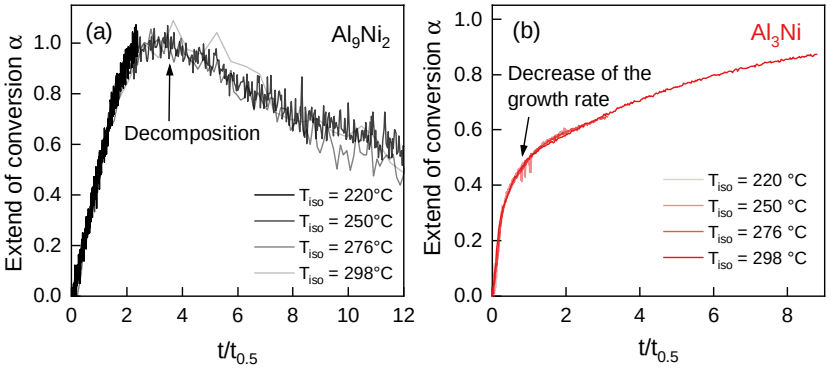

Figure 4.7: Phase growth under isothermal heating rate conditions. The relative amount of phase α is plotted versus the normalized time $t/t_{0.5}$. (a) The amount of Ni_9Ni_2 shows a temporary maximum, followed by a decrease of the amount of phase. (b) The amount of Al_3Ni continuously increase and approaches asymptotically a value of 1.

Section 2.4.4, the benefit of isothermal heating is that the kinetic curve is only given by the reaction model $f(\alpha)$ [73]. Hence in Figure 4.7, the growth kinetics of a phase can be directly determined from the α curve. Independent of the annealing temperature, all curves coincide, which proves the reproducibility of the method. Higher scattering in the Al_9Ni_2 signal can be attributed to the significantly lower peak intensities. The growth behaviour of Al_9Ni_2 and Al_3Ni differ significantly. In case of Al_9Ni_2, there is a rapid linear increase of α to the maximum at $t/t_{0.5} = 3$. With further annealing, the amount of Al_9Ni_2 decreases again until a value of $\alpha = 0.6$ at $t/t_{0.5} = 12$ is reached at the end of the experiment. In contrast, Al_3Ni has the highest growth rate at the beginning of the reaction. The amount of phase increases continuously, whereas the growth rate decreases. At $\alpha = 0.5$, a transitional regime with a significant drop in the slope of the curve is observed. The sample was not completely converted into Al_3Ni within this experiment. To determine the phase amount of completely converted sample and the corresponding $I_{XRD,max}$, the same type

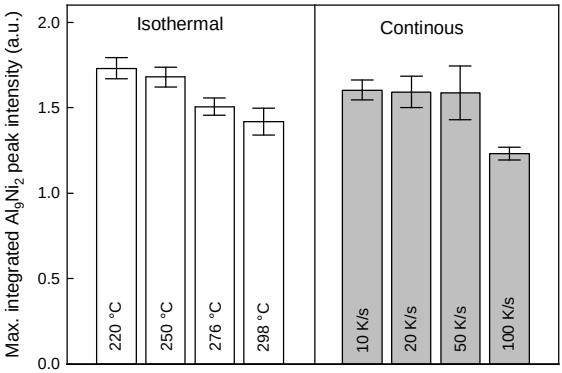

Figure 4.8: The maximum integrated Al_9Ni_2 peak intensity per interface under isothermal and continuous heating conditions. Independent of the heating rate conditions, an almost constant amount of maximum phase was observed. The standard deviation takes the scattering of the XRD signal at the maximum value into account.

of sample (bilayer thickness, total film thickness) was investigated after a runaway reaction. In the course of a runaway reaction, the temperature exceeds the melting temperature of Al. In the liquid phase, ideal intermixing between the reactants can occur. Therefore the complete sample is converted into its product phase. The validity of $I_{XRD,max}$ at $\alpha = 1$ is proven by the congruence between the individual curves recorded at different temperatures.

In order to draw conclusions about the underlying Al_9Ni_2 growth mechanism, the maximum amount of phase is evaluated. The maximum of the integrated peak intensity of the Al_9Ni_2 phase under isothermal and continuous heating rate conditions is plotted in Figure 4.8. As previously stated, the integrated peak intensity is proportional to the maximum amount of phase. In the case of isothermal heating, the Ni content of the samples is 10 at.%, whereas for continuous heating samples with 15 at.% Ni was used. To compensate for this,

the plot is normalized to the number of Al/Ni interfaces. It is found that in the isothermal case, the maximum amount of Al_9Ni_2 tends to decrease slightly with temperature. However, the decrease hardly exceeds the standard deviations of the measurement. To prove whether the maximum amount of Al_9Ni_2 is dependent on the heating conditions, samples were heated continuously at a rate of 10, 20, 50 and 100 $\mathrm{K\,s^{-1}}$. It was found that the heating conditions have no significant impact on the amount of Al_9Ni_2 phase formed. Only for 100 $\mathrm{K\,s^{-1}}$, the amount of Al_9Ni_2 is reduced, which may be interpreted as an incomplete conversion.

To get a more detailed understanding of the phase growth behaviour, growth kinetics were analysed. The objective is a description of the Al_9Ni_2 and Al_3Ni growth with a suitable kinetic model. As outlined in Section 2.4.4, the conversion rate of thermally activated processes is given by

$$\frac{d\alpha}{dt} = k(T)f(\alpha) \tag{4.3}$$

The first temperature-dependent term $k(T)$ is characterized by the activation energy determined by the Kissinger analysis in Figure 4.6. The second term $f(\alpha)$ represents the conversion-dependent kinetic model. The underlying physical mechanism can be inferred by assigning a valid reaction model to the phase formation data. Complementary to the isothermal data, continuous heating data with a heating rate of 10 - 100$\mathrm{K\,s^{-1}}$ is used for this analysis. According to the *International Confederation for Thermal Analysis and Calorimetry (ICTAC)* [73], the reliability of a kinetic model is significantly enhanced if the model is able to describe the phase formation kinetics under arbitrary heating conditions (isothermal and continuous heating).

The results of the kinetics analysis are summarized in master plots. Master plots allow for the comparison of kinetic data from isothermal and continuous

heating rate conditions [138]. In the first master plot in Figure 4.9 (a) and (c), the normalized conversion $g(\alpha)/g(0.5)$ is plotted versus α. The normalized conversion is the integral form of $f(\alpha)$ and defined as

$$g(\alpha) \equiv \int_0^{\alpha} \frac{d\alpha}{f(\alpha)} \tag{4.4}$$

In the differential form, the normalized growth rate $f(\alpha)/f(0.5)$ is plotted versus α in Figure 4.9 (b) and (d). In both cases, Al_9Ni_2 and Al_3Ni is considered separately. In Appendix A.6 the mathematical principle of master plots is described. In addition, calculated traces (solid black lines) of selected kinetic models from Table 4.1 are plotted for reference. Besides this, the schematic of the growth behaviour of the models is shown in Figure 4.9. To reduce noise in the data, the number of data points was reduced to 10-15 points by a moving average procedure. It should be noted that scattering in the continuous heating data did not allow for a sufficient analysis of $f(\alpha)/f(0.5)$. Therefore only isothermal heating data was used in this case.

Al_9Ni_2 growth

The growth kinetics of Al_9Ni_2 is evaluated first. The integral kinetic data $g(\alpha)/g(0.5)$ of Al_9Ni_2 is shown in Figure 4.9 (a). In general, the continuous heating data (black rectangles) and the isothermal heating data (black triangles) are in good agreement. Therefore, the heating rate regime investigated can be described with an uniform kinetic model [73]. The underlying mechanisms of phase formation do not change when the heating conditions are changed. Up to $\alpha = 0.6$, there is a linear increase of $g(\alpha)/g(0.5)$. At later stages, the curve deviates from the linear behaviour and the slope of $g(\alpha)/g(0.5)$ increases. Complementarily, the differential form of the Al_9Ni_2 kinetic data is shown in Figure 4.9 (b). The $f(\alpha)/f(0.5)$ signal remains constant up to $\alpha \leq 0.6$, which is equivalent to a constant growth rate. In this regime, Al_9Ni_2 is formed

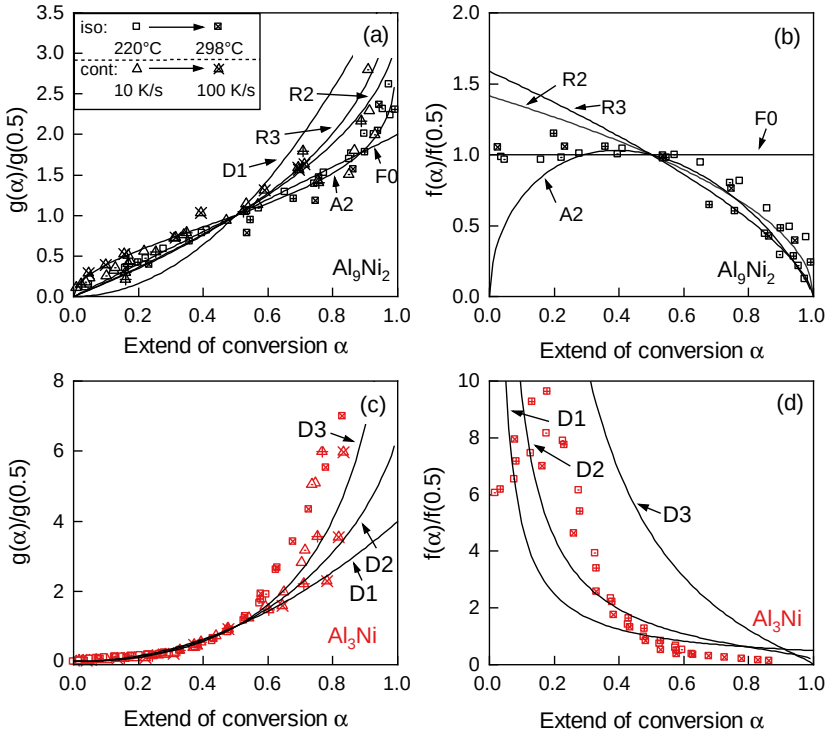

Figure 4.9: Master plots of the phase growth kinetics of Al_9Ni_2 and Al_3Ni. (a) The integral kinetic data of Al_9Ni_2 growth and (b) the corresponding differential kinetic data suggest a combination of a zero-order reaction model (F0) with a reaction model of a contracting volume (R2 and R3). In the case of Al_3Ni, the integral data (c) and differential data (d) show a good agreement with diffusion-based kinetic models (R1, R2 and R3).

at a constant rate. In the following the growth rate decrease continuously at $0.6 < \alpha < 1$ and approaches 0 when the conversion is completed.

For the identification of the phase formation mechanism, selected reaction models are plotted in black curves. Not a single reaction model was able to fit the whole α regime. For $\alpha \leq 0.6$, a zero-order reaction model (F0) is the best fit to the data, especially for the $f(\alpha)/f(0.5)$ signal. The F0 reaction model implies that the reaction rate is independent of the product phase concentration (= constant rate). In contrast, in geometry- and diffusion-based models, the diffusion length would change during the reaction and the reaction rate would be lowered. This is not the case for the first part of the Al_9Ni_2 transition. We conclude that a premixed solid solution is the starting point for a polymorphic transition into Al_9Ni_2 since, in this case, the constant diffusion length would lead to a constant reaction rate. For $\alpha > 0.6$, multiple models achieved good agreement with the measured data. Especially, reaction models of either a contracting sphere (R3), contracting cylinder (R2) or the nucleation and growth-based Avrami-Erofeev model (A2) could reproduce the data best. However, the available data do not allow the assignment of an explicit reaction model. The good agreement with R3 and R2 suggests that the remaining interspaces of premixed solid solution are transformed into the Al_9Ni_2 phase. Since the amount of premixed solid solution decrease, the reaction rate slows down. Generally, diffusion-based kinetic models showed poor correlation with the experimental data.

Al_3Ni growth

The integral kinetic data of Al_3Ni is shown in Figure 4.9 (c). Again, isothermal and continuous heating data show good agreement, which implies a single reaction model independent of the heating conditions. There is a continuous increase of $g(\alpha)/g(0.5)$ with α. The corresponding $f(\alpha)/f(0.5)$ signal shown in Figure 4.9 (d) reveals two regimes: Between $0.1 \leq \alpha \leq 0.25$,

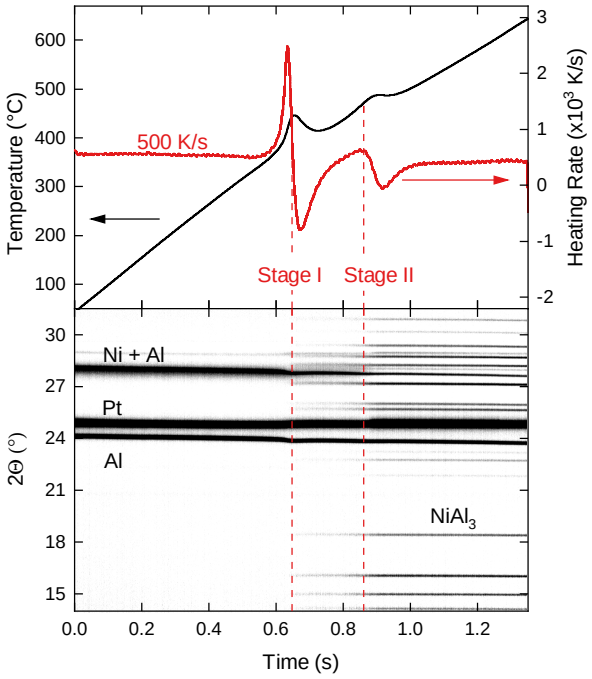

Figure 4.10: Two-stage formation of Al_3Ni in the case of an Al/Ni multilayer (10 at.% Ni) sample heated with 500 $K\,s^{-1}$. Upper part: Nanocalorimetry reveals two separated temperature peaks at 381°C and 431 °C. Lower part: The time-resolved XRD data corroborates the growth of Al_3Ni into two-stages. [126]

the $f(\alpha)/f(0.5)$ signal is at a high level. The initial increase at $\alpha < 0.1$ is not considered in the analysis since the usage of kinetic data at $\alpha < 0.1$ is generally not recommended by the ICTAC [73]. Moreover, peak fitting at the very beginning of the reaction is susceptible to errors. The second regime, starting at $\alpha > 0.25$, is characterised by a significant drop of the normalized growth rate. There is a continuous decrease of the growth rate until the reaction is completed.

The phase formation of Al_3Ni can be subdivided into two regimes. In order to reach the high growth rates in the first regime $\alpha \leq 0.25$, short diffusion pathways are required. The only region in the interface where the diffusion pathways are short, is the interface between Al and Ni. This suggests that the first regime is interface controlled. Characteristic for the second regime at $\alpha > 0.25$ is the decelerating growth behaviour. Various kinetic models were tested. Diffusion-based reaction models show the best fit to the given data set. The expected traces for 1D, 2D and 3D diffusion-limited kinetic models were calculated and plotted in Figure 4.9 (c) and (d). There is a decent congruence of the selected kinetic models with the given kinetic data. However, the 3D diffusion model seems to be the best fit for the integral data. In case of the differential data, the 2D diffusion represents the $f(\alpha)/f(0.5)$ signal more accurate. Independent of the direction, it is a valid assumption that diffusion is the controlling mechanism in the second regime. With the increasing amount of Al_3Ni, diffusion is getting more difficult, which result in a decrease in the reaction rate.

The two growth regimes of Al_3Ni become even more evident when the heating rate is increased to 500 $\mathrm{K\,s^{-1}}$. Figure 4.10 plots the temperature (black) and heating rate signal (red) of a 10 at.% Ni multilayer sample. The corresponding time-resolved X-ray diffractograms are shown in the lower part of Figure 4.10. These experimental data are published in [126]. The temperature and the heating rate signal reveal the presence of two distinctive peaks with an onset at 381°C and 431 °C. During the first peak, Al_3Ni is formed while simultaneously, the Al + Ni peak ($2\Theta_{Al(111),Ni(200)}$ = 27.95°) and the Al peak ($2\Theta_{Al(111)}$ = 24.11 °) intensity decrease. Associated with the second exothermic temperature peak, the XRD intensity of Al_3Ni significantly grows. Hence, the two exothermic peaks measured by nanocalorimetry are related to the growth of only one intermetallic compound, namely Al_3Ni.

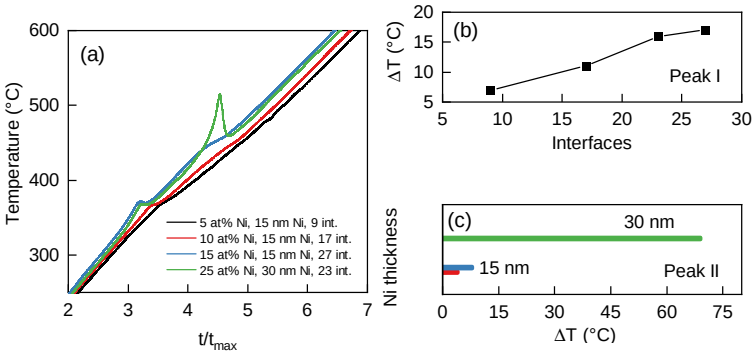

Figure 4.11: The temperature signal of Al/Ni multilayer samples heated with 100 $K s^{-1}$. (a) Depending on the bilayer thickness, the intensity of the first peak and second peak change. (b) An increase of the first peak with increasing Al/Ni interface density was observed. (c) The second peak scales with the thickness of the Ni layer.

Literature data suggest that the exothermic heat release of the two formation stages depends on the bilayer thickness [27, 70]. To prove, if this applies to given Al/Ni samples in this study, the number of interfaces and the bilayer thickness was systematically varied. Figure 4.11 (a) plots the temperature vs. the normalized time t/t_{max} for different multilayer geometries. The temperature increase of the first peak scales with the number of interfaces. Like shown in Figure 4.11 (b) ΔT increase from 7 °C to 17 °C when the number of Al/Ni interfaces is increased from 9 to 27. The investigation of the second temperature peak reveals a dependency on the Ni layer thickness. Figure 4.11 (c) plots the corresponding temperature increase for multilayers with 15 nm and 30 nm Ni. In the case of 15 nm Ni, only shallow second peaks are observable. This indicates that the Ni layers with a thickness of 15 nm are fully consumed during the first reaction stage. In contrast, the 30 nm Ni layer in case of 25 at.% Ni leading to a temperature increase of 69 °C. Therefore Ni is still remaining for the second reaction stage after the first interfacial reaction.

4.1.3 Phase formation and growth mechanisms

Based on the results of Section 4.1.1 and Section 4.1.2, a mechanism for the solid-state phase transition in Al/Ni multilayers is derived. The results suggest a heating rate dependency of the solid-state phase formation mechanism. For heating rates below 100 $\mathrm{K\,s^{-1}}$, the Al_9Ni_2 phase is formed prior to the Al_3Ni phase:

$$Al + Ni \rightarrow Al_9Ni_2 \rightarrow Al_3Ni + Al_9Ni_2 \rightarrow Al_3Ni \rightarrow Al_3Ni + Al_3Ni_2 \tag{4.5}$$

When the heating rate is increased above 100 $\mathrm{K\,s^{-1}}$, the formation of Al_9Ni_2 is suppressed and the Al_3Ni is directly formed:

$$Al + Ni \rightarrow Al_3Ni \rightarrow Al_3Ni + Al_3Ni_2 \tag{4.6}$$

A schematic illustration of both mechanisms is shown in Figure 4.12. The proposed mechanisms are valid for the full range of bilayer thickness and compositions investigated in this study. However, it should be noted that for a very thin bilayer thickness [31] or electron-beam deposited samples [28, 30], the mechanism may deviate. The main steps of the mechanisms can be summarized as follows:

As-deposited

In both cases, the starting point is a multilayer stack comprised of Al and Ni. A typical microstructure of the as-deposited state is depicted in Figure 3.22. Although the microscopical resolution impedes a detailed investigation of the Al/Ni interface, multiple studies suggest the presence of intermixing layer with a thickness of 1-3 nm [8, 9, 19, 139]. The X-ray diffraction results in Figure 4.1

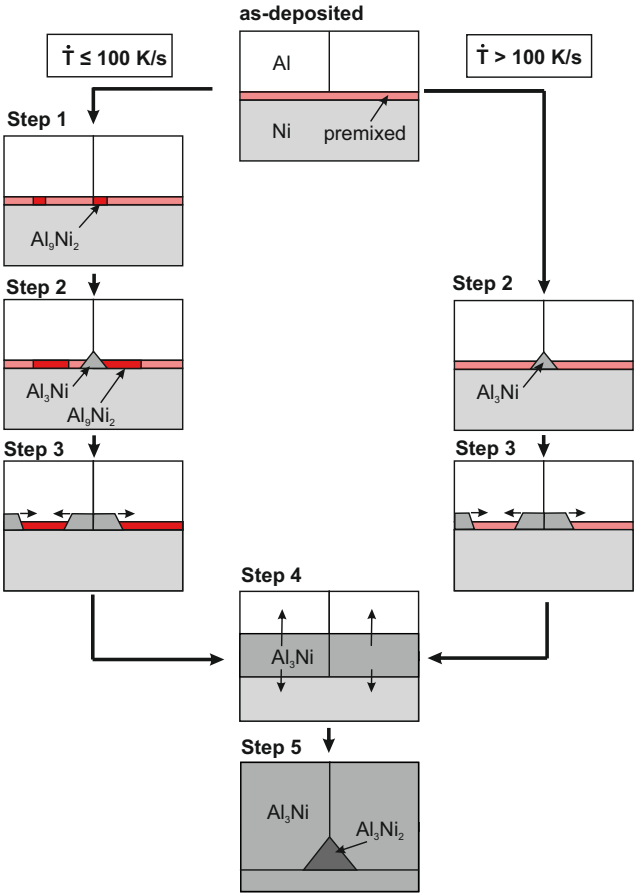

Figure 4.12: Schematic illustration of the phase formation mechanism in the solid-state. In dependence of the heating rate ($\dot{T}_{crit}$ = 100 K s^{-1}) two mechanisms were identified.

give no indications for crystalline phases besides Al and Ni in the as-deposited state. Therefore, we conclude that the intermixed layer is either amorphous or a solid solution, which is also proposed by [48].

Al_9Ni_2 formation and growth

When the multilayers are heated at rates below 100 $K\,s^{-1}$, Al_9Ni_2 is the first phase which is formed (compare Figure 4.5). The observed phase sequence is in good agreement calorimetric studies in the literature [8, 14, 30, 48, 75, 140]. However, only a slight temperature difference of 10-20 °C was observed between the nucleation of Al_9Ni_2 and Al_3Ni (see Figure 4.5). In some experiments we even observed a simultaneous nucleation of both phases. Both phases grow in parallel (see Figure 4.4). This observation is contradictory to that of *Blobaum et al.* [50], where a clear phase formation sequence is reported. From a purely thermodynamic point of view, they concluded that the Al_9Ni_2 phase is not necessarily favoured. Comparing the heat of formation of Al_3Ni + 3 Al formation ($\Delta H_{f,Al_{3Ni}}$ = -27.2 $kJ\,mol^{-1}$atom) to Al_9Ni_2 formation (ΔH_f = -28 $kJ\,mol^{-1}$atom), it becomes evident that there are only minor differences between both phases [50]. Considering the effective heat of formation at the lowest eutectic at 3.5 at.% Ni (compare Section 2.4.5) a comparable result emerges. Using equation 2.23, in case of Al_3Ni,$\Delta H_f^{'}$ is - 5.3 $kJ\,mol^{-1}$atom. In case of Al_9Ni_2, a value for $\Delta H_f^{'}$ of - 5.4 $kJ\,mol^{-1}$atom is calculated. In both considerations, Al_9Ni_2 is slightly favoured but the difference is negligible. The situation is the same when the composition gradient theory outlined in Section 2.4.1 is applied to Al_9Ni_2 and Al_3Ni. Steep concentration gradients may suppress one type of phase or favour another type. The critical thickness of the intermixed layer (= width of the concentration gradient) calculated by *Blobaum et al.* [50] is 13.8 nm in case of Al_9Ni_2 and 14.8 nm in case of Al_3Ni. Again, nucleation of Al_9Ni_2 is favoured, but there are only minor differences. Another factor which may facilitate Al_9Ni_2 nucleation, is a orientation relationship between Al_9Ni_2 and the adjacent Al phase [30, 47]. If the crystal

lattice of Al_9Ni_2 and Al are related to each other, the interfacial energy would be lowered. According to equation 2.6, the energy barrier for nucleation of Al_9Ni_2 would be lower. In summary, the results of these theoretical considerations perfectly reflect the observations in this study: the formation of Al_9Ni_2 is preferred, but there are only minor differences to Al_3Ni. Especially when real sample conditions are considered, this difference explains the parallel growth of both phases. Therefore, we conclude that the formation of Al_9Ni_2 is generally favoured, but in real samples conditions, local differences at the interface may affect the nucleation behaviour. The conditions for nucleation of both phases, Al_9Ni_2 and Al_3Ni, may be fulfilled simultaneously, which leads to a parallel growth of both phases.

The nanocalorimetry experiments shown in Figure 4.3 reveals a upper heating rate limit of 100 $K\,s^{-1}$ for Al_9Ni_2 formation. This finding extends the stability range of Al_9Ni_2 significantly, since until now the existence of Al_9Ni_2 was only proven up to 0.8 $K\,s^{-1}$ [30]. This sheds new light on the role of Al_9Ni_2 formation for intermediate or even high heating rate reactions. Although there are indications that the maximum amount of Al_9Ni_2 decreases with heating rate (see Figure 4.8), Al_9Ni_2 may be formed at even higher rates. Here, the lower phase resolution (compare Figure 3.26) at high XRD frame rates makes the identification at heating rates above 100 $K\,s^{-1}$ difficult.

There is no conclusive explanation available for an upper heating rate limit of the Al_9Ni_2 formation. Most likely, a combined effect of nucleation in a composition gradient and the complex crystal structure results in an upper heating rate limit. For the heating rate induced change of the first phase from Al_3Ni to Al_3Ni_2, a change from transversal to polymorphic nucleation in the composition gradient was proposed [11]. The time for chemical redistribution in the case of fast heating may not be sufficient for transversal nucleation. Therefore, polymorphic nucleation may suppress the more Al-rich Al_9Ni_2 phase. Additionally, we take the crystal structure into account. In Table 4.2, the crystal

structure of Al_9Ni_2 is compared to Al_3Ni. The Al_9Ni_2 phase crystallizes in a monoclinic unit cell consisting of 22 atoms. In contrast, Al_3Ni crystallizes in an orthorhombic unit cell consisting of 16 atoms. It is reasonable to assume that for the more complex crystal structure of Al_9Ni_2, the redistribution process is more difficult. In consequence, the formation of Al_9Ni_2 is suppressed at high heating rates.

Table 4.2: Crystal structure parameters of Al_9Ni_2 [30, 141, 142] and Al_3Ni [143]

	Al_9Ni_2	**Al_3Ni**
Crystal system	monoclinic	orthorhombic
Structure type	Al9Co2	In3Ir
Space group	P 1 21/a 1	Pnma
a	6.23 Å	6.60 Å
b	6.18 Å	7.35 Å
c	8.68 Å	4.80 Å
α angle	96.5°	90°
Atoms per unit cell	22	16

As shown in Figure 4.8, the maximum amount of Al_9Ni_2 per interface is almost constant, independent of the heating rate conditions. Moreover, a constant amount of Al_9Ni_2 is also reported for different multilayer geometries [30]. We interpret this finding as follows: a constant volume fraction of the microstructure is transformed into Al_9Ni_2 nearly independent of heating rate and annealing temperature. Perhaps intermixing between Al and Ni during sputter deposition creates the precondition for Al_9Ni_2 formation [28]. If Al_9Ni_2 would be formed by nucleation and growth at a sharp Al/Ni interface, the temperature dependency of diffusion (compare Section 2.4.2) would affect the amount of Al_9Ni_2 formed, especially in the case of isothermal heating. At higher temperatures, the increased atomic mobility would result in higher amounts of

Al_9Ni_2, which is not observed in this study. Based on this argumentation, we deduce that the premixed layer, which is formed during sputter deposition, is transformed into Al_9Ni_2. Less chemical redistribution is necessary to reach the composition of the nucleus. Short-range displacements of Ni and Al atoms would be sufficient to reach the local composition of Al_9Ni_2 [30]. This is supported by the low activation energy we found for Al_9Ni_2 formation (see Figure 4.6). Like summarized in Table 4.1, E_a is close to the literature values for interdiffusion between Ni and Al. Therefore, interdiffusion is the thermodynamic barrier that has to be overcome for Al_9Ni_2 formation.

It was found that the majority of the Al_9Ni_2 phase is formed at a constant rate (see Figure 4.9 (a) and (b)). Therefore, the reaction rate is independent of the volume fraction of the product phase. According to equation 2.21, there is only a dependency on the temperature. This is unexpected for a solid-state reaction since the characteristic diffusion length generally changes with reaction progression and leads to a decelerating reaction profile. Consequently, we conclude that long-range diffusion is less important for Al_9Ni_2 formation. Based on the zero-order reaction model, short-range displacements of Ni and Al atoms in the intermixed region is more likely. With further reaction progression, the reaction rate of Al_9Ni_2 decreases (see Figure 4.9). One explanation is the consumption of the premixed layer. Furthermore, it should be noted that at this stage, Al_3Ni already starts to form and Al_9Ni_2 layer gets gradually transformed into Al_3Ni. Consequently, the reaction rate is a result of two superimposed processes: (i) Transition of the intermixed layer into Al_9Ni_2 phase and (ii) the transition of Al_3Ni into Al_9Ni_2. Since the absolute amount of the phases cannot be determined in this study, the contribution of both effects is not clear and deserve further investigations.

Al_3Ni formation and growth

With further heating, interdiffusion between Al and Ni proceeds and the Al_3Ni phase starts to nucleate. In case of $\dot{T} > 100\ \mathrm{K\,s^{-1}}$, the Al_3Ni is the first phase which is formed. This finding is in good agreement with nanocalorimetry studies at heating rates above 1,000 $\mathrm{K\,s^{-1}}$ [7]. The physics of nucleation outlined in Section 2.4.1 suggests that triple junctions are preferred places for Al_3Ni formation. Here, the required interfacial energy for nucleation is reduced. The preference for triple junctions still can be seen in the late stages of phase formation. Figure 4.13 shows the microstructure (STEM) of Al/Ni multilayers annealed at 317 °C for 600 s. The tetrahedral shape of the Al_3Ni grains at the Al–Al grain boundaries prove that nucleation in triple junctions is preferred. Since grain boundaries are fast pathways for Ni diffusion, the composition gradient is lowered. According to Section 2.4.1 this favours the nucleation of intermetallic compounds like Al_3Ni. The activation energy for Al_3Ni formation was found to be higher compared to Al_9Ni_2 (see Figure 4.6). This points to long diffusion pathways of Ni atoms or the presence of a diffusion barrier, like Al_9Ni_2 grains.

As shown in Figure 4.11 (a), phase formation leads to two exothermic temperature peaks, which are correlated with the Al_3Ni. The formation of the product phase in metallic multilayer in two separated stages was firstly discovered by *Coffey et al.* [70]. For Al/Ni multilayers, this phenomenon was first documented by *Ma et al.* [27, 67]. The first growth step of Al_3Ni is attributed to interfacial growth along the Al/Ni interfaces. Regarding the phase formation kinetics shown in Figure 4.9 (d) the reaction rate remains constant up to $\alpha = 0.3$. At this early stage of the reaction, Al_3Ni is nucleating at preferred sites at the interface. However, it can be expected that the interface is not fully covered by the reactant. Therefore, with regard to Section 2.4.3, the growth of Al_3Ni can be described with the thin-product-layer case of equation 2.18. Here, the growth rate is governed by the interfacial reaction rate κ_{Al_3Ni} and therefore

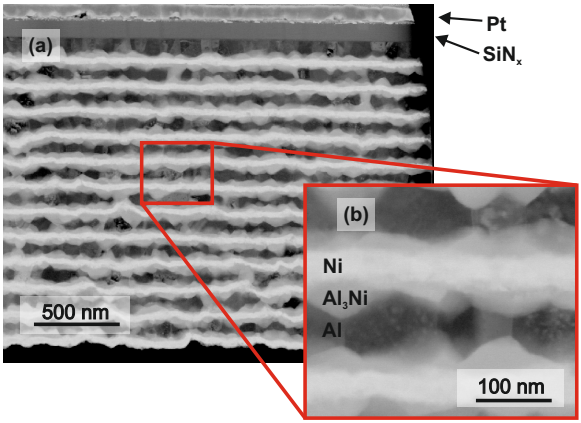

Figure 4.13: Cross-section (STEM) of an Al/Ni multilayer sample which was isothermally annealed at 317 °C for 600 s. The bright layers represent Ni and the dark layers Al. The formation of a continuous layer of Al_3Ni can be observed at the Al/Ni interface.

controlled by the processes at the interface. The result is a growth rate that is initially proportional to the time, or reference to the extent of conversion, proportional to α. For $\dot{T} \leq 100\ \mathrm{K\,s^{-1}}$, the remaining Al_9Ni_2 is consumed in course of the Al_3Ni growth (see Figure 4.4). The first reaction stage is finished when the nuclei impinge and a 2-dimensional Al_3Ni layer is formed at the interface [70]. Since nucleation within the first reaction stage takes place at the interfaces, the exothermic heat release is governed by the interfacial density in the sample. As shown in Figure 4.11 (b), the temperature increase of the first peak can be tailored by the multilayer geometry.

It was found that the amount of Al_3Ni increases significantly with the second exothermic temperature peak (see Figure 4.10). According to the two-stage

phase formation mechanism, this can be interpreted as phase growth perpendicular to the interface [70]. For this growth step, the thickening of the continuous product phase layer at the interface is characteristic. This has a direct impact on the reaction kinetics shown in Figure 4.9 (d). At $\alpha > 0.3$, the reaction rate decreases with the further extent of the conversion. The continuous Al_3Ni layer at the interface acts as a diffusion barrier for Al and Ni atoms. Regarding equation 2.19, the thickening rate of the product phase is now governed by the diffusion constant of Al_3Ni. As a result, the thickness of the product is proportional to $t^{1/2}$ or, equivalently, $\alpha^{1/2}$. Therefore, this second growth stage is a diffusion-controlled process [67]. Depending on the sample composition and the Ni layer thickness, the thickening of the Al_3Ni leads to a second temperature peak [27]. As shown in Figure 4.11 (c), the temperature increase might be low when the available Ni is completely consumed in the first reaction stage.

Al_3Ni_2 formation and growth

With further heating, Ni-rich intermetallic compounds like Al_3Ni_2 are formed (see Figure 4.1). The formation of Ni-rich compounds with further reaction progression was observed multiple times in literature [14, 16, 17, 75]. This is in good agreement with the phase sequence proposed by *Pretorius* [74]. Like outlined in Section 2.4.5, diffusion of Ni into Al_3Ni proceeds. The next stable phase leading to the most negative value of the effective heat of formation is the Al_3Ni_2 phase, which is formed at the Ni/Al_3Ni interface.

4.2 Ignition

When reactive materials are heated at a sufficiently high rate, ignition takes place and the solid-state reaction discussed in the previous section turns into a runaway reaction. Ignition of reactive materials is predominantly defined by the energy release rate. Therefore in Section 4.2.1 the energy release rate denoted as reaction power is quantified depending on various parameters like the material geometry, heating rate and heat capacity. Based on these results, in Section 4.2.2 a new criterion for ignition is derived and sample effects and effects from the reaction conditions (heat losses to the surrounding) on the ignition temperature are discussed.

4.2.1 Exothermic heat release

The reaction power of Al/Ni multilayers is characterized at heating rates above 1,000 $\mathrm{K\,s^{-1}}$ by using nanocalorimetry. A detailed description of the method can be found in Section 3.1.3. The exothermic heat release is quantified by the reaction power $\dot{Q}_{rct}$ and the reaction enthalpy change per temperature dH/dT. The latter one allows a direct comparison of the energy release of experiments with different heating rates. dH/dT is defined by

$$\frac{dH}{dT} = \frac{\dot{Q}_{rct}}{\dot{T}} \tag{4.7}$$

By normalizing dH/dT by the number of interfaces, a quantity is available, which allows for the comparison of the heating-rate-independent energy release per interface.

First, the influence of the interface density on the heat release is investigated. Figure 4.14 (a) shows $\dot{Q}_{rct}$ as a function of temperature. Al/Ni multilayers with

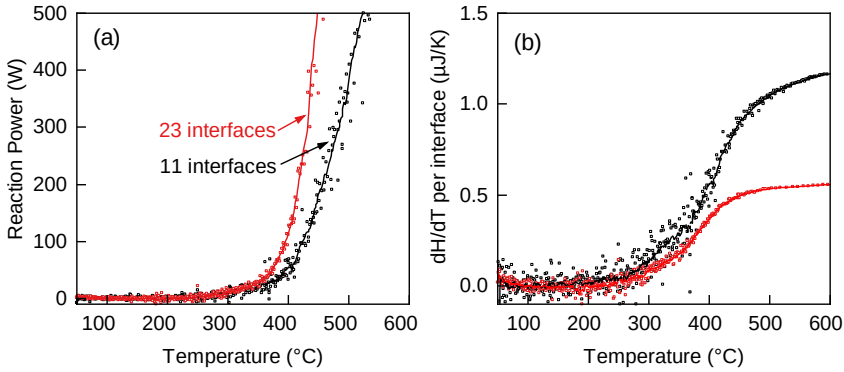

Figure 4.14: Influence of the interface density on the reaction power $\dot{Q}_{rct}$. (a) Starting at 270 °C, $\dot{Q}_{rct}$ increases with temperature. $\dot{Q}_{rct}$ is shifted to lower temperatures when the number of interfaces is increased. (b) The enthalpy change per temperature and interface proves that in the initial stage of the reaction, the same amount of energy is released for each interface.

a composition of 25 at.% Ni and overall thickness of 1 µm were tested. By reducing the bilayer thickness from 166 nm to 83 nm, the number of interfaces was increased from 11 (black line) to 23 (red line). For better visualization, the data points were smoothed by a moving average method (solid line). It was found that for both samples, $\dot{Q}_{rct}$ increases rapidly with temperature. However, in case of 23 interfaces, the rise of $\dot{Q}_{rct}$ is shifted to lower temperatures and the curve is steeper compared to 11 interfaces. The comparison of dH/dT per interface shown in Figure 4.17 (b) reveals, that the energy release for both samples starts at 270 °C. Up to 400 °C, both specimen show a almost identical increase of dH/dT per interface. This proves that at the initial stage of the reaction, the energy release is solely dependent on the interface density in the multilayer stack. At each interface, the same amount of energy is released. Therefore, in the beginning, the overall $\dot{Q}_{rct}$ of the specimen scales linearly with the number of interfaces. At temperatures above 400 °C, the dH/dT

signal is flattened for both specimens. Nevertheless, dH/dT proceeds at a significantly higher level in the case of 11 interfaces. In other words, the amount of energy that is released per interface is higher for a lower interface density. This is not intuitive since the overall composition of the sample is the same. Since all samples were deposited under the same conditions, differences in the interfacial structure are not expected. However, it is well known that the interface density has a direct impact on the reaction rate [9].

In order to prove if the reaction rate directly impacts dH/dT per interface, an experiment was designed where the same Al/Ni multilayer reaction takes place at different rates. This was realized by keeping the multilayer dimensions (total thickness and bilayer thickness) constant while varying the membrane thickness of the nanocalorimetry sensor between 150 nm and 1500 nm. By increasing the membrane thickness of the sensor, the heat capacity C_P of the non-reacting components is increased. Figure 3.20 proves the linear correlation between membrane thickness and C_P. The additional C_P decelerates the Al/Ni reaction. The resulting heating rate of the reaction for sensor different membrane thicknesses is shown in Figure 4.15 (a). When the membrane thickness is increased, the heating rate during reaction decreases from about $5.1 \cdot 10^5$ $\mathrm{K\,s^{-1}}$ for 150 nm to $5.4 \cdot 10^4$ $\mathrm{K\,s^{-1}}$ in case of 1500 nm. In this way, the influence of the heating rate on the heat release can be investigated without changing the sample dimension or composition. It should be noted that Ni with 7 at% V instead of pure Ni was used for this experiment. Since only the correlation between heating rate and dH/dT is of interest, the material selection does not impact the experiment.

The resulting dH/dT curve as a function of the temperature is shown in Figure 4.15 (b). Up to 400 °C, the heat release per interface is equivalent for all experiments. Within this initial regime, there is no significant increase of the heating rate observed (see Figure 4.15 (a)). At higher temperatures, dH/dT per interface proceeds at an almost constant level. We find higher values for dH/dT

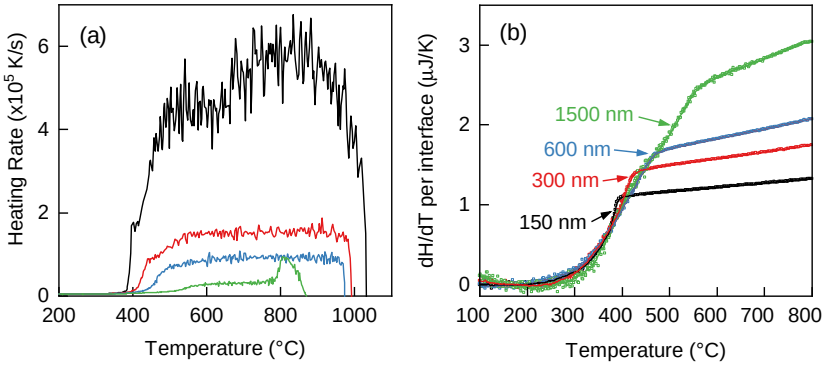

Figure 4.15: (a) Heating rate signal of an Al/Ni(7at.% V) reaction as a function of the nanocalorimetry membrane thickness. (b) The enthalpy change per temperature and interface increase with decreasing heating rate.

per interface when the reaction proceeds at a lower rate. In contrast, for high rate reactions, like they took place at a membrane thickness of 150 nm, a low value of dH/dT per interface was found. Therefore, more energy is released per interface in case of a slow reaction ($\dot{T} = 5.4 \cdot 10^4$ K s^{-1}) compared to a fast reaction. In order to explain this correlation, interdiffusion as the basic mechanism driving the reaction has to be taken into account [14]. Diffusion of atoms is quantified by the diffusion coefficient (see equation 2.9), which is defined by the square of the average diffusion length per time (unit: m^2 s^{-1}) [64]. Therefore, diffusion is a time-dependent process. The correlation between heating rate, interdiffusion and energy release is schematically shown in Figure 4.16. At high heating rates (left illustration), less time for intermixing is available. Consequently, the exothermic diffusion process releases less energy, and dH/dT per interface is reduced. In contrast, in the case of a low heating rate experiment (right illustration), the interdiffusion zone is thicker because the duration of a reaction is elongated. More time is available for the movement of atoms. As a result, the release of dH/dT per interface is significantly

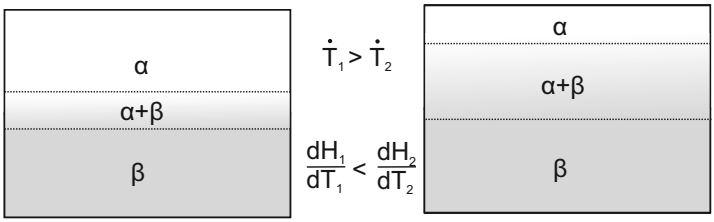

Figure 4.16: Schematical illustration of intermixing in the case of different heating rates $\dot{T}$. With a higher rate (left part), the time for intermixing is reduced, which results in a narrow interdiffusion zone and enhanced exothermic heat release $\dot{Q}$.

higher. It should be noted that this correlation is not necessarily a contradiction to the heating-rate-independent definition of dH/dT in equation 4.7. The quantity dH/dT is only mathematically corrected for the heating rate but does not contribute to heating rate induced changes in the reaction process.

Besides the interface density and the membrane thickness, the influence of the multilayer composition was investigated. Figure 4.17 (a) plots $\dot{Q}_{rct}$ vs. T for of Al/Ni multilayers with a composition of 5, 10, 15, and 25 at.% Ni. Like annotated in Figure 4.17 (a), the number of interfaces changes with the composition from 9 to 27. All specimens were heated with $5 \cdot 10^3$ K s^{-1}. Two different heat release characteristics were identified. Whereas 10, 15 and 25 at.% Ni show a continuous increase of $\dot{Q}_{rct}$, in case of 5 at.% Ni, the rise is interrupted by a plateau starting at about 450 °C. The occurrence of a plateau indicates a phase formation mechanism that proceeds in two stages. This mechanism is discussed in detail in Section 4.3.3. In general, by increasing the Ni content, the $\dot{Q}_{rct}$ the onset of exothermic heat release is shifted to lower temperatures. Only the sample with 15 at.% Ni and 25 at.% Ni show an equivalent $\dot{Q}_{rct}$ behaviour. dH/dT per interfaces is shown in Figure 4.17 (b). Up to 430 °C, all

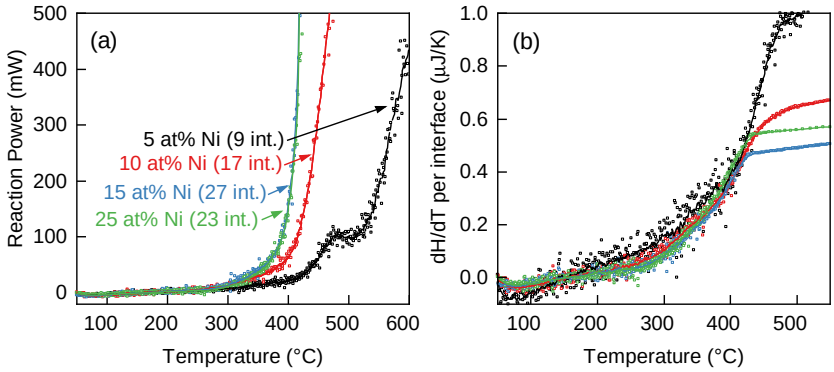

Figure 4.17: The reaction power $\dot{Q}_{rct}$ and the enthalpy change per temperature and interface dH/dT is plotted vs. the temperature. The shift of $\dot{Q}_{rct}$ to lower temperatures is mainly caused by the change of interfaces from 9 at 5 at.% Ni to 23 at 25 at.% Ni, rather by the change of composition.

specimens show a similar increase of dH/dT per interface independent of the composition. As already outlined, the energy released in the initial stage of the reaction is solely dependent on the interface density in the multilayer stack. Exothermic processes like intermixing of Al and Ni are localized at the interface. Thus, the shift of the onset of $\dot{Q}_{rct}$ is primarily explained by the change of the number of Al/Ni interfaces from 9 to 23, rather than the change of the composition. Multilayers where the number of interfaces differs only by 4 (15 at.% Ni and 25 at.% Ni) show similar $\dot{Q}_{rct}$ signals. At temperatures > 430 °C, the dH/dT release is flattened for all compositions whereas for 5 at.% Ni the release of dH/dT is significantly higher. It was found that the heating rate during the reaction is about times lower in the case of 5 at.% Ni compared to the reaction of the 25 at.% Ni sample (compare Figure 4.29 b). The increased heating rate causes a lower amount of intermixing and therefore lowers the dH/dT values per interface.

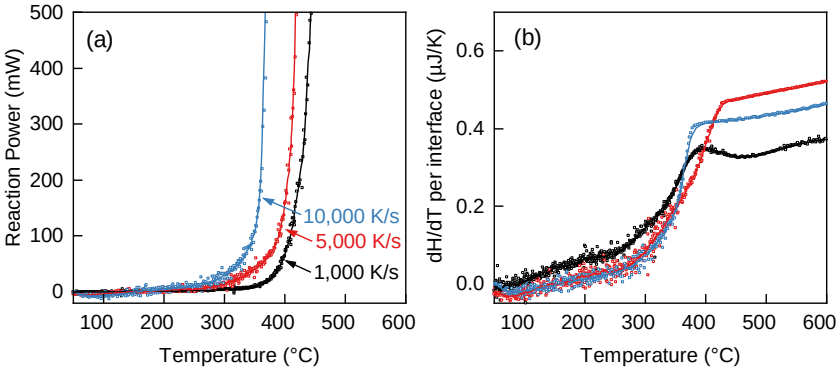

Figure 4.18: (a)The reaction power is shifted to lower temperatures by increasing the heating rate. (b) The enthalpy change per temperature is almost similar for all experiments since there are only minor differences in the heating rate during the reaction.

.

The influence of the heating rate on the energy release is shown in Figure 4.18. For this purpose, the heating rate was varied between $1 \cdot 10^3$, $5 \cdot 10^3$ and $1 \cdot 10^4$ $\mathrm{K\,s^{-1}}$. Here, multilayers with a composition of 15 at.% Ni were used. It was found that the onset of the $\dot{Q}_{rct}$ release is shifted to lower temperatures with the increase of the heating rate. This is expected, since at higher heating rates the reaction power is increased. This amplification of the $\dot{Q}_{rct}$ signal can be seen in Figure 4.18 (a). At 300 °C the exothermic heat release is not resolvable at $1 \cdot 10^3$ $\mathrm{K\,s^{-1}}$ (black curve), whereas there is a clear increase of $\dot{Q}_{rct}$ at $1 \cdot 10^4$ $\mathrm{K\,s^{-1}}$ (blue curve). All three tested rates showed qualitatively identical dH/dT curves. The differences in dH/dT during reaction are mainly caused by unsystematic variations of the heating rate.

So far, the influence of the interfaces, composition and the heating rate was investigated. As a final step, the impact of the surrounding atmosphere on the heat release is examined. Figure 4.19 (a) plots the reaction power vs. the temperature for a 1-µm-thick Al/Ni(7 at.% V) specimen. A bilayer thickness

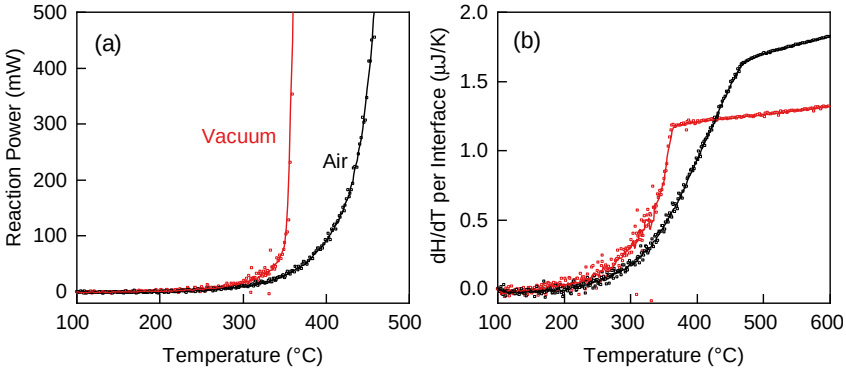

Figure 4.19: (a) The reaction power $\dot{Q}_{rct}$ versus the temperature for an Al/Ni(7 at% V) sample (1 µm, Λ = 166 nm) tested in air and under vacuum conditions ($p < 10^{-4} Pa$). The rapid increase of $\dot{Q}_{rct}$ under vacuum is caused by the faster self-heating of the sample. (b) The enthalpy change per temperature and interface shows that initially the reactions are equivalent and deviate at elevated temperatures due to heating rate effects.

of 166 nm and a sensor membrane thickness of 600 nm was chosen. It is evident that under vacuum conditions ($p < 1 \cdot 10^{-4} Pa$) the reaction power rises more rapidly than under atmospheric conditions. In vacuum, the heat losses are significantly reduced due to the elimination of air convection. This results in increased heating rates and enhanced heat release under vacuum. An additional effect of oxidation in air is unlikely. STEM investigations showed that the Ni-oxide layer formed on the top of the layer stack has a thickness in the range of 1-5 nm. Compared to the exothermic energy release of 11 Al/Ni interfaces, the oxide formation is negligible. Figure 4.19 (b) plots dH/dT per interface. Initially, both curves run in parallel. This is expected since the reaction itself is independent of the surrounding atmosphere. At later stages, the curves deviate, which can be attributed to the influence of the heating rate on dH/dT (compare Figure 4.15).

In summary, the reaction power scales only with the number of interfaces and the heating rate during the reaction. It was found that especially for the initial stages, the composition does not influence $\dot{Q}_{rct}$. However, for later stages of the reaction, Ni is consumed and influence on $\dot{Q}_{rct}$ is expected. For all experiments, the initial part of dH/dT per interface showed similar behaviour. At about 250 °C, the initial energy release is observed. With further reaction progression, flattening of dH/dT is observed. The dH/dT curve proceeds at different levels depending on the heating rate during the reaction. An explanatory approach was presented which explains the change in dH/dT per interface by the different amounts of intermixing at different heating rates. Less intermixing at high heating rates leads to a lower energy release per interface. The heating rate during the reaction can be influenced by intrinsic factors like the interface density or external factors like the sensor membrane thickness, atmosphere or base heating rate.

4.2.2 Ignition criterion [1]

Ignition marks the threshold between a solid-state reaction and a runaway reaction. In the framework of this study, the ignition temperature is important because it defines the limiting conditions between an externally controllable reaction and an uncontrolled runaway reaction. For the determination of the ignition temperature, the reaction power from Section 4.2.1 is used. Excerpts of the section were published by *Neuhauser et al.* [54] [1].

Figure 4.20 shows the individual power contributions during heating of an Al/Ni multilayer sample with $5 \cdot 10^3$ K s^{-1}. In this example, a 1-µm-thick specimen with 25 at.% Ni and Λ = 166 nm was selected. The red line represents $\dot{Q}_{rct}$, the blue line $\dot{Q}_{loss}$ and the black line the difference between $\dot{Q}_{loss}$ and

[1] Excerpts from this section are published in: T. Neuhauser, G. Tinti, H. Leiste, N. Casati, M. Stüber, and K. Woll, "Analysis of the reaction runaway in Al/Ni multilayers with combined nanocalorimetry and time-resolved X-ray diffraction," Acta Materialia, vol. 195, pp. 579–587, 2020.

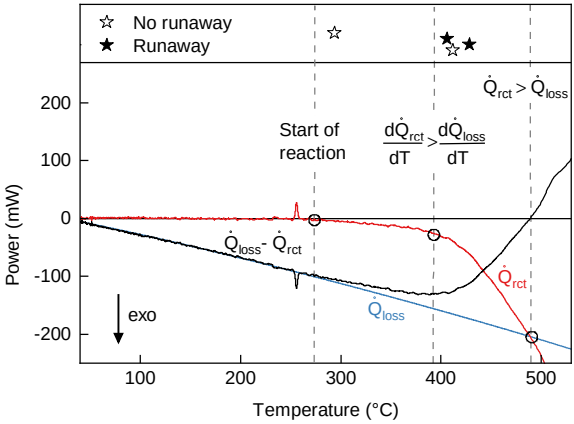

Figure 4.20: Thermodynamic characterisation of a 1 µm (25 at.% Ni, λ = 166 nm) Al/Ni mulitlayer sample. The $\dot{Q}_{rct}$ (red line) overcompensates $\dot{Q}_{loss}$ (blue line) at 490 °C which marks the ignition point according to $\dot{Q}_{rct} > \dot{Q}_{loss}$. Quenching experiments (star symbols) suggest a second ignition criterion $\dot{Q}_{rct}/dT > \dot{Q}_{loss}/dT$ which is defined by the vertex of the $\dot{Q}_{loss} - \dot{Q}_{rct}$ signal (black line). [54]

$\dot{Q}_{rct}$. Starting at room temperature the heat losses increase continuously with temperature. The first evidence of an exothermic reaction starting at 271 °C, apparent by the deviation of $\dot{Q}_{rct}$ from zero. Up to about 400 °C, the amount of $\dot{Q}_{rct}$ is almost negligible compared to $\dot{Q}_{loss}$. The difference $\dot{Q}_{loss} - \dot{Q}_{rct}$ hardly deviates from the heat losses. With increasing temperature, the amount of $\dot{Q}_{rct}$ grows rapidly and starts at 490 °C to overcompensate $\dot{Q}_{loss}$. At the intersection of the black line with the x-axis, the ignition criterion $\dot{Q}_{rct} > \dot{Q}_{loss}$ proposed by *Semenov* [55] is fulfilled (see Section 2.3).

Quenching experiments were performed to check the applicability of the as-defined ignition criterion. By operating the nanocalorimetry sensor under atmospheric conditions, the heat losses are high enough to realize quenching

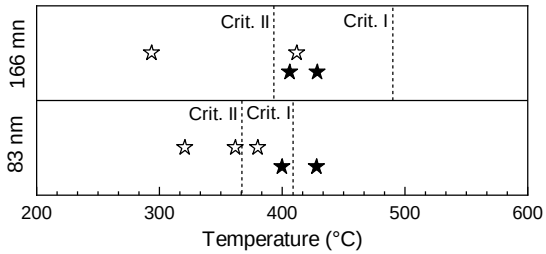

Figure 4.21: Quenching of Λ = 166 nm (upper part) and Λ = 83 nm (lower part) Al/Ni multilayer sample. Filled stars indicate ignition and empty stars quenchable specimens. For both multilayer geometries criterion II (see equation 4.8) is the best description for ignition point.

rates of $\sim 2 \cdot 10^4$ $\mathrm{K\,s^{-1}}$. Samples were heated close to the ignition temperature of 490 °C and subsequently quenched by switching off the power supply. The resulting quenching temperatures are plotted in the upper part of Figure 4.20. Filled stars represent quenching temperatures where a runaway reaction was observed. Open symbols represent temperatures where quenching of the sample was possible. It was found that ignition occurs already at 410 °C. This is 80 °C lower than predicted by the ignition criterion $\dot{Q}_{rct} > \dot{Q}_{loss}$. Based on these findings, we suggest the following criterion:

$$\frac{d\dot{Q}_{rct}}{dT} > \frac{d\dot{Q}_{loss}}{dT} \tag{4.8}$$

In the following, this criterion for ignition is denoted criterion II, whereas the criterion from *Semenov* [55] is denoted criterion I. Beside Al/Ni with Λ = 166 nm, specimen with Λ = 83 nm were tested. Figure 4.21 shows the results. Again a runaway reaction is observed at temperatures lower than predicted by criterion I. This confirms the validity of ignition criterion II. However, in one case quenching was feasible above the ignition criterion II. Since the deviation

is less than 20 °C, variations in the sample conditions are the most likely explanation. Besides this, Figure 4.21 demonstrates that the temperature distance between criteria I and II is lowered from Λ = 166 nm to Λ = 83 nm. The reason for this is the higher reactivity of the 83-nm-sample. Due to a higher interface density, the reaction power increases faster (compare Figure 4.14), which leads to a rapid succession of both ignition criteria. In the limit case of a very reactive specimen or high heating rates, it can be expected that both criteria almost coincide.

In contrast to criterion I, not only the absolute power contributions but the dynamic of the reaction is taken into account. Ignition is easier for a reaction that is accelerating compared to a decelerating one. In this context an accelerating reaction is a reaction where $d(\dot{Q}_{loss} - \dot{Q}_{rct})/dT > 0$. The amount of $\dot{Q}_{rct}$ increases continuously. Here, we propose an explanatory model for the validity of ignition criterion II, which is based on the overshooting of the reaction power. In the theoretical framework of ignition, the ignition delay is the period of time between external stimulus and thermal runaway. This concept is illustrated in Figure 4.22. Although the external power input is stopped, the reaction continues. Nanocalorimetry sensors provide an ultrafast temperature response due to the low thermal mass. However, a short period of time is needed to decelerate heating and initiate the cooling of the system. This amount of time is caused by the heat capacity of the system and is typically in the $\sim$ ms range. Within this period of time, further reactions can take place, which potentially leads to further heating and an 'overshoot' of the reaction power (see Figure 4.22 (a)). For instance, in case of 12 to 25 µm thick Al/Ni films, *Fritz et al.* [18] observed a runaway reaction up to 146 ms after switching off external heating. Within this time frame, atomic movement takes place and exothermic heat is released. Since ignition criterion I does not take the ignition delay into account, the actual ignition temperature is lower than predicted. According to the experimentally determined temperatures for ignition shown in Figure 4.21 criterion II seems to reflect the ignition delay better than

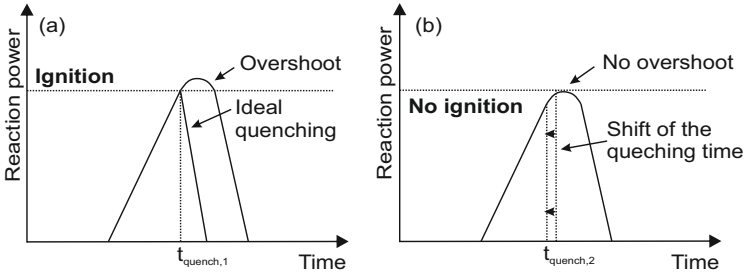

Figure 4.22: Schematic illustration of the ignition delay. (a) After switching off the external heating, further heat is released due to exothermic reactions (overshoot). (b) The ignition can be avoided by earlier quenching of the sample. The reaction power remains below the critical ignition limit.

criterion I. Using ignition criterion II is equivalent to early quenching of the sample (see Figure 4.22 (b)). In this way, the reaction power stays below the critical limit of ignition.

In literature, experimentally verified criteria for ignition are rare. In order to determine the ignition temperature of reactive multilayers, there are two major approaches: hot-plate experiments, where multilayer specimen are dropped onto a heating plate with a defined temperature [6, 53] and resistance heating experiments where the specimen are heated directly by a current [18, 19]. These methods allow the determination of ignition by the temperature signal but lack the thermodynamic characterization. This brings two major drawbacks: (i) since the ignition criteria are defined by thermodynamic quantities, a direct verification is not possible and (ii) ignition temperatures are not comparable. The latter one results from the dependency of the ignition temperature from the sample and the thermodynamic system. As outlined in Section 4.2.1, the heat capacity and the heat losses are additional contributions that influence the ignition point. Using nanocalorimetry, the characterization of the ignition

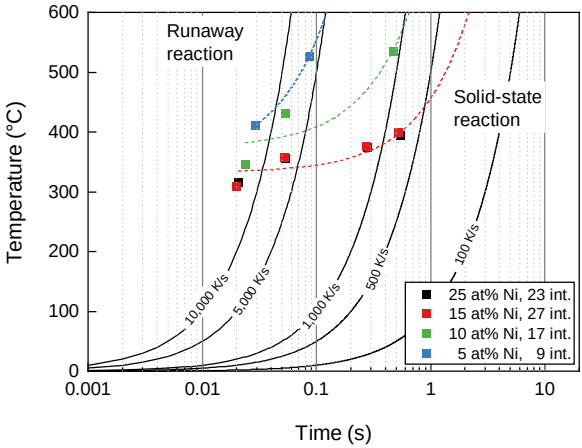

Figure 4.23: The ignition temperatures are plotted versus the time on a logarithmic scale. Al/Ni multilayers with a composition between 5 at.% Ni and 25 at.% Ni were tested between 100 $\mathrm{K\,s^{-1}}$ and 10^4 $\mathrm{K\,s^{-1}}$. For illustration, the linear heating curves are plotted in black lines. It was found that the ignition temperature decrease with increasing heating rate and interface density. At 500 $\mathrm{K\,s^{-1}}$ the lower limit for ignition of the Ni-rich multilayers is reached.

temperature based on thermodynamic quantities is accessible. Therefore, direct and universal characterization of the ignition behaviour of reactive materials is possible independent of the sample geometry and thermodynamic boundary conditions.

Based on the reaction power determined in Section 4.2.1, the ignition temperature is characterized by dependence of composition, interface density, sensor membrane thickness and surrounding atmosphere. In all cases, ignition criterion II was used. Figure 4.23 plots the ignition temperature on the y-axis and time in the logarithmic scale on the x-axis. Al/Ni multilayers with a compositional range of 5-25 at.% and heating rates between $5 \cdot 10^2$ $\mathrm{K\,s^{-1}}$ and $1 \cdot 10^4$ $\mathrm{K\,s^{-1}}$ are compared. All specimens were 2 µm thick. Exemplarily, linear heating curves are plotted in black lines. As a guide to the eye, the

ignition temperature characteristics are indicated with dashed lines. The ignition time is derived based on the heating rate during reaction determined in a temperature regime between 300 °C and the ignition temperature. The ignition temperature is plotted in Figure 4.23. Two observations can be made: (i) the ignition temperature is lowered with increasing heating rate and (ii) the ignition temperature increases with decreasing Ni content, respectively, with decreasing number of Al/Ni interfaces. The lowest ignition temperature was found at 313 °C in case of 15 at.% and 25 at.% Ni, heated with $1 \cdot 10^4$ $\mathrm{K\,s^{-1}}$. The highest ignition temperature was 535 °C in the case of 10 at.% Ni heated with $1 \cdot 10^3$ $\mathrm{K\,s^{-1}}$. The ignition temperatures of 15 at.% Ni and 25 at.% Ni are almost identical. This is explained by the number of Al/Ni interfaces in the sample that differs only by 4. This points to the relevance of the interface density for ignition. It was found that for the type of sample used in this study, the lower heating rate limit for ignition is $5 \cdot 10^2$ $\mathrm{K\,s^{-1}}$. Below ignition, the solid-state reaction is dominating. Typically, this is the case for slow heating conditions and low temperatures. In contrast to the runaway reaction, the solid-state reaction can be quenched. However, beyond the ignition line, the reaction propagates by its own.

The influence of the number of interfaces on the ignition temperature is shown in Figure 4.24 (a). Heating of a 1-µm-thick sample with $5 \cdot 10^3$ $\mathrm{K\,s^{-1}}$ shows that the reduction of the number of Al/Ni interfaces from 23 to 11 increases the ignition temperature from 346 °C to 383 °C. Typically, ignition occurs in the early stages of the reaction. The reaction power during these early stages of the reaction is dominated by the number of Al/Ni interfaces (compare Figure 4.14 (a)). If the number of interfaces is unchanged, the composition of the sample has a minor impact on ignition. Instead, the reaction power at later stages of the reaction is determined by the composition. In Figure 4.24 (b), the ignition temperature of Al/Ni(7 at.% V) as a function of the thickness of the nanocalorimetry membrane is plotted. Again, all specimens were heated with $5 \cdot 10^3$ $\mathrm{K\,s^{-1}}$. It was found that the ignition temperature increases with

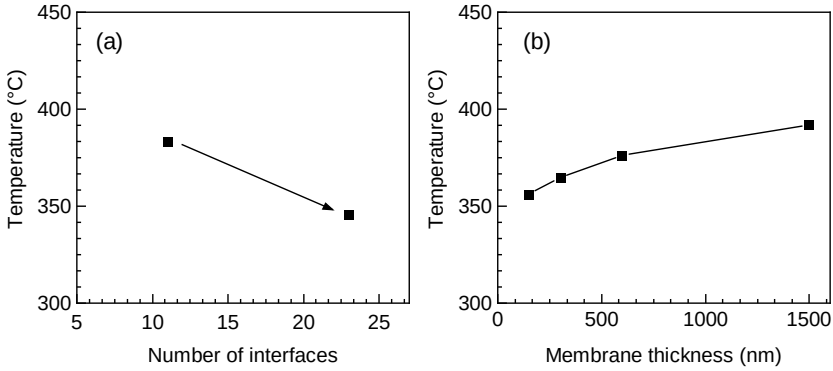

Figure 4.24: Ignition temperature as a function of (a) the number of interfaces in a 1-µm-thick Al/Ni multilayer sample and (b) the membrane thickness of the nanocalorimetry sensor. With increasing membrane thickness, the heat capacity of the system increase.

sensor membrane thickness. From 150 nm to 1500 nm, a temperature increase of 36 °C is observed. Since there is no chemical interaction between Al/Ni and the sensor membrane, the shift of the ignition point is caused by the different thermodynamic surrounding. As outlined in Section 3.1.5, the heat capacity and the heat losses increase with the membrane thickness. As a consequence, the heating rate during reaction is reduced (see Figure 4.15 (a)) and consequently, ignition temperature increase. This clearly proves that the ignition temperature is not exclusively a function of the multilayer geometry but also of the thermodynamic conditions of the surrounding.

Besides the sensor membrane thickness, the atmospheric conditions influence the ignition temperature. Figure 4.25 plots the ignition temperatures of a 1-µm-thick Al/Ni (7at.% V) specimen in vacuum and air. In both experiments, the bilayer thickness was 166 nm. It was found that there is a decrease of the ignition temperature of 90 °C when the atmosphere is changed from air to vacuum ($p < 1 \cdot 10^{-4}$ Pa). This is caused by the significantly lower heat losses in vacuum. The sample heats up faster, which results in higher values of the reaction

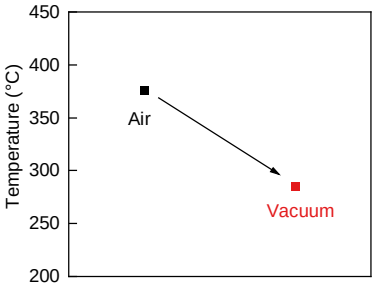

Figure 4.25: The influence of the atmospheric conditions on the ignition temperature of Al/Ni(7at.% V) multilayer samples (1 µm, Λ = 166 nm).

power. Due to the low heat losses and increased reaction power, the condition for ignition according to equation 4.8 is reached at lower temperatures.

4.3 Fast heating rates: Runaway reactions

When heated above the ignition temperature, the reaction turns into a self-sustaining runaway reaction. In contrast to slow heating discussed in Section 4.1, the reaction is not externally controlled. The characteristics of the exothermic heat release, which was quantified in Section 4.1, determines the reaction temperature. The high heating rates and the peak temperature affect the underlying mechanism of the reaction. Besides solid-solid interdiffusion, now diffusion in liquid-solid conditions gains in importance. First, the runaway reaction is characterized using *in situ* X-ray diffraction in Section 4.3.1. In Section 4.3.2, parameters are identified which influence the runaway reaction. The special case of solid-state runaway reactions is considered in Section 4.3.3. The early stages of the reaction, with a special focus on the mechanism prior to ignition, are investigated in Section 4.3.4. The underlying mechanism for arbitrary runaway reactions is discussed in Section 4.3.5.

4.3.1 Liquid-state runaway reactions [2]

The runaway reaction was investigated by using nanocalorimetry in combination with synchrotron X-ray diffraction. The results of this investigation were published by *Neuhauser et al.* in [54] [2]. Al/Ni multilayers with Λ = 166 nm and a total thickness of 2 µm were deposited on a nanocalorimetry sensor with a membrane thickness of 150 nm. A composition of 25 at.% Ni was chosen. The sample was ignited by linear heating at $5.7 \pm 0.1 \cdot 10^3$ K s^{-1}. Figure 4.26 plots the temperature profile of the reaction. This reaction is representative of numerous liquid-state runaway reactions in the course of this study.

[2] Excerpts from this chapter are published in: T. Neuhauser, G. Tinti, H. Leiste, N. Casati, M. Stüber, and K. Woll, "Analysis of the reaction runaway in Al/Ni multilayers with combined nanocalorimetry and time-resolved X-ray diffraction," Acta Materialia, vol. 195, pp. 579–587, 2020.

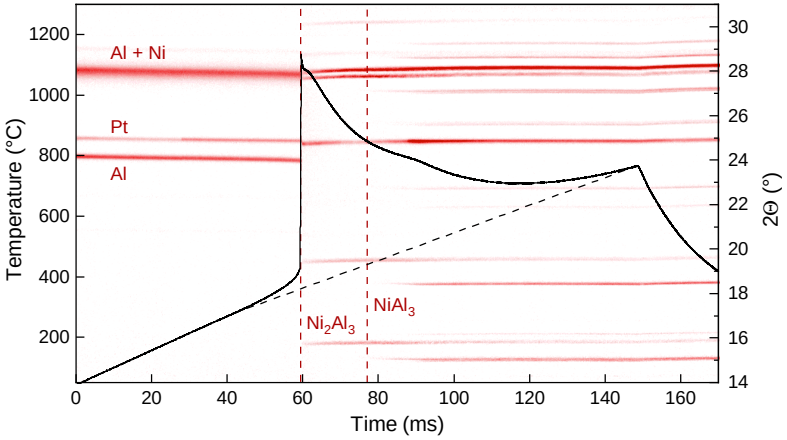

Figure 4.26: Runaway reaction of Al/Ni multilayers with 25 at.% Ni and Λ = 166 nm. The sample was heated using nanocalorimetry combined with time-resolved X-ray diffraction. The temperature curve is plotted in black, while the corresponding diffractograms are shown in red. It was found that during the reaction, the sample pass through the stages of interdiffusion, Al_3Ni_2 and Al_3Ni phase formation. [54]

Up to 350 °C, the sample temperature increases linearly with time, which is a result of the external heating via the nanocalorimetry sensor. The external power input is maintained up to 148.5 ms. The theoretical temperature profile without the reaction power contribution of the sample is illustrated by the dashed black line. Above 350 °C, the temperature deviates from linear heating, followed by a major temperature increase at 425 °C (t = 59.2 ms). This sudden temperature increase of 709 °C within 0.385 ms is called the thermal runaway reaction. Here, the highest temperature of 1134 °C and the largest heating rate of $2.8 \cdot 10^5$ K s^{-1} was observed. After the runaway reaction the sample cools down to 708 °C (t = 117.6 ms) driven by the heat losses to the surrounding. The cooling curve exhibits two temperature plateaus at 1073 °C and 788 °C. It follows a second temperature increase. This is not attributed to an exothermic reaction but to the ongoing external heating up to 148.5 ms.

In the background of Figure 4.26, the time-resolved X-ray diffractograms are plotted in red colour. At the beginning of the experiment, four diffraction peaks can be identified: Al ($2\theta_{Al(111)} = 24.14°$, Pt ($2\theta_{Pt(111)} = 24.96°$), Pt ($2\theta_{Pt(200)} = 28.97°$) and an overlapping Al + Ni ($2\theta_{Al(111),Ni(200)} = 28.02°$) peak. It should be noted that the origin of the Pt peaks is the heating strip of the sensor and is therefore not involved in the reaction. For all peaks, a shift of the peak position with temperature is observed, which is equivalent to an extension of the lattice parameters. This can be attributed to a combined effect of thermal expansion on the one side and internal stresses on the other side. Stresses arise due to the mismatch of the coefficient of thermal expansion between Al, Ni and Pt. Two phase transformations can be observed by X-ray diffraction. The first one takes place during the thermal runaway reaction. The Al peaks disappear while new diffraction peaks are formed in a 2θ range between 15.72° and 30.10°. These peaks can be clearly assigned to the Al_3Ni_2 phase. Since the temperature quickly exceeds the melting point of Al (T_m = 660 °C), it can be expected that Al turns into the liquid state and is consumed during the formation of Al_3Ni_2. The peak intensity increases up to t = 82 ms, which indicates phase growth. The second phase transformation occurs during the cooling of the sample. Below 788 °C, the Al_3Ni phase precipitates. Simultaneously, the Al_3Ni_2 peak intensity decreases. Hence, Al_3Ni_2 is transformed into Al_3Ni. At room temperature, the sample consists of two phases, namely Al_3Ni and Al_3Ni_2. The reactants Al and Ni were fully consumed during the reaction.

A detailed investigation of the major temperature increase was performed to reveal the mechanism driving the runaway reaction. Figure 4.27 (a) plots the time-resolved temperature evolution.. The corresponding X-ray diffractograms are shown in 4.27 (b). Four individual reaction stages were identified:

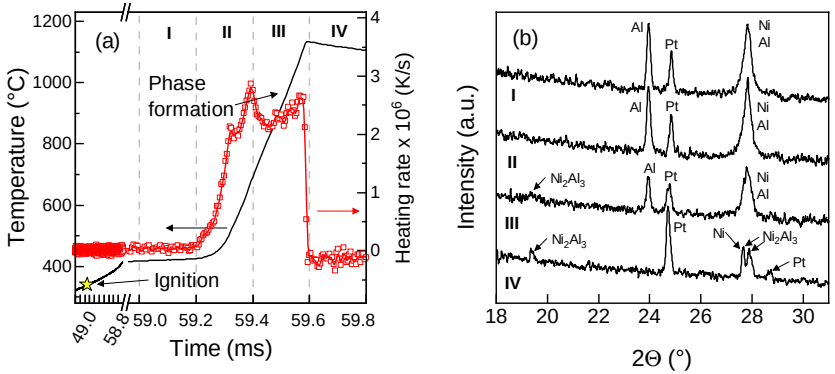

Figure 4.27: (a) Nanocalorimetry signal of the runaway reaction depicted in Figure 4.26. Based on the heating rate signal (red), four reaction stages were identified. (b) X-ray diffractograms of the individual reaction stages. Formation of the product phase Al_3Ni_2 was not observed until Stage III. [54]

Stage I

At the beginning of the runaway reaction, the temperature signal is predominantly defined by the sensor heating. The X-ray diffractograms show only the elemental peaks of Ni, Al and Pt. Formation of any type of product phase is not present. However, the calorimetric analysis plotted in Figure 4.17 (a) reveals that the exothermic heat release starts already at 271 °C. In fact, the ignition point represented by the golden star (= reaction becomes self-sustaining) is already reached long before Stage I at 338 °C. Within Stage I, no phase formation was observed. This points to intermixing as the dominant mechanism. The calculated energy of $1.80 \cdot 10^3 \mathrm{J\,cm^{-3}}$ for the initiation of a runaway reaction is in good agreement with values reported for Al/Ni(V) multilayers. [18].

Stage II

Within Stage II, the major temperature increase occurs. The heating rate data shows a peak at 693 °C. Here, the highest values for the heating rate with $3 \cdot 10^6$ K s^{-1} were found. Most likely, the heating rate peak is related to the onset of Al melting. There is no difference in the diffracted signal compared to Stage I. Still, only diffraction peaks of Al, Ni and Pt are present and there is no change in the peak intensity. It is found that there is a time delay between the ignition point (yellow star) and the latter temperature increase of 7.75 ms. This phenomenon, called ignition delay, is generally observed in reactive materials. A theoretical description of this phenomenon can be found in Section 2.3.

Stage III

In Stage III, changes in the diffracted X-ray signal can be detected. Compared to Stage II, the intensity of the Al peak at $2\theta = 24°$ decreases, which indicates the melting of major amounts of the Al phase. Simultaneously, the heating rate drops to values between $2 \cdot 10^6$ and $2.5 \cdot 10^6$ K s^{-1}. A melting temperature of Al of at least 693 °C was determined. This is above the literature value of 660 °C. A possible explanation for this deviation is the superheating of solid Al at high heating rates [144]. Perturbations of the nanocalorimetry temperature measurement are not expected. Temperature calibration experiments with 2-µm-thick Al thin film as shown in Appendix A.4 prove the temperature accuracy of the measurement. However, since the heating rate deviates from the conditions in runaway reactions, temperature inhomogeneities cannot be completely ruled out. The diffracted X-ray signal gives some indications for the formation of Al_3Ni_2 peaks. This can be attributed to the formation of a minor amount of phase, most likely at the end of Stage III. At the end of the stage a peak temperature of 1134 °C is reached.

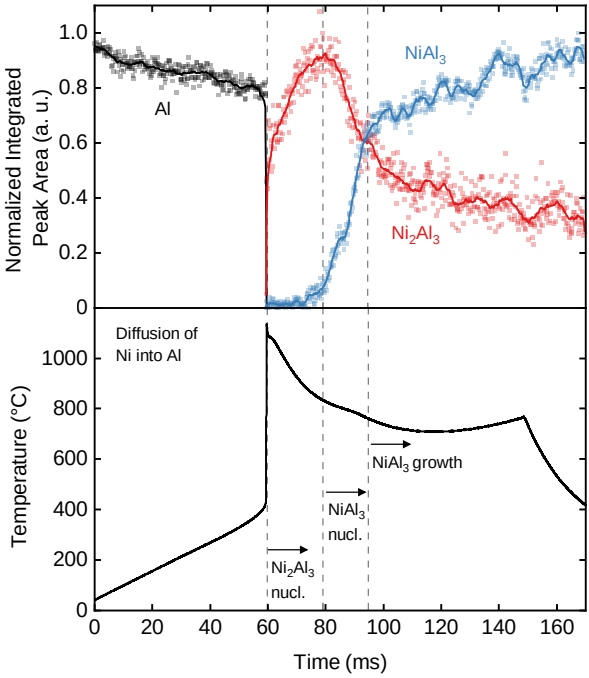

Figure 4.28: Temporal evolution of the normalized integrated peak intensity of Al, Al_3Ni and Al_3Ni_2. The formation of Al_3Ni_2 proceeds up to 20 ms after the maximum reaction temperature was exceeded. With further cooling, Al_3Ni_2 decomposes into Al_3Ni. [54]

Stage IV

By exceeding the peak temperature of 1134 °C (t = 59.6 ms), a sudden drop of the heating rate is observable. The part of the reaction where the exothermic heat release is dominating the reaction is completed. Now, the heat losses cool down the sample gradually. At the same time, the Al peak disappears and pronounced peaks of Al_3Ni_2 are formed. The Al phase is now completely in the molten state and is getting consumed in the course of the Al_3Ni_2 phase

formation.With further cooling of the sample, the growth of Al_3Ni_2 phase is facilitated. Figure 4.28 plots the normalized integrated peak intensity of Al, Al_3Ni and Al_3Ni_2 based on the *in situ* XRD data. To a good approximation, the integrated peak intensity is equal to the amount of phase in the sample (see Appendix A.5). A moving average smoothing was applied to reduce the scattering of the data (solid line). It has to be noted that Ni was not evaluated. Overlapping of the Ni peaks with other phases makes integration difficult and therefore prone to errors. The maximum amount of Al_3Ni_2 was found 20 ms after the runaway reaction. Hence, 50 % of Al_3Ni_2 is formed after the peak temperature is exceeded and does not contribute to the temperature evolution of the reaction. Below 882 °C, Al_3Ni_2 decomposes and Al_3Ni is formed. With further reaction progression, the amount of Al_3Ni continuously increases. At the end of the reaction, about 70 % of the initial formed Al_3Ni_2 are transformed into Al_3Ni.

4.3.2 Runaway reaction kinetics

In the next step, the impact of the experimental parameters like the heating rate, composition, nanocalorimetry sensor geometry and annealing conditions on the runaway reaction kinetics were characterized. So far, the influence of these parameters was only studied for self-propagating reaction fronts [9, 27, 31, 48, 145]. Although this gives valuable information about the peak temperatures and reaction waves velocities, the actual temperature profile and the phase sequence is unknown. Therefore, nanocalorimetry was used to investigate the impact of the composition and the heating rate on temperature profile of the reaction.

Figure 4.29 plots the temperature profiles of various Al/Ni runaway reactions with a Ni content between 5 at.% and 25 at.% Ni and a heating rate between $5 \cdot 10^2$ $\mathrm{K\,s^{-1}}$ and $1 \cdot 10^4$ $\mathrm{K\,s^{-1}}$. All reactions fulfil the criterion of ignition

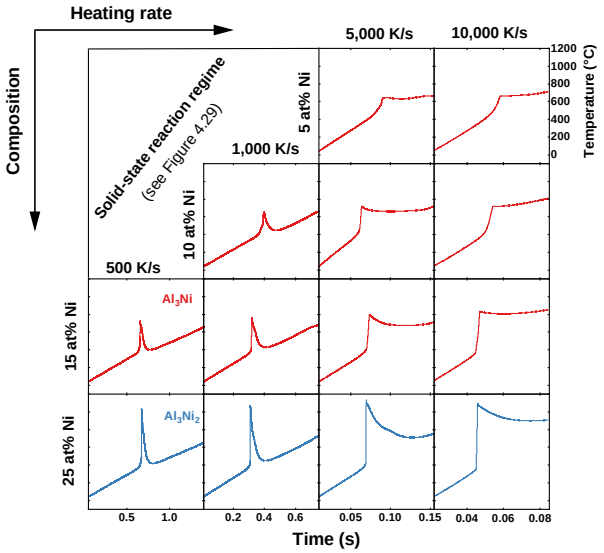

Figure 4.29: Overview of the temperature profiles of Al/Ni runaway reactions in a compositional range between 5 at.% and 25 at.% Ni and a heating rate of 500 $\mathrm{K\,s^{-1}}$ up to 10^4 $\mathrm{K\,s^{-1}}$. The reaction temperatures are lower in Al-rich samples. In case of 25 at.% Ni, the temperatures exceeds 1000 °C and Al_3Ni_2 is formed first. The temperature profiles for heating rates < 500 $\mathrm{K\,s^{-1}}$ are depicted in Figure 4.3.

derived in Section 4.2.2, which confirms the presence of a runaway reaction. Generally, it was found that the maximum temperature of the reaction increases with Ni content and heating rate. The latter shows significantly less influence on the temperature profile. In this study, the lowest runaway temperature observed was 646 °C in case of 5 at.% at $5 \cdot 10^3$ $\mathrm{K\,s^{-1}}$ and the highest temperature 1134 °C in case of 25 at.% at $5 \cdot 10^3$ $\mathrm{K\,s^{-1}}$. Since the peak temperatures are above and below the melting temperature of Al, it is expected that the runaway reaction proceeds in the solid and the liquid state of the sample. A detailed

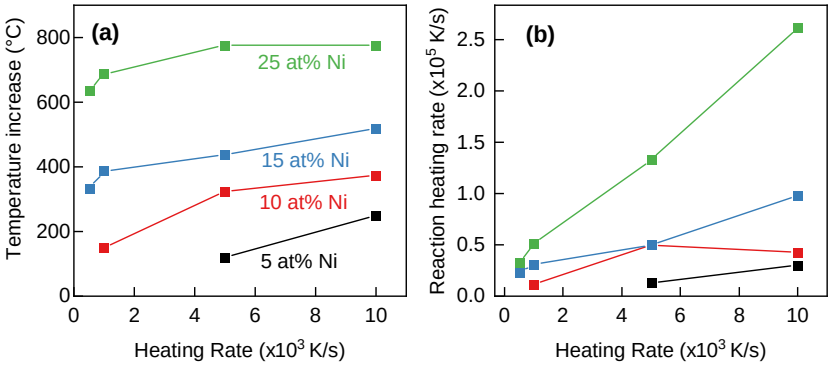

Figure 4.30: (a) Temperature increase and (b) reaction heating rate of a runaway reaction in Al/Ni multilayers as a function of composition and base heating rate. The highest temperature increase and fastest reaction were observed in samples with 25 at.% Ni.

discussion about the difference in the reaction mechanism can be found in Section 4.3.5.

The difference between ignition point and maximum temperature is plotted in Figure 4.30 (a). It becomes evident that the exothermic temperature increase is more pronounced at higher Ni concentrations. Whereas for 5 at.% Ni the temperature increase is only about 250 °C, at 25 at.% there is an increase of 776 °C. This is expected since in the compositional range investigated, the enthalpy of the formation increases with Ni content (compare Figure 2.4). In contrast, it was found that the influence of the heating rate is less pronounced. Exemplarily, at 25 at.% Ni the runaway reaction temperature increases by 140 °C when the heating rate rises from $5 \cdot 10^2$ $\mathrm{K\,s^{-1}}$ to $1 \cdot 10^4$ $\mathrm{K\,s^{-1}}$. However, the result indicates that the peak temperature cannot be increased any further with an increase of the heating rate. The average heating rate of the reaction, here denoted as reaction heating rate (RHR), is plotted in Figure 4.30 (b). Since the RHR is primarily determined by the rate of heat release and, therefore, by the conversion rate from reactants to products, the RHR is a measure for the

reaction rate. Generally, all compositions show an increase of the RHR with the base heating rate. The highest values of RHR were found for multilayers with 25 at.% Ni. These findings suggest a dependence of the heating rate on the composition and the number of Al/Ni interfaces. Note that the number of interfaces changes with composition. The interfaces are the locations where atomic intermixing takes place. More interfaces lead to a faster release of exothermic heat and, therefore, more rapid conversion to the product phase (compare Figure 4.14). Especially above the melting temperature of Al, a high Ni content leads to fast heating and high peak temperatures.

Two different types of primary formed intermetallic phases were observed. For all experiments with $c \leq 15$ at.% Ni, Al_3Ni is the first phase, indicated by a red line in Figure 4.29. In all experiments with $c = 25$ at.% Ni, Al_3Ni_2 is formed first (blue line). This suggests that in the heating rate regime between $5 \cdot 10^2$ K s^{-1} and $1 \cdot 10^4$ K s^{-1} the type of the first phase is primarily dependent on the composition. However, this simplification does not take the temperature stability of Al_3Ni and the physical state of the sample into account. Considering the Al-Ni phase diagram (Figure 2.3), above 854 °C Al_3Ni_2 is the only thermodynamic stable phase in a compositional range between 15 at.% and 36.8 at.% Ni. Therefore, the composition is not the primary factor defining the first phase. In fact, the composition in combination with the number of interfaces defines the reaction temperature, which is decisive for the thermodynamic stability of a compound phase. In case of 15 at.% Ni the reaction temperature does not exceed 827 °C, which is too low for the formation of Al_3Ni_2.

Besides the composition and heating rate, the influence of annealing prior to ignition was studied. For this purpose, Al/Ni multilayers with 25 at.% Ni were annealed at a constant temperature of 250 ± 4 °C. This is well below the ignition temperature of 338 °C for this system. The annealing time was

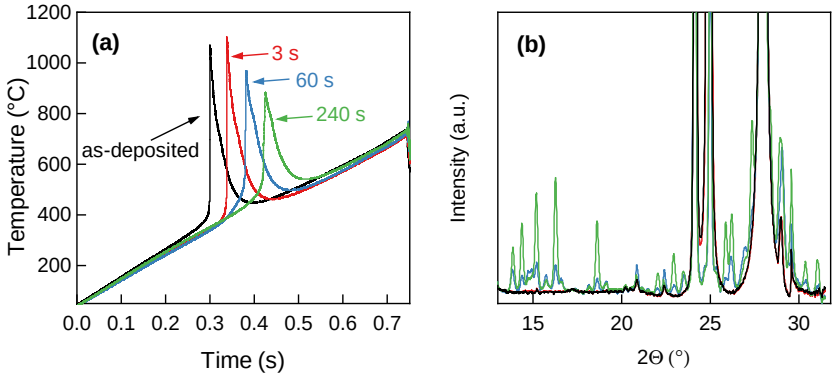

Figure 4.31: The temperature profile of runaway reactions after annealing. Al/Ni multilayer stacks with 25 at.% Ni serve as starting material for a pre-reaction annealing procedure at $\sim$ 250 °C for 3 s to 60 s and 240 s. A reduction of the peak temperature and an increase of the runaway onset was observed with increasing annealing time.

incrementally increased from 3 s to 60 s and 240 s. This experimental approach mimics the isothermal heating shown in Section 4.1.1. The structural changes caused by annealing were characterized by XRD. The diffractograms in Figure 4.31 (b) reveal phase formation in the case of 60 s and 240 s annealing time. The peaks indicate that predominantly Al_9Ni_2 and Al_3Ni is formed. However, at an annealing time of 3 s, the diffractogram does not show any difference to the as-deposited state. After annealing, the samples were ignited at a heating rate of $1 \cdot 10^3$ K s^{-1}. Figure 4.31 (a) show the resulting temperature profiles in comparison to the as-deposited state. Two observations can be made: (i) in case of 60 s and 240 s annealing time, the onset of the reaction is shifted to higher times and temperatures, while the peak temperatures decrease and (ii) there is a slight increase of the peak temperature after 3 s annealing. The first observation can be explained by the reduction of the heat of formation due to phase growth during annealing. Since the multilayers are partially reacted after annealing, the amount of Al and Ni reactants is reduced. Consequently, the peak temperatures of the as-deposited sample are not reached

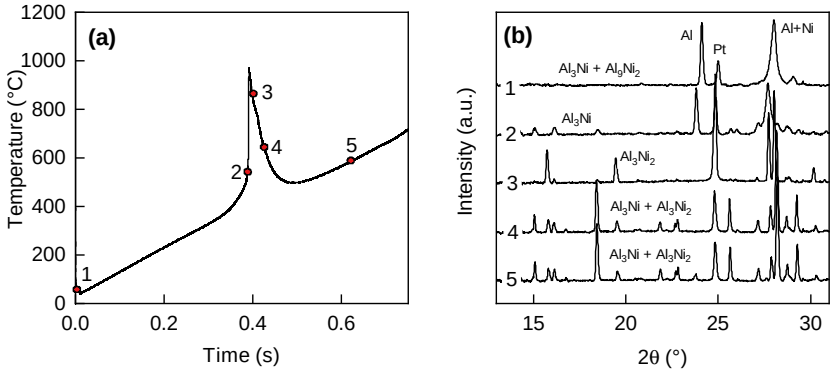

Figure 4.32: (a) Temperature profile of a Al/Ni runaway reaction after annealing 60 s @ 250 °C. (b) X-ray diffraction reveals that the runaway reaction is initiated by Al_3Ni phase growth. After the peak temperature is exceeded, Al_3Ni and Al_3Ni_2 are formed.

in case of long annealing times. The situation is different in case of 3 s annealing. Here, the peak temperature is increased by about +32°C, while the onset of the reaction remains constant. Based on the experimental results, it is difficult to draw a conclusion about the influence of short annealing times on the runaway reaction. Above 1000 °C deviation of temperature measurement can not be excluded with certainty and more measurements are required for a reliable database. However, the temperature increase can indicate the increase of the reactivity for short annealing times. Studies showed that the formation of amorphous layers and Al_3Ni crystals by ion irradiation enhance the reactivity of multilayer materials [25]. Interdiffusion and the formation of nanoscale nuclei by annealing may also reduce the thermodynamic barrier for phase formation (see Section 2.4.1) and therefore enhance the reactivity of the sample.

To get a better understanding of the structural changes during reaction, Figure 4.32 plots the temperature profile (a) and selected *in situ* recorded diffractograms (b) of a runaway reaction after 60 s annealing. The selected

diffractograms are numbered with (1)–(5) and marked as red circles in Figure 4.32 (a). (1) Prior to ignition, Figure 4.31 proves the formation of minor amounts of Al_9Ni_2 and Al_3Ni. (2) By heating the sample, the runaway reaction is initiated. The diffractogram shows an increase of the Al_3Ni amount associated with the exothermic temperature release. Up to 544 °C, the phase growth proceeds below the melting point of all constituents and therefore in the solid state of the sample. (3) Shortly after the peak temperature of the reaction is exceeded, Al_3Ni_2 is formed while the Al_3Ni is predominantly decomposed. (4) During cooling of the sample, the phase ratio is reversed. The amount of Al_3Ni increases and Al_3Ni_2 gets decomposed. (5) In the final diffractogram, the amount of Al_3Ni and Al_3Ni_2 remains constant, whereas the unreacted Al solidifies. Since the product phase is partly formed prior to the runaway reaction, the reaction mechanism differs from the liquid-state runaway reaction shown in Figure 4.27. A detailed description of this liquid-state runaway reaction with compound layer and the distinction to the liquid-state runway is made in Section 4.3.5.

So far, the sample chemistry and annealing conditions were identified as parameters influencing the runaway reaction. Now the question is addressed in which way the runaway reaction is affected by the external thermodynamic conditions. For this purpose, the thickness of the sensor membrane was varied between 150 nm, 300 nm, 600 nm and 1,500 nm. As outlined in Section 3.1.5, this has an impact on the heat losses and especially on the heat capacity. The sample was held constant at a thickness of 1 µm and a composition of 25 at.% Ni(V). Figure 4.33 plots the temperature profile of the runaway reaction for different types of sensors. With increasing membrane thickness, the peak temperature not only decreases from 1032 °C to 869 °C but also the reaction slows down. In case of 150 nm the conversion takes 1.8 ms whereas the time is increased to 29.6 ms in the case of 1,500 nm. An increase of the membrane thickness adds C_P to the system. Thus, more thermal power is required to heat the system. Investigations of self-propagating reaction fronts in

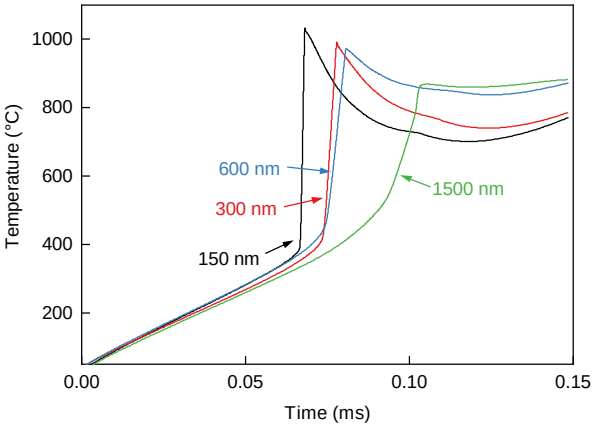

Figure 4.33: Influence of the sensor membrane thickness on the temperature profile of runaway reactions. With increasing thickness, the additional inert heat capacity increase. Consequently heating rate and the peak temperature of the runaway reaction decrease.

inert-mediated reactive multilayers give some evidence that the reaction mechanism is influenced by the reaction kinetics [110]. Here, an inert material like copper is introduced into the multilayer stack. Based on the activation energy analysis, a change of the reaction mechanism from Ni diffusion into liquid Al to atomic transport through a product phase layer is proposed. Although in the present study, no XRD data is available, it can be assumed that at a longer reaction time, phase formation is also facilitated (see Section 2.4.1). Therefore it is possible that the mechanism, which is driving the runaway reaction change with reaction time.

4.3.3 Solid-state runaway reactions [3]

Most of the reactions presented in Section 4.3.2 proceed in the liquid-state of at least one constituent. The liquid state of Al increases significantly the rate of intermixing and leads to high heating rates, which are observed in runaway reactions. The question arises, if the liquid-state of one constituent is a mandatory condition for the presence of a runaway reaction. Can the diffusivity of a solid Ni/ solid Al system be high enough to enable a runaway reaction? Generally, a mandatory criterion for a solid-state runaway is a melting temperature of all constituents above the adiabatic reaction temperature [146]. *Neuhauser et al.* [126] addressed the question if the low melting temperature of Al (T_m = 660 °C) enables a solid-state runaway reaction. [3]

An intermediate heating rate regime between 100 $\mathrm{K\,s^{-1}}$ and $1 \cdot 10^3$ $\mathrm{K\,s^{-1}}$ was chosen to study the solid-state runaway. Al/Ni multilayers with a Ni content of 10 at.% and a bilayer thickness of 220 nm were used. The temperature profiles of the nanocalorimetry experiments are shown in Figure 4.34. In case of 100 $\mathrm{K\,s^{-1}}$ and 500 $\mathrm{K\,s^{-1}}$, two separate peaks are observed. At 100 $\mathrm{K\,s^{-1}}$, the onset of the first peak is at 343 °C and of the second peak at $\sim$ 407 °C. By increasing the heating rate to 500 $\mathrm{K\,s^{-1}}$, the onset of the first peak is shifted by +24 °C and of the second peak by +38 °C. These two temperature peaks can be attributed to the two-stage phase formation discussed in Section 4.1.2 and 4.1.3. The two-stage phase formation comprises a nucleation and a growth step of one phase. The temperature increase within one peak is substantially more pronounced in the case of 500 $\mathrm{K\,s^{-1}}$. This is explained by the increase of $\dot{Q}_{rct}$ when the time interval of the reaction is shortened. At a heating rate of $1 \cdot 10^3$ $\mathrm{K\,s^{-1}}$, a shift from two exothermic peaks to the one temperature

[3] Excerpts from this chapter are published in: T. Neuhauser, G. Tinti, H. Leiste, N. Casati, S. Ulrich, M. Stüber, and K. Woll, "The role of two-stage phase formation for the solid-state runaway reaction in Al/Ni reactive multilayers," Applied Physics Letters, vol. 117, no. 1, p. 011902, 2020

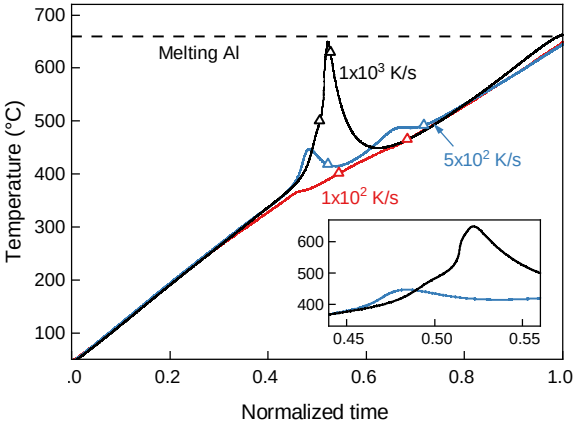

Figure 4.34: Shift from a two-stage reaction to a solid-state runaway reaction by increasing the heating rate from 100 $\mathrm{K\,s^{-1}}$ (red) to 10^3 $\mathrm{K\,s^{-1}}$ (black). The two peaks merge to one solid-state runaway peak. [126]

peak is observed. As it can be seen in the inset of Figure 4.34, there is a low-temperature shoulder between 400 °C and 500 °C, which indicates that the two-stage phase formation mechanism is still present. Within the exothermic peak, the temperature increases about 255 °C within 40 ms.

To prove the presence of a runaway reaction, a thermodynamic analysis of the $1 \cdot 10^3$-$\mathrm{K\,s^{-1}}$-experiment was performed. For this purpose, $\dot{Q}_{rct}$ and $\dot{Q}_{loss}$ was determined using the nanocalorimetry method described in Section 3.1.3. Figure 4.35 shows an increase of $\dot{Q}_{rct}$ in two stages starting at 375 °C. Applying the ignition criterion $d\dot{Q}_{rct}/dT > d\dot{Q}_{loss}/dT$ deduced in Section 4.2.2, ignition occurs at a temperature of 495 °C, right after the first stage. It should be noted, that even the more conservative ignition criterion $\dot{Q}_{rct} > \dot{Q}_{loss}$ is fulfilled at temperatures > 550 °C. This confirms the presence of a runaway reaction. The comparison of the critical power input density of $5.8 \cdot 10^4$ $\mathrm{W\,cm^{-3}}$ required for ignition show a good agreement to literature data [6, 18]. Since the maximum

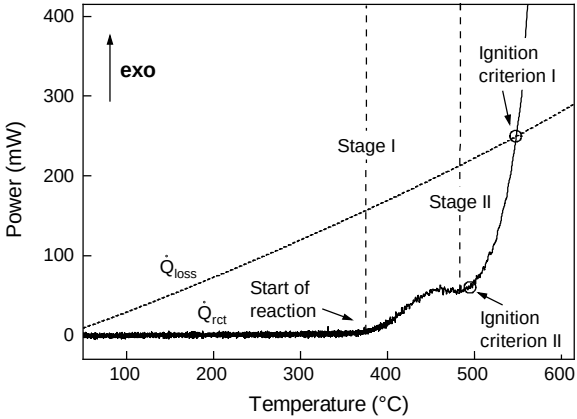

Figure 4.35: Thermodynamic characterisation of the solid state-state runaway reaction using nanocalorimetry. The heat losses $\dot{Q}_{loss}$ and the reaction power $\dot{Q}_{rct}$ are plotted versus the temperature. The ignition is reached at a temperature of 495 °C. [126]

temperature does not exceed 650 °C, all reactants and products are in the solid state (Al = 660°C, Al_3Ni = 845 °C and Ni = 1455°C). Although a solid flame was already observed in ball-milled powders [147–149], this is the first time this phenomenon is observed in metallic multilayers. This proves that the presence of a liquid phase, which is generally defined as necessary condition for a runaway reaction [150], is not required.

In the next step, the underlying mechanism which drives the solid-state runaway reaction should be identified. For this purpose, X-ray diffraction data is used. In Figure 4.36 (a), diffractograms after the first and the second phase formation stage are plotted. The exact time of recording of the diffractograms is marked in Figure 4.34. Independent from the heating rate, only one product phase, namely Al_3Ni, was identified. The presence of Al_3Ni is already verified after the first formation stage. However, the peak intensity increases significantly during the second stage. Besides the product phase, in all diffractograms, peaks of the reactants Al and Ni are present. The intensity of the reactants

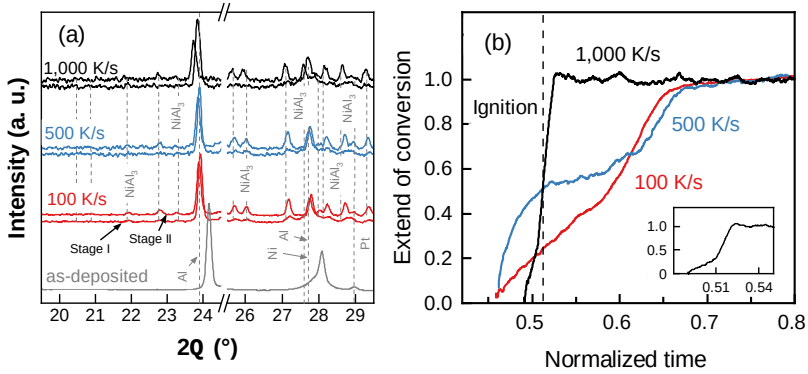

Figure 4.36: (a) X-ray diffractograms after the first and the second formation stage. The time of the recording is marked in Figure 4.34. After the first peak, Al_3Ni was identified. The peak intensity grows after the second stage. (b) The time-resolved extent of conversion is based on the integrated X-ray peak intensity of Al_3Ni. The phase formation kinetics changes with heating rate. The rapid succession of two formation stages of Al_3Ni leads to a solid-state runaway reaction. [126]

decreases with the increasing amount of Al_3Ni, which states that Al and Ni are consumed during the reaction. In the case of the $1 \cdot 10^3$-$K\,s^{-1}$-experiment, the diffractogram was recorded at the maximum temperature of the reaction. The Al peak at $2\theta = 23.86$ ° is permanently present. Since Al is the reactant with the lowest melting point, this corroborates that the reaction proceeds in a solid-state condition. It should be noted that the peak shift of Al and Ni between the as-deposited and the heated state is mainly caused by temperature-induced lattice expansion.

The time-resolved evolution of the integrated peak intensity of Al_3Ni plotted as extent of conversion α is shown in Figure 4.36 (b). The Al_3Ni peaks in the 2Θ range of 13.78°-18.51°, 21.93°, 22.81°, 25.73°, 26.05° and 30.19° were selected for integration. For comparability, the normalized values of the intensity and the normalized values of time t_{norm} were taken. In case of the 100 $K\,s^{-1}$ and $1 \cdot 10^3$ $K\,s^{-1}$ experiments the intensity increases continuously with time.

At $t_{norm} = 0.5$ ($\alpha = 0.32$) a change in the slope indicates a change in the phase growth rate. For the intermediate heating rate of 500 $K\,s^{-1}$, a plateau is present at $t_{norm} = 0.6$. This points towards a change of the phase growth kinetics with the heating rate. At 100 $K\,s^{-1}$, the heating rate is almost constant with no additional temperature peak. Hence, Al_3Ni grows continuously and the transition between the two growth stages is only indicated by a change in the slope. When the heating rate is increased, the separation between stage I and stage II is more pronounced. We contribute this to the temperature increase during stage I, which leads to a quick saturation of the interfacial phase growth. Further heating is required until the critical activation energy for phase growth perpendicular to the interface is reached. It can be estimated that for 100 $K\,s^{-1}$ and 500 $K\,s^{-1}$, stage I is completed at $0.5 < \alpha < 0.6$. This changes when the sample is heated with 1,000 $K\,s^{-1}$. The transition is lowered to $\alpha = 0.32$, which is an evidence for an incomplete stage I. Already at the beginning of stage I, enough reaction power is released to increase the temperature above 550 °C. This is well above the stage II initiation temperature of $\sim$ 450 °C, determined in the 100-$K\,s^{-1}$- and 500-$K\,s^{-1}$-experiment. Therefore, stage I is not completed before stage II is initiated. The rapid succession of both Al_3Ni reaction stages leads to a solid-state runaway reaction.

4.3.4 Early stages of the runaway reaction [4]

Next, the relevant mechanism for the initiation of the runaway reaction is investigated. The early stages of the reaction are of particular relevance since they define the characteristics of the consequent runaway reaction. Besides this, the initial stages of the runaway reaction are controlled by the external temperature profile. This is the fraction of the reaction which is externally controllable. Hence, a mechanism-based understanding of the initial stages is

fundamental for tailoring the runaway characteristics. *Neuhauser et al.* [4] [54] showed two experimental approaches: (i) Quenching using nanocalorimetry sensors in combination with XRD and electron microscopical investigations and (ii) subsequent pulsing in combination with XRD to investigate the initiation.

For the quenching experiments, Al/Ni multilayers with Λ = 166 nm were heated close to the ignition temperature and quenched using nanocalorimetry. Originally developed for the investigation of metallic glasses [84, 85, 87, 117–120], here nanocalorimetry is used for the first time to quench reactive materials. Because of the low thermal mass of the sensor, quenching rates of $\sim 2 \times 10^4$ $\mathrm{K\,s^{-1}}$ can be archived. This approach for quenching mimics hot plate experiments [6, 53]. However, nanocalorimetry has two major benefits compared to hot plate experiments: (i) accurate control of heating rate and temperature and (ii) uniform heating of the sample. This is mandatory for the characterisation of the mechanisms right before ignition. As shown in Section 4.2.2 the ignition temperature varies with heating rate and heating conditions. Hence, nanocalorimetry enables reproducible heating of the multilayer stack close to the physical ignition point. This enables the application of structural characterisation methods only a couple of degrees below the actual ignition temperature of the sample. After heating the multilayer stack to 412 °C, which is close to its ignition temperature, X-ray diffraction was performed. Figure 4.37 plots the *ex situ* synchrotron diffractograms before and after quenching. An acquisition time of 20 s was selected to increase the phase resolution. According to calculations, this reduces the minimum thickness of the detectable phase to $\sim$ 2.6 nm. The only peaks which are detectable are

[4] Excerpts from this chapter are published in: T. Neuhauser, G. Tinti, H. Leiste, N. Casati, M. Stüber, and K. Woll, "Analysis of the reaction runaway in Al/Ni multilayers with combined nanocalorimetry and time-resolved X-ray diffraction," Acta Materialia, vol. 195, pp. 579–587, 2020.

the elemental peaks of Al, Ni and Pt. No indication for the formation of intermetallic peaks of Al_9Ni_2, Al_3Ni or Al_3Ni_2 were found after heating. This is supported by analysing the integrated peak area of the Al peak at $\sim$ 24.3 °. There is no change in the peak area (as-deposited 1851 a.u. / quenched 1846 a.u.)[5] between the as-deposited state and after quenching. Hence, no Al was consumed for the formation of product phases. In case of the overlapping Ni (28.01 °) and Al (28.15 °) peak at $\sim$ 28.1 °, an increase of the intensity is observed. This is not expected since Al and Ni are elements, which are consumed during the reaction. The most likely explanation for the intensity increase are microstructural changes like a crystallisation of amorphous regimes. Interestingly it is reported that this phenomenon was also observed after annealing of Al/Ni multilayers [19]. It was concluded that the annihilation of lattice defects and an increase of the overall crystallinity are responsible for the intensity increase.

The previously described experiments reveal that interdiffusion dominates the reaction up to the ignition point. In order to investigate the stability range of the interdiffused state, multiple heating runs and subsequent XRD was performed. For this purpose, thermal pulses below the ignition temperature were conducted on Al/Ni samples with Λ = 83 nm. The pulse length was held constant at 100 ms and the temperature was gradually increased by 9 °C steps. The individual temperature pulses are shown in 4.38. With increasing peak temperature the heating rate increase from $3 \cdot 10^3$ Ks^{-1} up to $5 \cdot 10^3$ Ks^{-1}. All in all, 12 subsequent thermal pulses, numbered with the labels P1 to P12, were conducted. The experiments that are highlighted in colour were investigated in detail. It should be noted that the temperature increase per pulse is not evenly distributed. This can be traced back to the release of exothermic heat for certain pulses, which pushes the temperature above the predefined 9 °C.

[5] The detector used: Eiger 500k (self-developed 2D single-photon counting detector at the Paul Scherrer Institute)

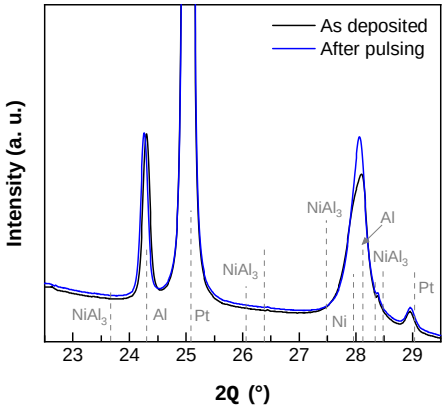

Figure 4.37: X-ray diffractograms of the as-deposited (black) and the quenched state (blue) of a $\Lambda = 166$ Al/Ni multilayer sample. By using nanocalorimetry, the sample was heated to 412 °C and quenched afterwards. The comparison shows no indications for intermetallic product phases formation Al_3Ni_2. In addition, there is no change of the integrated Al peak intensity at ~ 24.3 °. Hence, no Al was consumed during heating. [54].

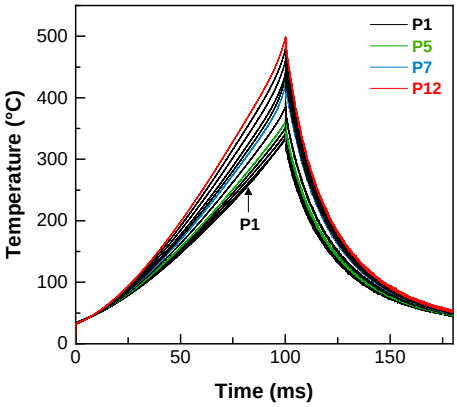

Figure 4.38: Multiple pulsing experiment on Al/Ni samples with $\Lambda = 83$ nm. The peak temperature is gradually increased by 9 °C steps, while the pulse length is held constant.

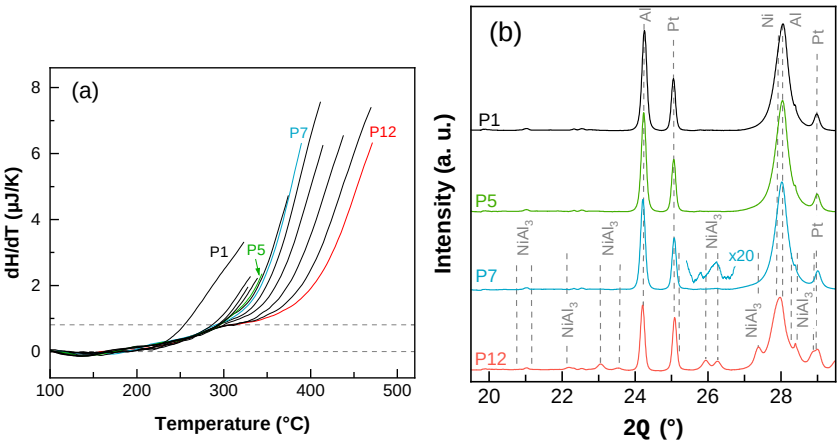

Figure 4.39: (a) Enthalpy release per temperature dH/dT for Al/Ni multilayers. The exothermic energy release is increased after P7. (b) Ex situ X-ray diffractograms of selected thermal pulses are depicted in colour. Up to pulse P5, there is no indication for product phase formation. Starting with P7 Al_3Ni is observed. [54]

To quantify the energy release during each thermal pulse the enthalpy change per temperature increment dH/dT calculated from equation 4.7 used. Here, dH/dT is preferential over $\dot{Q}_{rct}$, because the independence of the heating rate ensures the comparability of different experiments. Figure 4.39 (a) plots dH/dT vs. the temperature. Except for P1, up to 285 °C the dH/dT evolves similar for all pulses. Above 234 °C dH/dT continuously increases. When the temperature exceed 285 °C the slope of the dH/dT curve increases significantly. With each thermal pulse the onset the exothermic reaction is shifted incrementally to higher temperatures. The maximum values of dH/dT for P6 - P12 are about 4 times higher compared to P2- P5. The first pulses deviates from the successive P2 - P5 in the way, that a dH/dT increase is already observable at 234 °C. After P1 there is a significant shift dH/dT to higher temperatures.

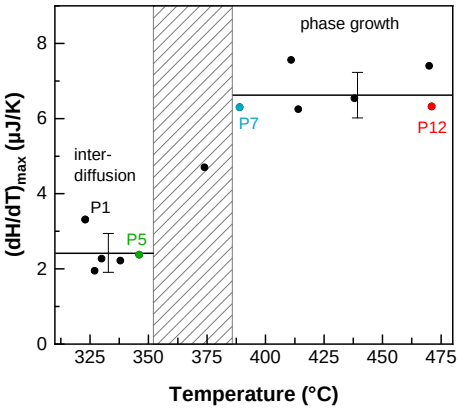

Figure 4.40: Plotting the maximum values of dH/dT from Figure 4.39 reveals two distinctive regimes. Up to P5, low values of dH/dT indicating interdiffusion, whereas the higher values starting at P7 can be correlated with Al_3Ni formation. [54]

The phase composition after selected thermal pulse was analysed via a long-acquisition (t = 20 s) XRD scan. The diffractograms of selected pulses are shown in Figure 4.39 (b). Up to P5, no intermetallic phases are detectable. Only the elemental peaks of Al, Ni and Pt are present. Starting with P7, there are first indications for the formation of Al_3Ni. With an increasing number of pulses, the intensity of the Al_3Ni peak increases. Simultaneously, the decreasing peak intensity of the Al peak indicates the consumption of reactants. By correlating the enthalpy change and the X-ray diffractograms, it becomes evident that the increase of reaction rate coincidence with the formation of intermetallic phases. This becomes even clearer when $(dH/dT)_{max}$ is plotted versus the number of pulses. Figure 4.40 shows two distinctive regimes, where up to P5 low reaction rates are observed and starting with P7 $(dH/dT)_{max}$ significantly increase. In combination with the XRD results, this allows us to conclude that up to 342 °C interdiffusion dominating the reaction mechanism. Grain boundaries perpendicular to the Al/Ni interfaces are most likely the preferred pathways for diffusing Ni atoms. The formation of a solid solution

proceeds up to P5. Since the enthalpy of mixing is usually much lower than the enthalpy of phase formation, the values for colo$(dH/dT)_{max}$ are lower. Taking the composition gradient theory outlined in Section 2.4.1 into account, it can be assumed that the composition gradient is above a critical limit, which suppresses nucleation of Al_3Ni. Since exothermic heat is released, but XRD gives no evidence for phase formation, we conclude that interdiffusion is the dominant mechanism up to the ignition temperature (compare Figure 4.37). Simultaneously with the beginning of the second plateau, the formation of the Al_3Ni phase is observed. Further intermixing leads to the flattening of the composition gradient and enables the nucleation of the product phase. Therefore, phase formation dominates the reaction at temperatures above 389 °C. Since the enthalpy of formation is high for phase formation (see Table 2.1), also high values for $(dH/dT)_{max}$ are observed. With every thermal pulse, the thickness of Al_3Ni increases and, therefore, the thermodynamic barrier for Ni diffusion through the product layer. Higher temperatures (= higher thermal energy) are required for the Ni atoms to overcome this barrier, which shifts the onset of the energy release to higher values.

Interestingly the microstructural changes occurring during pulsing have a direct impact on the ignition temperature. Note, that in Figure 4.38 the peak temperature of 499 °C of P12 is well above the ignition temperature of the as-deposited sample with 367 °C. This implies that the ignition temperature depends on the thermal history of the sample. The source for exothermic energy release, namely interdiffusion and phase formation, is shifted to higher temperatures. Consequently, the ignition point which relies on the energy release is shifted to higher temperatures. This is comparable to the annealing experiments shown in Figure 4.31. These observations point to the relevance of the local microstructure at the interface for the reaction characteristics.

4.3.5 Mechanisms of the runaway reactions

Within this study, runaway reactions were initiated under various experimental conditions. All runaway reactions observed can be classified into three types: (i) liquid-state runaway reactions, (ii) liquid-state runaway reactions with prior phase formation, (iii) solid-state runaway reaction. Based on the experimental findings for every type the underlying mechanism is derived in the following:

Liquid-state runaway reaction (LRR)

The majority of the runaway reaction can be assigned to the liquid-state runaway reactions. Typically, this type is observed in metallic multilayers with a high enthalpy of formation in combination with high diffusivity. This includes multilayer samples with a composition close to the corresponding compound phase (see Figure 4.17), high Al/Ni interface density (see Figure 4.14) and high ratio of reactive material to inert material (see Figure 4.33). The characteristic feature of this reaction is the melting of one constituent before the product phase is formed. According to the experimental findings shown in Figure 4.27 *Neuhauser et al.* [54] derived a mechanism for the solid-state runaway reaction. The reaction can be subdivided into five individual stages, which are illustrated in Figure 4.41. The phase sequence can be summarized as follows:

$$\begin{aligned} Al + Ni \rightarrow Al(l) + Ni(s) &\rightarrow Al_3Ni_2 + Al(l) + Ni(s) \\ &\rightarrow Al_3Ni_2 \rightarrow Al_3Ni_2 + Al_3Ni \end{aligned} \tag{4.9}$$

For stages I and II, the experimental findings presented in Section 4.3.4 suggest that the liquid-state runaway reaction is initiated by interdiffusion between Ni and Al. The formation of an intermixed layer releases exothermic heat and leads to an increase in the sample temperature. This is indicated by stage I and stage II in Figure 4.27. Complementary studies at slow heating rates [50]

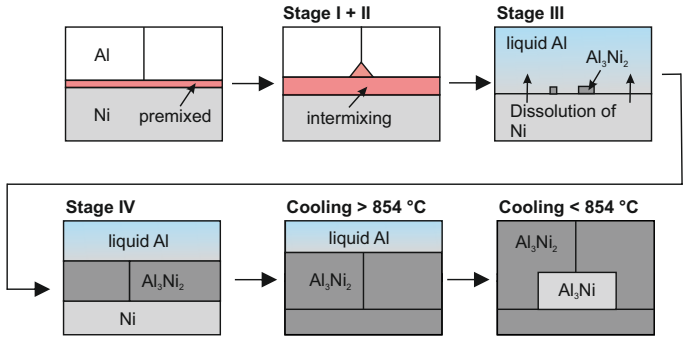

Figure 4.41: Illustration of the mechanism in a liquid-state runaway reaction. The main steps are the formation of an intermixed layer, melting of Al, formation of Al_3Ni_2 and precipitation Al_3Ni during cooling.

and fast heating rates [7, 20] confirm that intermixing is the dominating mechanism. Stage I and II differ in reaction rates. Whereas in stage I, there is no significant influence on the temperature, in stage II, the major temperature increase is observable. This is related to the activation of diffusion processes. Since diffusion is temperature dependent, the rise in temperature leads to an increasing degree of intermixing and, therefore, to an enhanced exothermic heat release. This may be accelerated by the onset of Al melting at the very end of stage II, leading to a heating rate peak.

Stage III is dominated by the solid-to-liquid transition of Al. This material transition leads to a decrease in the heating rate (see Figure 4.27). This can be attributed to two mechanisms running in parallel: (i) endothermic melting of Al and (ii) exothermic intermixing of liquid Al and solid Ni. The diffusivity of Ni in the liquid Al ($D^0 = 10^{-8} - 10^{-9}$ m^2 s^{-1} [151]) is significantly enhanced

compared to the solid-state ($D^0 = 10^{-12} - 10^{-16}$ m^2 s^{-1} [151]). Both contributions are not fully balanced. With the onset of melting, an endothermic process is added to heat balance, which lowers the heating rate. It is unlikely that heat losses have a major contribution to the heating rate signal at this point. With the ignition of the sample the reaction power overcompensated the heat losses already at a very early stage of the reaction. The observations of stage III agree well with the so-called exothermic dissolution process proposed by *Rogachev et al.* [150, 152]. The dissolution of Ni into liquid Al is the driving mechanism for the Al/Ni runaway reaction. This process leads to a significant release of exothermic heat and is responsible for the major part of the temperature increase. The exothermic dissolution theory assumes phase formation during the late stages of the reactions. This is confirmed by findings in this study. Al_3Ni or Al_3Ni_2 is formed to a minor extent at the end of stage III.

In stage IV, the major part of the Al_3Ni_2 compound phase is formed. As shown in Figure 4.28, this takes place well after the peak temperature has been exceeded. Hence, significant parts of the phase formation do not contribute to the temperature increase in liquid-state runaway reactions. Such a post-reaction phase formation process was also observed for self-propagating reactions in Al/Ni multilayers [150, 152, 153]. However, due to the lack of *in situ* investigations, the influence of quenching on phase formation could not be answered unambiguously. This study proves that the intermetallic phase is formed in the presence of liquid Al and solid Ni after the high-temperature reaction. Interestingly, phase formation during cooling was also observed for macroscopic reaction couples between liquid Al and solid Ni [154, 155]. The formation of intermetallic phases at the Al/Ni interface was only observed when the system was cooled down. Holding the reaction couple at a constant temperature did not result in the formation of compound phases. This points to the thermodynamic driving force during cooling, which is required for the nucleation of the product phase.

The fact that phase formation does not significantly contribute to the runaway is unexpected since, from a purely thermodynamic point of view, the formation of Al_3Ni_2 is a highly exothermic and thermodynamically favourable process. We propose two explanatory approaches for this phenomenon. Assuming that Al_3Ni_2 is formed as a continuous layer at the liquid Al/solid Ni interface, the dissolution process would be slowed down due to the additional diffusion barrier. Hence, less exothermic reaction power is released. An alternative explanation is the reduction of the total enthalpy of formation of Al_3Ni_2 due to prior intermixing. In the course of the dissolution process in stage III, liquid Al is enriched with Ni. This leads to the release of the enthalpy of intermixing. The enthalpy of intermixing versus the enthalpy of phase formation is plotted in Figure 2.4. At an atomic fraction of 0.75 Al, approximately 80 % of the total enthalpy is already released by intermixing. Only 20 % are available for the Al_3Ni_2 formation. We assume that both explanatory approaches are valid. The interaction between both contributions result in the decrease of the heating rate signal depicted in Figure 4.28.

In case of liquid-state runaway reaction shown in Figure 4.26, it was found that Al_3Ni_2 is the first phase which is formed. This seems to contradict nanocalorimetry studies which identified Al_3Ni as the first phase [7, 20] and self-propagating reactions fronts which identified NiAl as the first phase [23, 78]. Considering only thermodynamic aspects Ni-rich intermetallic compounds are preferred. Comparing the enthalpy of formation, the sequence of formation is NiAl ($\Delta H_f = -59\ \mathrm{kJ\,g^{-1}at}$) , Al_3Ni_2 ($\Delta H_f = -57\ \mathrm{kJ\,g^{-1}at}$) and finally Al_3Ni ($\Delta H_f = -38\ \mathrm{kJ\,g^{-1}at}$) [74]. However, this requires a fast mixing of the constituents, which is only possible in the liquid-state. In this case, the type of the first phase is defined by the composition and temperature given by the phase diagram. Since the reaction temperature in this study is just in the stability region of Al_3Ni_2, this type of phase is formed first. In contrast to solid-state

reactions, intermixing is limited [7, 20]. In the solid-state, the material transport across the Al/Ni interface favours Al-rich compounds (see Section 2.4).

With the ending of Stage IV, the phase transition during the runaway reaction is not completed. The amount Al_3Ni_2 further increases, but with a decreasing growth rate (see Figure 4.28). This is attributed to the rising proportion of the product phase formed at the Al/Ni interface. This additional layer impedes diffusion and therefore, the growth rate of Al_3Ni_2 decreases. Below the peritectic temperature, Al_3Ni starts to form whereas Al_3Ni_2 is consumed. The sample tends towards the equilibrium condition. Finally, the sample is in a two-phase state comprising Al_3Ni_2 and Al_3Ni. It cannot be ruled out that a deviation of the target composition of 25 at.% Ni is the reason for Al_3Ni_2 in the post-reacted state of the sample. However, the kinetics of the phase transition must be considered as well. Fast cooling of the sample may impede a complete transformation of Al_3Ni_2 into Al_3Ni.

Liquid-state runaway reaction with compound layer (LRRCL)

The LRRCL is closely related to the purely liquid-state runaway reaction. The major difference is the initial state of the multilayer stack before ignition. In the case of a LRRCL, the multilayer stack was exposed to a pre-reaction temperature treatment prior to ignition. This temperature treatment could either be an isothermal annealing procedure as shown in Figure 4.31 or sequential thermal pulsing as depicted in Figure 4.38. However, besides these two exemplary cases, there are also more complex thermal treatments conceivable. The temperature treatment of the multilayer stack leads to the formation of a compound layer, which plays an essential role in the subsequent runaway reaction. The individual steps of a LRRCL are schematically shown in Figure 4.42.

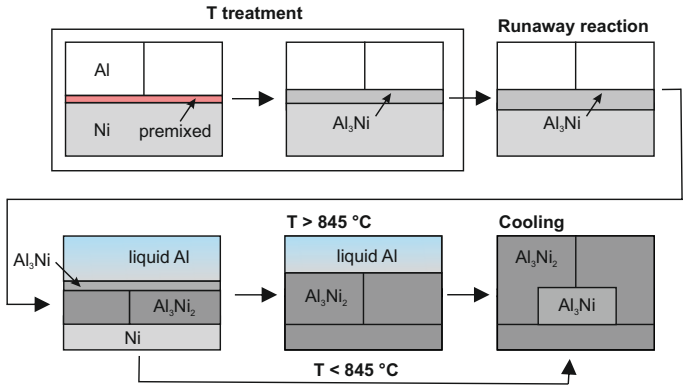

Figure 4.42: Illustration of the mechanism in a liquid-state runaway reaction with reactant layer. In the course of the pre-reaction thermal treatment Al_3, Ni is formed. The consequent runaway reaction is driven by phase growth and the nucleation of Al_3Ni_2. Depending on the peak temperature, the sample turns directly into the Al_3Ni_2/Al_3Ni state or into an intermediate step where only Al_3Ni_2 is present.

The phase sequence can be summarized as follows:

$$\begin{aligned} Al + Ni + Al_3Ni \rightarrow Al(l) + Ni(s) + Al_3Ni_2 \\ \rightarrow Al_3Ni_2 \rightarrow Al_3Ni_2 + Al_3Ni \end{aligned} \tag{4.10}$$

In the first step, the multilayer stack is exposed to temperature, which leads to the formation of the Al-rich compound Al_3Ni at the interface. This process is equivalent to the phase formation mechanism observed in the slow-heating-rate- or constant-temperature-experiment discussed in Section 4.1. Since the Al_9Ni_2 and Al_3Ni formation is already observed during annealing, the initial state of the sample is not a binary system but a ternary system consisting of Al/Al_3Ni/Ni. This affects the initiation of the runaway reaction. As shown in Figure 4.32 the reaction is initiated by Al_3Ni growth. This is different to

LRR, where ignition and the runaway reaction is driven by the formation of an intermixed layer. The reactant layer hinders Ni from diffusing into Al. This impacts the reaction kinetic: first, the heating rate during initiation is lower and second, the onset of the runaway reaction is shifted to a higher temperature when the annealing time is increased. With the thickening of the compound layer, higher temperatures are required for Ni and Al to overcome this thermodynamic barrier. Depending on the peak temperature, the sample can either be directly transformed into Al_3Ni and Al_3Ni_2 ($T_{max} < 845$ °C) or an additional intermediate step with liquid Al and solid Al_3Ni_2 ($T_{max} > 845$ °C) is prior to the formation of the final product state. Generally, the peak temperatures of the reaction are lower compared to LRR (see Figure 4.32). The intermetallic phases formed during annealing reduce the total amount of the enthalpy of formation. Less exothermic energy is released during the reaction, which results in a reduction of the peak temperature. This is in good agreement with the investigations of self-propagating reaction fronts after annealing [8]. It was found that the heat of formation and the reaction velocity is reduced with increasing annealing time. This is attributed to the thickness of the intermixed region.

Solid-state runaway reaction (SRR)

For the solid-state runaway reaction, the temperature must not exceed the melting temperature of one constituent. However, the reaction rate and the exothermic energy release have to be high enough to ignite the multilayers stack. For this reason, there is only a small parameter window for this type of reaction. Under the conditions in this study, the solid-state runaway reaction was observed only for 10 at.% Ni and a heating rate of $1 \cdot 10^3$ Ks^{-1} (see Section 4.3.3). Based on the findings, *Neuhauser et al.* [126] derived a mechanism for the solid-state reaction. The most important steps are depicted in Figure 4.43.

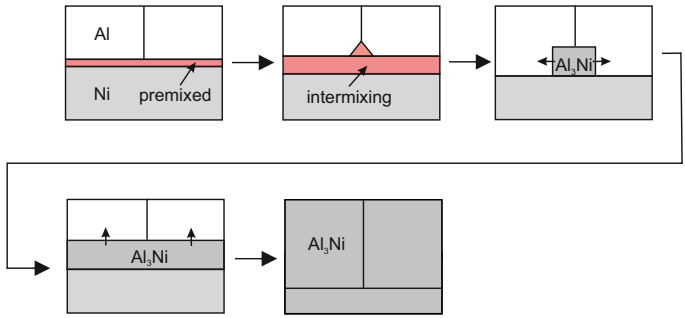

Figure 4.43: Mechanism of the solid-state runaway reaction. After intermixing, Al_3Ni is formed in a two-stage process. The rapid succession of growth parallel and perpendicular to the Al/Ni interface leading to ignition. During the reaction, the temperature remains below the melting point of all constituents.

The phase sequence can be summarized as follows:

$$Al + Ni \rightarrow Al + Ni + Al_3Ni \rightarrow Al_3Ni + Ni \tag{4.11}$$

Parallel to the liquid-state reactions, solid-state reactions are initiated by Ni atoms diffusing into the Al layer. However, the lower reaction rate in the first step does not lead to the ignition of the sample. A major temperature increase takes place in connection with the formation of Al_3Ni. The formation proceeds in two growth stages: (i) interfacial growth of Al_3Ni (ii) growth perpendicular to the Al/Ni interface. This process is comparable to the two-step formation proposed by *Coffey et al.* [70]. This mechanism was also observed in the case of the low heating rate experiments shown in Section 4.1.2. In the first stage, a compound layer is formed at the Al/Ni interface. In the second stage,

the reactant layer grows perpendicular to the interface. In contrast to the two-stage formation mechanism at low heating rates, the second stage is initiated before the first stage is completed at high heating rates. Figure 4.34 demonstrates that the exothermic heat of the first stage is high enough to activate the second stage. The rapid succession of both reaction stages leads to a solid-state runaway reaction. In the SRR shown in Section 4.3.3, Al_3Ni is formed. According to theoretical considerations by *Pretorius et al.* [156], it is a reasonable assumption that the phase sequence in SRR follows the sequence predicted for slow heating solid-state reactions, which favours Al-rich compounds.

5 Summary

The phase formation behaviour of Al/Ni multilayers was investigated in a heating rate regime between 10 and 10^6 K/s. For this purpose, an *in situ* method was developed, which combines chip-based nanocalorimetry with synchrotron X-ray diffraction. For the first time, this methodical approach was applied to reactive multilayers. It could be demonstrated that this setup enables structural characterization with a temporal resolution up to 15 µs. The main findings of this study can be summarized as follows:

(1) For **heating rates below 500 Ks^{-1}**, a solid-state reaction was observed. A critical heating rate of 100 Ks^{-1} was identified where the metastable Al_9Ni_2 phase is replace by Al_3Ni as the first phase formed.

(2) Based on time-resolved X-ray diffraction data, a **kinetic analysis** of the phase growth was performed. Both Al_9Ni_2 and Al_3Ni showed a linear growth behaviour at the beginning. The activation energy of Al_9Ni_2 of 1.06 ± 0.12 eV suggests interdiffusion and redistribution as the rate-limiting processes. With further reaction progression, the growth behaviour of Al_3Ni becomes diffusion dominated.

(3) Nanocalorimetry was used to **determine the ignition temperatures** of Al/Ni multilayers. Numerous parameters which influence the ignition temperature, including heating rate, multilayer geometry, heat capacity and thermal history, were identified. Based on the results, a new criterion for the ignition of reactive multilayers is proposed. The quantification of the ignition point enabled the differentiation between solid-state and runaway reactions depending on the sample geometry.

(4) The **runaway reaction** is initiated when ignition temperature is exceeded. In this study, three types of runaway reactions could be identified: liquid-state runaway reactions, liquid-state runaway reactions with compound layer and solid-state runaway reactions.

- In the case of **liquid-state runaway reactions** it was found that the diffusion of Ni into Al is the dominating mechanism for the initiation of the runaway reaction. Phase formation was observed not until the melting of Al. Instead, the dissolution of Ni into liquid Al is suggested as the dominant mechanism. The majority of the Al_3Ni_2 phase formation was observed during cooling.
- By annealing, a compound phase was introduced at the Al/Ni interface prior to ignition. The investigations of **liquid-state runaway reactions with compound layers** showed that the growth of the Al_3Ni phase initiates the runaway reaction. Thickening of Al_3Ni and formation of Al_3Ni_2 dominate the further course of the reaction.
- For the first time, a **solid-state runaway reaction** was observed in reactive multilayers. The rapid succession of two Al_3Ni formation stages comprising phase growth along and perpendicular to the interface could be identified as the underlying mechanism.

In summary, the influence of the heating rate on the phase selection could be verified. Generally, it can be stated that the formation of Ni-rich compound phases is preferred at high heating rates due to the transition to liquid-state reactions.

Bibliography

[1] J. H. Perepezko, "The hotter the engine, the better," *Science*, vol. 326, no. 5956, pp. 1068–1069, 2009.

[2] B. Lojek, *History of semiconductor engineering*, 1st ed., Berlin: Springer, 2007.

[3] H. Gleiter, "Microstrucutre," in *Physical Metallurgy*, 4th ed., R. W. Cahn and P. Haasen, Eds. Amsterdam: Elsevier Ltd., 1996, pp. 843–942.

[4] L. Spieß, G. Teichert, R. Schwarzer, H. Behnken, and C. Genzel, *Moderne Röntgenbeugung*, 2nd ed., Wiesbaden: Vieweg+Teubner, 2009.

[5] D. P. Adams, "Reactive multilayers fabricated by vapor deposition: A critical review," *Thin Solid Films*, vol. 576, pp. 98–128, 2015.

[6] G. M. Fritz, S. J. Spey, M. D. Grapes, and T. P. Weihs, "Thresholds for igniting exothermic reactions in Al/Ni multilayers using pulses of electrical, mechanical, and thermal energy," *Journal of Applied Physics*, vol. 113, no. 1, p. 014901, 2013.

[7] M. D. Grapes, T. P. Weihs, M. K. Santala, H. Campbell, and D. A. LaVan, "A detailed study of the Al 3 Ni formation reaction using nanocalorimetry," *Thermochimica Acta*, vol. 658, pp. 72–83, 2017.

[8] A. J. Gavens, D. Van Heerden, A. B. Mann, M. E. Reiss, and T. P. Weihs, "Effect of intermixing on self-propagating exothermic reactions

in Al/Ni nanolaminate foils," *Journal of Applied Physics*, vol. 87, no. 3, pp. 1255–1263, 2000.

[9] R. Knepper, M. R. Snyder, G. Fritz, K. Fisher, O. M. Knio, and T. P. Weihs, "Effect of varying bilayer spacing distribution on reaction heat and velocity in reactive Al/Ni multilayers," *Journal of Applied Physics*, vol. 105, no. 8, p. 083504, 2009.

[10] A. S. Rogachev, S. G. Vadchenko, F. Baras, O. Politano, S. Rouvimov, N. V. Sachkova, M. D. Grapes, T. P. Weihs, and A. S. Mukasyan, "Combustion in reactive multilayer Ni/Al nanofoils: Experiments and molecular dynamic simulation," *Combustion and Flame*, vol. 166, pp. 158–169, 2016.

[11] P. Swaminathan, M. D. Grapes, K. Woll, S. C. Barron, D. A. Lavan, and T. P. Weihs, "Studying exothermic reactions in the Ni-Al system at rapid heating rates using a nanocalorimeter," *Journal of Applied Physics*, vol. 113, no. 14, p. 143509, 2013.

[12] A. S. Mukasyan and C. E. Shuck, "Kinetics of SHS reactions: A review," *International Journal of Self-Propagating High-Temperature Synthesis*, vol. 26, no. 3, pp. 145–165, 2017.

[13] E. Ma, C. V. Thompson, L. A. Clevenger, and K. N. Tu, "Self-propagating explosive reactions in Al/Ni multilayer thin films," *Applied Physics Letters*, vol. 57, no. 12, pp. 1262–1264, 1990.

[14] A. S. Edelstein, R. K. Everett, G. Y. Richardson, S. B. Qadri, E. I. Altman, J. C. Foley, and J. H. Perepezko, "Intermetallic phase formation during annealing of Al/Ni multilayers," *Journal of Applied Physics*, vol. 76, no. 12, pp. 7850–7859, 1994.

[15] C. Michaelsen, K. Barmak, and T. P. Weihs, "Investigating the thermodynamics and kinetics of thin lm reactions by differential

scanning calorimetry," *Journal of Physics D: Applied Physics*, vol. 30, pp. 3167–3186, 1997.

[16] A. Ustinov, L. Olikhovska, T. Melnichenko, and A. Shyshkin, "Effect of overall composition on thermally induced solid-state transformations in thick EB PVD Al/Ni multilayers," *Surface and Coatings Technology*, vol. 202, no. 16, pp. 3832–3838, 2008.

[17] Ł. Maj and J. Morgiel, "In-situ transmission electron microscopy observations of nucleation and growth of intermetallic phases during reaction of Ni(V)/Al multilayers," *Thin Solid Films*, vol. 621, pp. 165–170, 2017.

[18] G. M. Fritz, J. A. Grzyb, O. M. Knio, M. D. Grapes, and T. P. Weihs, "Characterizing solid-state ignition of runaway chemical reactions in Ni-Al nanoscale multilayers under uniform heating," *Journal of Applied Physics*, vol. 118, no. 13, p. 135101, 2015.

[19] K. V. Manukyan, J. M. Pauls, C. E. Shuck, S. Rouvimov, A. S. Mukasyan, K. Nazaretyan, H. Chatilyan, and S. Kharatyan, "Kinetics and Mechanism of Ignition in Reactive Al/Ni Nanostructured Materials," *The Journal of Physical Chemistry C*, vol. 122, p. 27082−27092, 2018.

[20] M. D. Grapes, T. Lagrange, L. H. Friedman, B. W. Reed, G. H. Campbell, T. P. Weihs, and D. A. Lavan, "Combining nanocalorimetry and dynamic transmission electron microscopy for in situ characterization of materials processes under rapid heating and cooling," *Review of Scientific Instruments*, vol. 85, no. 8, p. 084902, 2014.

[21] F. Yi and D. A. LaVan, "Nanocalorimetry: Exploring materials faster and smaller," *Applied Physics Reviews*, vol. 6, no. 3, p. 031302, 2019.

[22] J. C. Trenkle, L. J. Koerner, M. W. Tate, S. M. Gruner, T. P. Weihs, and T. C. Hufnagel, "Phase transformations during rapid heating of Al/Ni multilayer foils," *Applied Physics Letters*, vol. 93, no. 8, pp. 1–4, 2008.

[23] K. Fadenberger, I. E. Gunduz, C. Tsotsos, M. Kokonou, S. Gravani, S. Brandstetter, A. Bergamaschi, B. Schmitt, P. H. Mayrhofer, C. C. Doumanidis, and C. Rebholz, "In situ observation of rapid reactions in nanoscale Ni-Al multilayer foils using synchrotron radiation," *Applied Physics Letters*, vol. 97, no. 14, pp. 1–4, 2010.

[24] A. B. Mann, A. J. Gavens, M. E. Reiss, D. Van Heerden, G. Bao, and T. P. Weihs, "Modeling and characterizing the propagation velocity of exothermic reactions in multilayer foils," *Journal of Applied Physics*, vol. 82, no. 3, pp. 1178–1188, 1997.

[25] K. V. Manukyan, W. Tan, R. J. Deboer, E. J. Stech, A. Aprahamian, M. Wiescher, S. Rouvimov, K. R. Overdeep, C. E. Shuck, T. P. Weihs, and A. S. Mukasyan, "Irradiation-enhanced reactivity of multilayer Al/Ni nanomaterials," *ACS Applied Materials and Interfaces*, vol. 7, no. 21, pp. 11 272–11 279, 2015.

[26] R. G. Xu, M. L. Falk, and T. P. Weihs, "Interdiffusion of Ni-Al multilayers: A continuum and molecular dynamics study," *Journal of Applied Physics*, vol. 114, no. 16, 2013.

[27] E. Ma, M. A. Nicolet, and M. Nathan, "NiAl3 formation in Al/Ni thin-film bilayers with and without contamination," *Journal of Applied Physics*, vol. 65, no. 7, pp. 2703–2710, 1989.

[28] T. Jeske, M. Seibt, and G. Schmitz, "Microstructural influence on the early stages of interreaction of Al/Ni-investigated by TAP and HREM," *Materials Science and Engineering: A*, vol. 353, pp. 105–111, 2003.

[29] C. Michaelsen and K. Barmak, “Calorimetric determination of NiAl3-growth kinetics in sputter-deposited Ni/Al diffusion couples,” *Journal of Alloys and Compounds*, vol. 257, pp. 211–214, 1997.

[30] A. I. Ustinov and S. A. Demchenkov, “Influence of metastable Al9Ni2 phase on the sequence of phase transformations initiated by heating of Al/Ni multilayer foils produced by EBPVD method,” *Intermetallics*, vol. 84, pp. 82–91, 2017.

[31] C. Michaelsen, G. Lucadamo, and K. Barmak, “The early stages of solid-state reactions in Ni/Al multilayer films,” *Journal of Applied Physics*, vol. 80, no. 12, pp. 6689–6698, 1996.

[32] P. J. Desré and A. R. Yavari, “Suppression of crystal nucleation in amorphous layers with sharp concentration gradients,” *Physical Review Letters*, vol. 64, no. 13, pp. 1533–1536, 1990.

[33] P. J. Desré, “Effect of sharp concentration gradients on the stability of a two-component amorphous layer obtained by solid state reaction,” *Acta Metallurgica et Materialia*, vol. 39, no. 10, pp. 2309–2315, 1991.

[34] T. P. Weihs, O. Knio, M. Reiss, and D. van Heerden, “Composite reactive mulitlayer foil,” pp. 6, US Patent 6,863,992 B2, 2005.

[35] C. Suryanarayana, J. J. Moore, and R. P. Radtke, “Novel methods of brazing dissimilar materials,” *Advanced materials & processes*, vol. 159, no. 3, pp. 29–31, 2001.

[36] M. Ding, F. Krieger, J. Swank, J. Poret, C. McMullan, and G. Chen, “Use of NanoFoil as a New Heat Source in Thermal Batteries,” *Proc. 43 th Power Sources Conference*, vol. 615, p. 8, 2008.

[37] C. J. Morris, B. Mary, E. Zakar, S. Barron, G. Fritz, O. Knio, T. P. Weihs, R. Hodgin, P. Wilkins, and C. May, “Rapid initiation of

reactions in Al/Ni multilayers with nanoscale layering," *Journal of Physics and Chemistry of Solids*, vol. 71, no. 2, pp. 84–89, 2010.

[38] G. M. Fritz, H. Joress, and T. P. Weihs, "Enabling and controlling slow reaction velocities in low-density compacts of multilayer reactive particles," *Combustion and Flame*, vol. 158, no. 6, pp. 1084–1088, 2011.

[39] S. Danzi, V. Schnabel, J. Gabl, A. Sologubenko, H. Galinski, and R. Spolenak, "Rapid On-Chip Healing of Metal Thin Films," *Advanced Materials Technologies*, vol. 4, no. 3, p. 1800468, 2019.

[40] Z. A. Munir, "Reaction synthesis processes: mechanisms and characteristics," *Metallurgical Transactions A*, vol. 23, no. 1, pp. 7–13, 1992.

[41] J. Subrahmanyam and M. Vijayakumar, "Self-propagating high-temperature synthesis," *Journal of Materials Science*, vol. 27, no. 23, pp. 6249–6273, 1992.

[42] J. J. Moore and H. J. Feng, "Combustion synthesis of advanced materials: Part I. Reaction parameters," *Progress in Materials Science*, vol. 39, no. 4-5, pp. 243–273, 1995.

[43] J. J. Moore and H. J. Feng, "Combustion synthesis of advanced materials: Part II. Classification, applications and modelling," *Progress in Materials Science*, vol. 39, no. 4-5, pp. 275–316, 1995.

[44] C. R. Bowen and B. Derby, "Finite-difference modelling of self-propagating high-temperature synthesis of materials," *Acta Metallurgica et Materialia*, vol. 43, no. 10, pp. 3903–3913, 1995.

[45] K. Morsi, "Review: Reaction synthesis processing of Ni-Al intermetallic materials," *Materials Science and Engineering A*, vol. 299, no. 1-2, pp. 1–15, 2001.

[46] P. Nash, M. Singleton, and J. Murray, *Phase diagrams of binary nickel alloys*. Ohio,USA: ASM International, 1991.

[47] L. Bendersky, "Orientation Relationship between Precipitated AI9(Fe, Ni)2 Phase and a-Aluminum," *Metallurgical Transactions A*, vol. 16A, no. 031, pp. 683–686, 1985.

[48] K. Barmak, C. Michaelsen, and G. Lucadamo, "Reactive phase formation in sputter-deposited Ni/Al multilayer thin films," *Journal of Materials Research*, vol. 12, no. 1, pp. 133–146., 1995.

[49] D. van Heerden, A. J. Gavens, S. Jayaraman, and T. P. Weihs, "Metastable phase formation and microstructural evolution during self-propagating reactions in Al/Ni and Al/Monel multilayer," *MRS Proceedings*, vol. 481, pp. 533–538, 1998.

[50] K. J. Blobaum, D. V. Heerden, A. J. Gavens, and T. P. Weihs, "Al/Ni formation reactions: characterization of the metastable Al9Ni2 phase and analysis of its formation," *Acta Materialia*, vol. 51, pp. 3871–3884, 2003.

[51] T. P. Weihs, "Self-propagating reactions in multilayer materials," in *Handbook of Thin Film Process Technology*, D. I. Glocker and S. I. Shah, Eds. Bristol: IOP Publishig Ltd., 1998.

[52] I. Glassman, A. R. Yetter, and G. N. Glumac, *Combustion*, 5th ed. Amsterdam: Elsevier, 2015.

[53] C. Pauly, K. Woll, B. Bax, and F. Mücklich, "The role of transitional phase formation during ignition of reactive multilayers," *Applied Physics Letters*, vol. 107, no. 11, p. 113104, 2015.

[54] T. Neuhauser, G. Tinti, H. Leiste, N. Casati, M. Stüber, and K. Woll, "Analysis of the reaction runaway in Al/Ni multilayers with combined

nanocalorimetry and time-resolved X-ray diffraction," *Acta Materialia*, vol. 195, pp. 579–587, 2020.

[55] N. N. Semenov, "Chemical kinetics and chain reactions," *Oxford University Press*, 1935.

[56] R. J. Highmore, J. E. Evetts, A. L. Greer, and R. E. Somekh, "Differential scanning calorimetry study of solid-state amorphization in multilayer thin-film Ni/Zr," *Applied Physics Letters*, vol. 50, no. 10, pp. 566–568, 1987.

[57] M. Atzmon, "The effect of interfacial diffusion barriers on the ignition of self-sustained reactions in metal-metal diffusion couples," *Metallurgical Transactions A*, vol. 23, no. 1, pp. 49–53, 1992.

[58] R. E. Reed-Hill and R. Abbaschian, *Physical metallurgy principles*, 3rd ed., Boston: PWS Publishing Company, 1991.

[59] A. L. Greer and K. Kelton, *Nucleation in Condensed Matter : Applications in Materials and Biology*, 15th ed., Amsterdam: Elsevier Science & Technology, 2010.

[60] A. M. Gusak, "No title available," *Ukrainian Journal of Physics*, vol. 35, p. 725, 1990.

[61] F. Hodaj and P. J. Desré, "Effect of a sharp gradient of concentration on nucleation of intermetallics at interfaces between polycrystalline layers," *Acta Materialia*, vol. 44, no. 11, pp. 4485–4490, 1996.

[62] C. V. Thompson, "On the role of diffusion in phase selection during reactions at interfaces," *Journal of Materials Research*, vol. 7, no. 2, pp. 367–373, 1992.

[63] D. Gupta, "Special Aspects of Diffusion in Metallic Thin Films." *Materials Research Society Symposia Proceedings*, vol. 47, pp. 11–26, 1985.

[64] H. Mehrer, P. Fulde, and K. von Klitzing, *Diffusion in Solids*, 1st ed., Berlin: Springer, 2009.

[65] N. Gjostein, *Short Circuit Diffusion, In: Diffusion*. Ohio: American Society for Metals, 1973.

[66] V. Vovk, G. Schmitz, and R. Kirchheim, "Nucleation of product phase in reactive diffusion of Al/Co," *Physical Review B - Condensed Matter and Materials Physics*, vol. 69, no. 10, pp. 1–9, 2004.

[67] E. Ma, C. V. Thompson, and L. A. Clevenger, "Nucleation and growth during reactions in multilayer Al/Ni films: The early stage of Al3Ni formation," *Journal of Applied Physics*, vol. 69, p. 2211, 1991.

[68] M. H. Da Silva Bassani, J. H. Perepezko, A. S. Edelstein, and R. K. Everett, "Initial phase evolution during interdiffusion reactions," *Scripta Materialia*, vol. 37, no. 2, pp. 227–232, 1997.

[69] U. Goesele and N. Tu, "Growth kinetics of planar binary diffusion couples: Thin-film case versus bulk cases," *Journal of Applied Physics*, vol. 53, no. 4, pp. 3252–3260, 1982.

[70] K. R. Coffey, L. A. Clevenger, K. Barmak, D. A. Rudman, and C. V. Thompson, "Experimental evidence for nucleation during thin-film reactions," *Applied Physics Letters*, vol. 55, no. 9, pp. 852–854, 1989.

[71] A. M. Brown and M. F. Ashby, "Correlations for Diffusion Constants." *Acta Metallurgica*, vol. 28, no. 8, pp. 1085–1101, 1980.

[72] A. Khawam and D. R. Flanagan, "Solid-state kinetic models: Basics and mathematical fundamentals," *Journal of Physical Chemistry B*, vol. 110, no. 35, pp. 17 315–17 328, 2006.

[73] S. Vyazovkin, A. K. Burnham, J. M. Criado, L. A. Pérez-Maqueda, C. Popescu, and N. Sbirrazzuoli, "ICTAC Kinetics Committee

recommendations for performing kinetic computations on thermal analysis data," *Thermochimica Acta*, vol. 520, no. 1-2, pp. 1–19, 2011.

[74] R. Pretorius, R. de Reus, A. M. Vredenberg, and F. W. Saris, "Use of the effective heat of formation rule for predicting phase formation sequence in AlNi systems," *Materials Letters*, vol. 9, no. 12, pp. 494–499, 1990.

[75] K. J. Blobaum, A. J. Wagner, J. M. Plitzko, D. Van Heerden, D. H. Fairbrother, and T. P. Weihs, "Investigating the reaction path and growth kinetics in CuOx/Al multilayer foils," *Journal of Applied Physics*, vol. 94, no. 5, pp. 2923–2929, 2003.

[76] C. Schick, *Fast Scanning Calorimetry*, 1st ed., Springer Berlin: Springer, 2016.

[77] M. D. Grapes, T. Lagrange, K. Woll, B. W. Reed, G. H. Campbell, D. A. Lavan, and T. P. Weihs, "In situ transmission electron microscopy investigation of the interfacial reaction between Ni and Al during rapid heating in a nanocalorimeter," *APL Materials*, vol. 2, no. 11, p. 116102, 2014.

[78] J. C. Trenkle, L. J. Koerner, M. W. Tate, N. Walker, S. M. Gruner, T. P. Weihs, and T. C. Hufnagel, "Time-resolved X-ray microdiffraction studies of phase transformations during rapidly propagating reactions in Al/Ni and Zr/Ni multilayer foils," *Journal of Applied Physics*, vol. 107, no. 11, p. 113511, 2010.

[79] M. Van Drongelen, T. Meijer-Vissers, D. Cavallo, G. Portale, G. V. Poel, and R. Androsch, "Microfocus wide-angle X-ray scattering of polymers crystallized in a fast scanning chip calorimeter," *Thermochimica Acta*, vol. 563, pp. 33–37, 2013.

[80] I. Stolte, D. Cavallo, G. C. Alfonso, G. Portale, M. V. Drongelen, and R. Androsch, "Form I′ crystal formation in random butene-1/propylene

copolymers as revealed by real-time X-ray scattering using synchrotron radiation and fast scanning chip calorimetry," *European Polymer Journal*, vol. 60, pp. 22–32, 2014.

[81] D. Baeten, V. B. Mathot, T. F. Pijpers, O. Verkinderen, G. Portale, P. Van Puyvelde, and B. Goderis, "Simultaneous synchrotron WAXD and fast scanning (chip) calorimetry: On the (isothermal) crystallization of HDPE and PA11 at high supercoolings and cooling rates up to 200 °C/s," *Macromolecular Rapid Communications*, vol. 36, no. 12, pp. 1184–1191, 2015.

[82] A. P. Melnikov, M. Rosenthal, A. I. Rodygin, D. Doblas, D. V. Anokhin, M. Burghammer, and D. A. Ivanov, "Re-exploring the double-melting behavior of semirigid-chain polymers with an in-situ combination of synchrotron nano-focus X-ray scattering and nanocalorimetry," *European Polymer Journal*, vol. 81, pp. 598–606, 2016.

[83] E. Parodi, L. E. Govaert, and G. W. Peters, "Glass transition temperature versus structure of polyamide 6: A flash-DSC study," *Thermochimica Acta*, vol. 657, pp. 110–122, 2017.

[84] J. M. Gregoire, K. Xiao, P. J. McCluskey, D. Dale, G. Cuddalorepatta, and J. J. Vlassak, "In-situ X-ray diffraction combined with scanning AC nanocalorimetry applied to a Fe0.84Ni0.16 thin-film sample," *Applied Physics Letters*, vol. 102, no. 20, pp. 0–4, 2013.

[85] P. J. McCluskey, K. Xiao, J. M. Gregoire, D. Dale, and J. J. Vlassak, "Application of in-situ nano-scanning calorimetry and X-ray diffraction to characterize Ni-Ti-Hf high-temperature shape memory alloys," *Thermochimica Acta*, vol. 603, pp. 53–62, 2015.

[86] M. Molina-Ruiz, P. Ferrando-Villalba, C. Rodriguez-Tinoco, G. Garcia, J. Rodriguez-Viejo, I. Peral, and A. F. Lopeandia, "Simultaneous

nanocalorimetry and fast XRD measurements to study the silicide formation in Pd/a-Si bilayers," *Journal of Synchrotron Radiation*, vol. 22, pp. 717–722, 2015.

[87] K. Willa, Z. Diao, D. Campanini, U. Welp, R. Divan, M. Hudl, Z. Islam, W. K. Kwok, and A. Rydh, "Nanocalorimeter platform for in situ specific heat measurements and x-ray diffraction at low temperature," *Review of Scientific Instruments*, vol. 88, no. 12, 2017.

[88] S. L. Lai, G. Ramanath, L. H. Allen, P. Infante, and Z. Ma, "High-speed (1000 °C/s) scanning microcalorimetry with monolayer sensitivity (J/m^2)," *Applied Physics Letters*, vol. 67, p. 1229, 1995.

[89] S. L. Lai, J. Y. Guo, V. Petrova, G. Ramanath, and L. H. Allen, "Size-dependent melting properties of small tin particles: Nanocalorimetric measurements," *Physical Review Letters*, vol. 77, no. 1, pp. 99–102, 1996.

[90] M. Schmidt, R. Kusche, B. von Issendorff, and H. Haberland, "Irregular variations in the melting point of size-selected atomic clusters," *Nature*, vol. 393, no. May, p. 238, 1998.

[91] S. A. Adamovsky, A. A. Minakov, and C. Schick, "Scanning microcalorimetry at high cooling rate," *Thermochimica Acta*, vol. 403, no. 1, pp. 55–63, 2003.

[92] A. A. Minakov, S. A. Adamovsky, and C. Schick, "Non-adiabatic thin-film (chip) nanocalorimetry," *Thermochimica Acta*, vol. 432, no. 2, pp. 177–185, 2005.

[93] K. Woll, T. Neuhauser, C. Acuña, D. Diaz-Droguett, and A. Rosenkranz, "Rapid thermal characterization of graphene oxide-nanocalorimetry as a pathway for novel insights in tribology," *Lubricants*, vol. 7, no. 11, p. 96, 2019.

[94] E. A. Olson, M. Y. Efremov, M. Zhang, Z. Zhang, and L. H. Allen, "The design and operation of a MEMS differential scanning nanocalorimeter for high-speed heat capacity measurements of ultrathin films," *Journal of Microelectromechanical Systems*, vol. 12, no. 3, pp. 355–364, 2003.

[95] F. Yi, M. D. Grapes, and D. A. Lavan, "Practical Guide to the Design, Fabrication and Calibration of NIST Nanocalorimeters," *Journal of Research of the National Institute of Standards and Technology*, vol. 124, no. 124021, pp. 1–19, 2019.

[96] P. Swaminathan, B. G. Burke, A. E. Holness, B. Wilthan, L. Hanssen, T. P. Weihs, and D. A. Lavan, "Optical calibration for nanocalorimeter measurements," *Thermochimica Acta*, vol. 522, no. 1-2, pp. 60–65, 2011.

[97] M. Y. Efremov, E. A. Olson, M. Zhang, F. Schiettekatte, Z. Zhang, and L. H. Allen, "Ultrasensitive, fast, thin-film differential scanning calorimeter," *Review of Scientific Instruments*, vol. 75, no. 1, pp. 179–191, 2004.

[98] R. M. Tiggelaar, R. G. Sanders, A. W. Groenland, and J. G. Gardeniers, "Stability of thin platinum films implemented in high-temperature microdevices," *Sensors and Actuators, A: Physical*, vol. 152, no. 1, pp. 39–47, 2009.

[99] L. N. Aksyutov, "Normal spectral emissivity of gold, platinum, and tungsten," *Journal of Engineering Physics*, vol. 27, no. 2, pp. 913–917, 1976.

[100] W. Sabuga and R. Todtenhaupt, "Effect of roughness on the emissivity of the precious metals silver, gold, palladium, platinum, rhodium, and iridium," *High Temperatures - High Pressures*, vol. 33, no. 3, pp. 261–269, 2001.

[101] S. Deemyad and I. F. Silvera, “Temperature dependence of the emissivity of platinum in the IR,” *Review of Scientific Instruments*, vol. 79, no. 8, pp. 3–5, 2008.

[102] C. P. Cagran, L. M. Hanssen, M. Noorma, A. V. Gura, and S. N. Mekhontsev, “Temperature-resolved infrared spectral emissivity of SiC and Pt-10Rh for temperatures up to 900°C,” *International Journal of Thermophysics*, vol. 28, no. 2, pp. 581–597, 2007.

[103] D. R. Lide, *CRC handbook of chemistry and physics: a ready-reference book of chemical and physical data*,76th ed., Boca Raton: CRC press, 1995.

[104] F. Yi, W. Osborn, J. Betz, and D. A. Lavan, “Interactions of Adhesion Materials and Annealing Environment on Resistance and Stability of MEMS Platinum Heaters and Temperature Sensors,” *Journal of Microelectromechanical Systems*, vol. 24, no. 4, pp. 1185–1192, 2015.

[105] J. L. Garden, H. Guillou, A. F. Lopeandia, J. Richard, J. S. Heron, G. M. Souche, F. R. Ong, B. Vianay, and O. Bourgeois, “Thermodynamics of small systems by nanocalorimetry: From physical to biological nano-objects,” *Thermochimica Acta*, vol. 492, no. 1-2, pp. 16–28, 2009.

[106] A. Dinsdale, *SGTE data for pure elements* Teddington: National Physical Laboratory, 1989.

[107] J. W. Pomeroy, M. Kuball, D. J. Wallis, A. M. Keir, K. P. Hilton, R. S. Balmer, M. J. Uren, T. Martin, and P. J. Heard, “Thermal mapping of defects in AlGaN/GaN heterostructure field-effect transistors using micro-Raman spectroscopy,” *Applied Physics Letters*, vol. 87, no. 10, 2005.

[108] J. Zheng, H. Zhang, Y. Miao, S. Chen, and J. J. Vlassak, “Temperature-resistance sensor arrays for combinatorial study of phase

transitions in shape memory alloys and metallic glasses," *Scripta Materialia*, vol. 168, pp. 144–148, 2019.

[109] S. M. Sarge, G. W. H. Höhne, and W. Hemminger, *Calorimetry - Fundamentals, Instrumentation and Applications*, 1st ed., Weinheim: Wiley-VCH Verlag GmbH & Co, 2014.

[110] M. D. Grapes and T. P. Weihs, "Exploring the reaction mechanism in self-propagating Al/Ni multilayers by adding inert material," *Combustion and Flame*, vol. 172, pp. 105–115, 2016.

[111] A. Minakov, J. Morikawa, T. Hashimoto, H. Huth, and C. Schick, "Temperature distribution in a thin-film chip utilized for advanced nanocalorimetry," *Measurement Science and Technology*, vol. 17, no. 1, pp. 199–207, 2006.

[112] A. A. Minakov and C. Schick, "Ultrafast thermal processing and nanocalorimetry at heating and cooling rates up to 1 MK/s," *Review of Scientific Instruments*, vol. 78, no. 7, 2007.

[113] D. R. Queen and F. Hellman, "Thin film nanocalorimeter for heat capacity measurements of 30 nm films," *Review of Scientific Instruments*, vol. 80, no. 6, 2009.

[114] R. G. Spruit, J. Tijn Van Omme, M. K. Ghatkesar, and H. Hugo Pérez Garza, "A review on development and optimization of microheaters for high-temperature in situ studies," *Journal of Microelectromechanical Systems*, vol. 26, no. 6, pp. 1165–1182, 2017.

[115] W. Kiyotaka and S. Hayakawa, *Handbook of sputter deposition technology : principles, technology and applications*, 12th ed., Park Ridge: Noyes Publication, 1992.

[116] A. P. Melnikov, M. Rosenthal, M. Burghammer, D. V. Anokhin, and D. A. Ivanov, "Study of Melting Processes in Semicrystalline Polymers

Using a Combination of Ultrafast Chip Calorimetry and Nanofocus Synchrotron X-Ray Diffraction," *Nanotechnologies in Russia*, vol. 11, no. 5-6, pp. 305–311, 2016.

[117] F. Nemouchi, D. Mangelinck, C. Bergman, P. Gas, and U. Smith, "Differential scanning calorimetry analysis of the linear parabolic growth of nanometric Ni suicide thin films on a Si substrate," *Applied Physics Letters*, vol. 86, no. 4, pp. 9–12, 2005.

[118] J. M. Gregoire, P. J. McCluskey, D. Dale, S. Ding, J. Schroers, and J. J. Vlassak, "Combining combinatorial nanocalorimetry and X-ray diffraction techniques to study the effects of composition and quench rate on Au-Cu-Si metallic glasses," *Scripta Materialia*, vol. 66, no. 3-4, pp. 178–181, 2012.

[119] P. Zalden, G. Aquilanti, C. Prestipino, O. Mathon, B. André, M. Wuttig, and M. V. Coulet, "Simultaneous calorimetric and quick-EXAFS measurements to study the crystallization process in phase-change materials," *Journal of Synchrotron Radiation*, vol. 19, no. 5, pp. 806–813, 2012.

[120] K. Xiao, J. M. Gregoire, P. J. McCluskey, D. Dale, and J. J. Vlassak, "Scanning AC nanocalorimetry combined with in-situ x-ray diffraction," *Journal of Applied Physics*, vol. 113, no. 24, p. 243501, 2013.

[121] P. R. Willmott, D. Meister, S. J. Leake, M. Lange, and A. Bergamaschi, "The Materials Science beamline upgrade at the Swiss Light Source," *Journal of Synchrotron Radiation*, vol. 20, no. 5, pp. 667–682, 2013.

[122] R. Dinapoli, A. Bergamaschi, D. Greiffenberg, B. Henrich, R. Horisberger, I. Johnson, A. Mozzanica, V. Radicci, B. Schmitt, X. Shi, and G. Tinti, "EIGER characterization results," *Nuclear Inst. and Methods in Physics Research, A*, vol. 731, pp. 68–73, 2013.

[123] I. Johnson, A. Bergamaschi, H. Billich, S. Cartier, R. Dinapoli, D. Greiffenberg, M. Guizar-Sicairos, B. Henrich, J. Jungmann, D. Mezza, A. Mozzanica, B. Schmitt, X. Shi, and G. Tinti, "Eiger: A single-photon counting x-ray detector," *Journal of Instrumentation*, vol. 9, p. C05032, 2014.

[124] G. Tinti, "To be submitted: 20-70 kHz time resolved reactive multilayer diffraction with a fast EIGER detector".

[125] V. Radicci, A. Bergamaschi, R. Dinapoli, D. Greiffenberg, B. Henrich, I. Johnson, A. Mozzanica, B. Schmitt, and X. Shi, "EIGER a new single photon counting detector for X-ray applications: performance of the chip," *Journal of Instrumentation*, vol. 7, 2012.

[126] T. Neuhauser, G. Tinti, H. Leiste, N. Casati, S. Ulrich, M. Stüber, and K. Woll, "The role of two-stage phase formation for the solid-state runaway reaction in Al/Ni reactive multilayers," *Applied Physics Letters*, vol. 117, no. 1, p. 011902, 2020.

[127] P. Scherrer, "Bestimmung der inneren Struktur und der Größe von Kolloidteilchen mittels Röntgenstrahlen," in *Kolloidchemie Ein Lehrbuch*. Berlin: Springer, 1912, pp. 387–409.

[128] J. Kieffer and D. Karkoulis, "PyFAI, a versatile library for azimuthal regrouping," *Journal of Physics: Conference Series*, vol. 425, p. 202012, 2013.

[129] V. Dyadkin, P. Pattison, V. Dmitriev, and D. Chernyshov, "A new multipurpose diffractometer PILATUS@SNBL," *Journal of Synchrotron Radiation*, vol. 23, no. 3, pp. 825–829, 2016.

[130] M. H. F. Overwijk, "Novel scheme for the preparation of transmission electron microscopy specimens with a focused ion beam," *Journal of Vacuum Science & Technology B: Microelectronics and Nanometer Structures*, vol. 11, no. 6, p. 2021, 1993.

[131] L. A. Giannuzzi and F. A. Stevie, “A review of focused ion beam milling techniques for TEM specimen preparation,” *Micron*, vol. 30, no. 3, pp. 197–204, 1999.

[132] F. I. Z. Karlsruhe, *ICSD Inorganic Crystal Structure Database.*, 2021. Retrieved September 2021: https://icsd.fiz-karlsruhe.de/search/basic.xhtml

[133] H. E. Kissinger, “Reaction Kinetics in Differential Thermal Analysis,” *Helv. Chim. Acta*, vol. 28, no. 5, p. 73, 1956.

[134] V. Schnabel, A. S. Sologubenko, S. Danzi, G. Kurtuldu, and R. Spolenak, “Controlling diffusion in Ni/Al reactive multilayers by Nb-alloying,” *Applied Physics Letters*, vol. 111, no. 17, p. 173902, 2017.

[135] J. P. Liu, J. Kirchhoff, L. Zhou, M. Zhao, M. D. Grapes, D. S. Dale, M. D. Tate, H. T. Philipp, S. M. Gruner, T. P. Weihs, and T. C. Hufnagel, “X-ray reflectivity measurement of interdiffusion in metallic multilayers during rapid heating,” *Journal of Synchrotron Radiation*, vol. 24, no. 4, pp. 796–801, 2017.

[136] R. Grieseler, I. S. Au, T. Kups, and P. Schaaf, “Diffusion in thin bilayer films during rapid thermal annealing,” *Physica Status Solidi (A) Applications and Materials Science*, vol. 211, no. 11, pp. 2635–2644, 2014.

[137] H. Joress, S. Q. Arlington, T. P. Weihs, J. D. Brock, and A. R. Woll, “X-ray reflectivity with a twist: Quantitative time-resolved X-ray reflectivity using monochromatic synchrotron radiation,” *Applied Physics Letters*, vol. 114, no. 8, 2019.

[138] F. J. Gotor, José, M. Criado, J. Malek, and N. Koga, “Kinetic analysis of solid-state reactions: The universality of master plots for analyzing

isothermal and nonisothermal experiments," *Journal of Physical Chemistry A*, vol. 104, no. 46, pp. 10 777–10 782, 2000.

[139] Y. Wang, Z. K. Liu, and L. Q. Chen, "Thermodynamic properties of Al, Ni, NiAl, and Ni3Al from first-principles calculations," *Acta Materialia*, vol. 52, no. 9, pp. 2665–2671, 2004.

[140] J. Morgiel, M. Szlezynger, M. Pomorska, L. Maj, K. Marszalek, and R. Mania, "In-situ TEM heating of Ni / Al multilayers," *XV International Conference on Electron Microscopy*,, vol. 106, no. 7, pp. 703–710, 2014.

[141] A. M. B. Douglas, "The structure of Co2Al9," *Acta Crystallographica*, vol. 3, no. 1, pp. 19–24, 1950.

[142] A. Yamamoto and H. Tsubakino, "Al9Ni2 precipitates formed in an Al-Ni dilute alloy," *Scripta Materialia*, vol. 37, no. 11, pp. 1721–1725, 1997.

[143] F. Ainutdinov, S. Khairidinov, and A. Vakhobov, "Phase Diagram of the System Aluminum-Barium-Nickel," *Doklady Akademii Nauk Tadzhikskoi SSR*, vol. 30, no. 3, pp. 169–172, 1987.

[144] L. Zhang, L. H. Zhang, M. L. Sui, J. Tan, and K. Lu, "Superheating and melting kinetics of confined thin films," *Acta Materialia*, vol. 54, no. 13, pp. 3553–3560, 2006.

[145] T. S. Dyer and Z. A. Munir, "The synthesis of nickel aluminides by multilayer self-propagating combustion," *Metallurgical and Materials Transactions B*, vol. 26, no. 3, pp. 603–610, 1995.

[146] A. S. Mukasyan, C. E. Shuck, J. M. Pauls, K. V. Manukyan, D. O. Moskovskikh, and A. S. Rogachev, "The Solid Flame Phenomenon: A Novel Perspective," *Advanced Engineering Materials*, vol. 20, no. 8, p. 1701065, 2018.

[147] D. Y. Kovalev, N. A. Kochetov, V. I. Ponomarev, and A. S. Mukasyan, "Effect of mechanical activation on thermal explosion in Ni-Al mixtures," *International Journal of Self-Propagating High-Temperature Synthesis*, vol. 19, no. 2, pp. 120–125, 2010.

[148] A. S. Mukasyan, J. D. White, D. Y. Kovalev, N. A. Kochetov, V. I. Ponomarev, and S. F. Son, "Dynamics of phase transformation during thermal explosion in the Al-Ni system: Influence of mechanical activation," *Physica B: Condensed Matter*, vol. 405, no. 2, pp. 778–784, 2010.

[149] C. E. Shuck, J. M. Pauls, and A. S. Mukasyan, "Ni/Al Energetic Nanocomposites and the Solid Flame Phenomenon," *Journal of Physical Chemistry C*, vol. 120, no. 47, pp. 27 066–27 078, 2016.

[150] A. S. Rogachev, S. G. Vadchenko, and A. S. Mukasyan, "Self-sustained waves of exothermic dissolution in reactive multilayer nano-foils," *Applied Physics Letters*, vol. 101, no. 6, p. 063119, 2012.

[151] Y. Du, Y. A. Chang, B. Huang, W. Gong, Z. Jin, H. Xu, Z. Yuan, Y. Liu, Y. He, and F. Y. Xie, "Diffusion coefficients of some solutes in fcc and liquid Al: Critical evaluation and correlation," *Materials Science and Engineering A*, vol. 363, no. 1-2, pp. 140–151, 2003.

[152] A. S. Rogachev, S. G. Vadchenko, F. Baras, O. Politano, S. Rouvimov, N. V. Sachkova, and A. S. Mukasyan, "Structure evolution and reaction mechanism in the Ni/Al reactive multilayer nanofoils," *Acta Materialia*, vol. 66, pp. 86–96, 2014.

[153] J. S. Kim, T. Lagrange, B. W. Reed, R. Knepper, T. P. Weihs, and N. D. Browning, "Direct characterization of phase transformations and morphologies in moving reaction zones in Al/Ni nanolaminates using dynamic transmission electron microscopy," *Acta Materialia*, vol. 59, no. 9, pp. 3571–3580, 2011.

[154] Z. Ding, Q. Hu, W. Lu, S. Sun, M. Xia, and J. Li, "In situ observation on the formation of intermetallics compounds at the interface of liquid Al/solid Ni," *Scripta Materialia*, vol. 130, pp. 214–218, 2017.

[155] Z. Ding, Q. Hu, W. Lu, S. Sun, M. Xia, and J. Li, "In-Situ Observation on the Diversified Morphology and Growth Behavior of Al3Ni Phase at the Liquid Al/Solid Ni Interface," *Metallurgical and Materials Transactions A: Physical Metallurgy and Materials Science*, vol. 49, no. 5, pp. 1486–1491, 2018.

[156] R. Pretorius, A. M. Vredenberg, F. W. Saris, and R. De Reus, "Prediction of phase formation sequence and phase stability in binary metal-aluminum thin-film systems using the effective heat of formation rule," *Journal of Applied Physics*, vol. 70, no. 7, pp. 3636–3646, 1991.

[157] P. Swaminathan, D. A. Lavan, and T. P. Weihs, "Dynamics of solidification in Al thin films measured using a nanocalorimeter," *Journal of Applied Physics*, vol. 110, no. 11, 2011.

[158] A. Gualtieri, P. Norby, J. Hanson, and J. Hriljac, "Rietveld Refinement using Synchrotron X-ray Powder Diffraction Data Collected in Transmission Geometry using an Imaging-Plate Detector: Application to Standard m-ZrO2," *Journal of Applied Crystallography*, vol. 29, pp. 707–713, 1996.

[159] P. Norby, "Synchrotron Powder Diffraction using Imaging Plates: Crystal Structure Determination and Rietveld Refinement," *Journal of Applied Crystallography*, vol. 30, no. 1, pp. 21–30, 1997.

[160] J. H. Hubbell and S. M. Seltzer, "Tables of X-Ray Mass Attenuation Coefficients and Mass Energy-Absorption Coefficients 1 keV to 20 MeV for Elements Z = 1 to 92 and 48 Additional Substances of Dosimetric Interest," Washington: U.S. Department of Commerce, 1995.

List of figures

List of tables

List of publications

1. K. Woll, **T. Neuhauser**, C. Acuña, D. Diaz-Droguett, and A. Rosenkranz, "Rapid thermal characterization of graphene oxide-nanocalorimetry as a pathway for novel insights in tribology," Lubricants, vol. 7, no. 11, p. 96, 2019.
   The co-author Tobias Neuhauser carried out the nanocalorimetric experiments on graphene-oxide. Additionally, he provided the schematic drawings and conducted the microscopical investigations.

2. **T. Neuhauser**, G. Tinti, H. Leiste, N. Casati, M. Stüber, and K. Woll, "Analysis of the reaction runaway in Al/Ni multilayers with combined nanocalorimetry and time-resolved X-ray diffraction," Acta Materialia, vol. 195, pp. 579–587, 2020.

3. **T. Neuhauser**, G. Tinti, H. Leiste, N. Casati, S. Ulrich, M. Stüber, and K. Woll, "The role of two-stage phase formation for the solid-state runaway reaction in Al/Ni reactive multilayers," Applied Physics Letters, vol. 117, no. 1, p. 011902, 2020.

A Appendix

A.1 Technical drawings

The technical drawings of the nanocalorimetry setup introduced in Chapter 3 are shown here. The dimensions of the nanocalorimetry sensors are shown in Figure A.1. The *ex situ* nanocalorimetry setup is depicted in Figure A.2. Figure A.3 shows the technical drawing of the shadow mask used for sputter deposition of the thin-film samples on the nanocalorimetry sensors. The *in situ* nanocalorimetry setup for synchrotron measurements is depicted in Figure A.4.

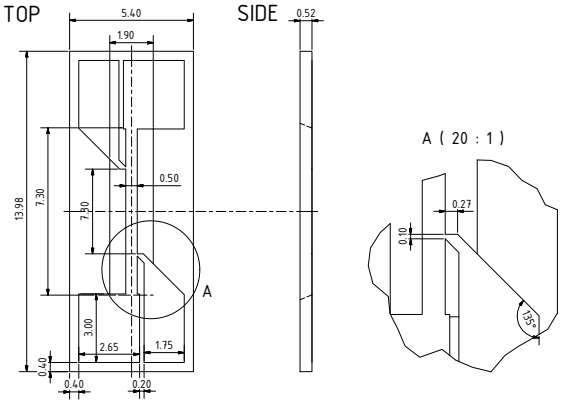

Figure A.1: Technical drawing of the nanocalorimetry sensor. The geometry and dimensions of the sensor are adopted from *Lai and Allen* [88] and *Swaminathan et al.* [157].

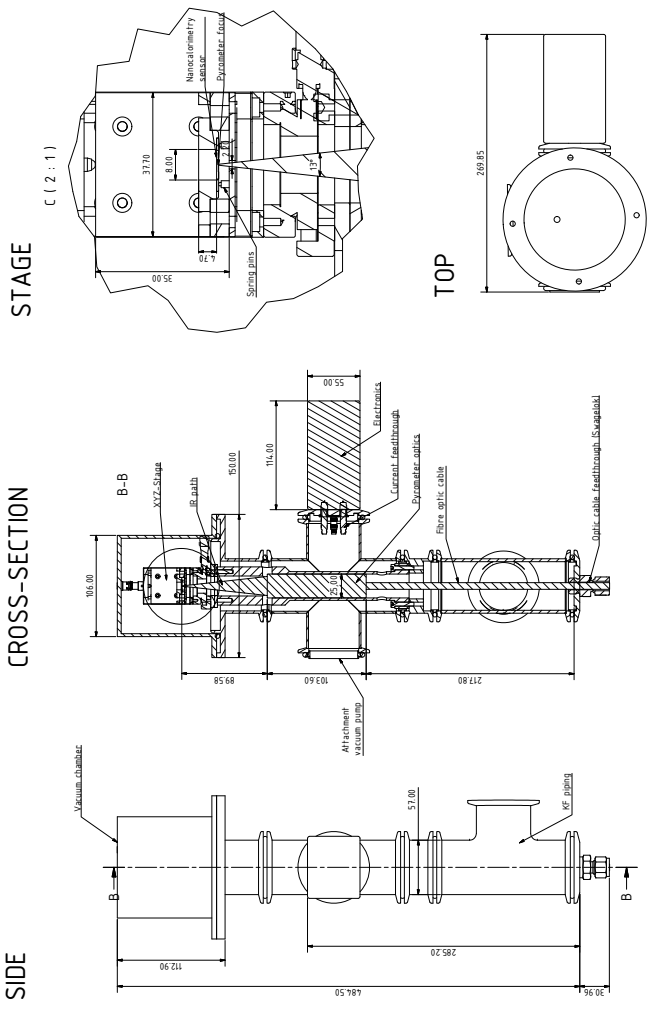

Figure A.2: Technical drawing of the *ex situ* nanocalorimetry setup. The stage where the nanocalorimetry sensor is positioned is shown enlarged.

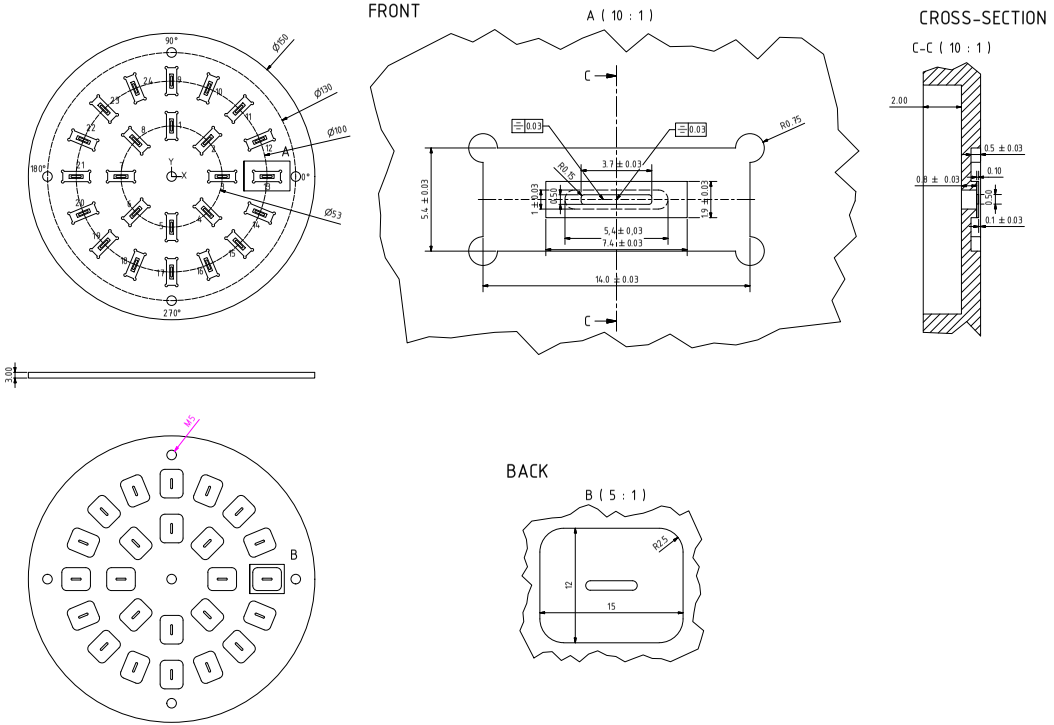

Figure A.3: Technical drawing of the shadow mask for sputter deposition of the Al/Ni multilayers on the nanocalorimetry sensors. The cavities for positioning the nanocalorimetry sensors are shown enlarged.

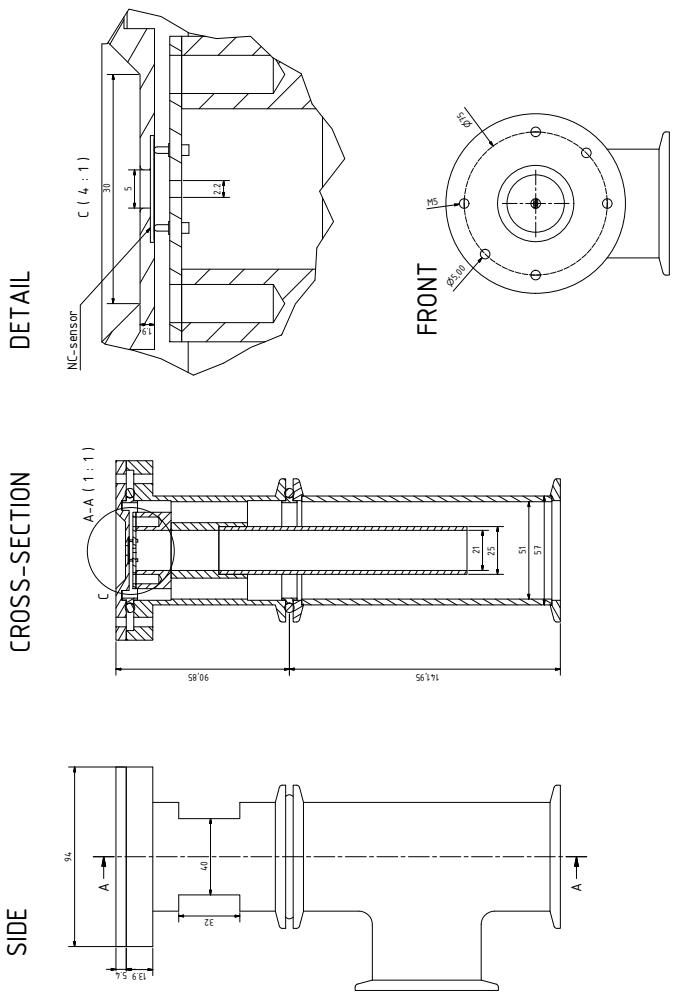

Figure A.4: Technical drawing of the textitin situ nanocalorimetry-synchrotron setup. The nanocalorimetry sensor holder is shown in detail.

A.2 Graphical user interface

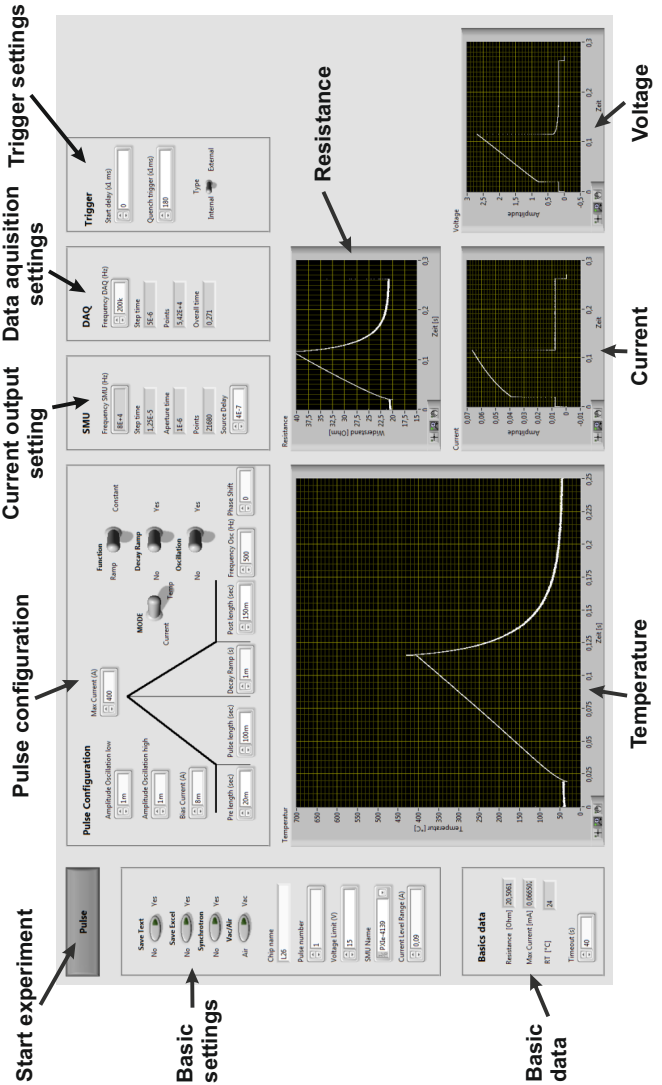

Figure A.5: Graphical user interface of the nanocalorimetry software.

A.3 Calibration of the nanocalorimetry sensor position

For the temperature calibration of the nanocalorimetry sensors, infrared pyrometry was used. A detailed description of the calibration procedure can be found in Section 3.1.4. For a highly accurate temperature measurement, positioning of the nanocalorimetry sensor relative to the infrared measurement spot is crucial. Therefore, the effect of misalignment of the sensor in the x-, y- and z-direction was evaluated. Figure A.6 plots the the temperature distribution along the heating strip (= x-axis) of the sensor. An empty sensor (black line) is compared to a sensor with 150 nm (red line) and 930 nm (blue line) Al sample. For all investigations, a membrane thickness 100 nm was chosen. The reference temperature is 500 °C. It was found that within the active area of the sensor, the temperature is almost constant. The presence of a sample leads to homogenization of the temperature distribution in the active area. Beside the active area, deviations of the reference temperature of +14 °C and +68 °C were found in the case of a 150 nm and a 930 nm Al sample. In contrast, in the case of an empty sensor, the temperature deviation is -23°C. Since the temperature measurement is restricted to the active area, this does not affect the temperature accuracy.

Figure A.7 plots the temperature distribution perpendicular to the Pt heating strip (y-axis). Again a reference temperature of 500 °C was chosen. It was found that a misalignment in the y-direction is causing a temperature error. Exemplarily, a misalignment of 250 µm causes a temperature error of -90 °C. The reason for this is the lower infrared emissivity of the SiN_x membrane compared to Pt. Due to the lower emissivity, the temperature measured by the pyrometer is incorrect. The peak shape of the temperature distribution indicates that the lateral dimension of the infrared measurement spot exceeds the width of the heating strip. Otherwise, a plateau would be observed. Figure A.8

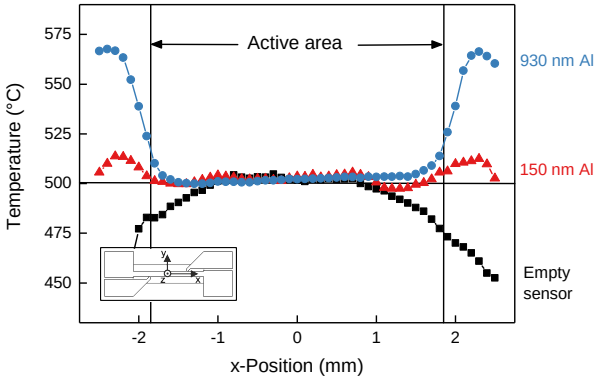

Figure A.6: Temperature distribution along the Pt heating strip of a 100 nm nanocalorimetry sensor with and without Al sample. By adding a sample, the temperature distribution is homogenized in the active area (= measurement area).

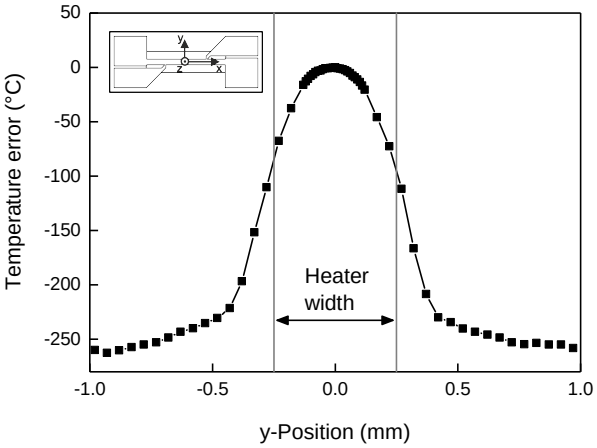

Figure A.7: Temperature distribution perpendicular to the Pt heating strip. Deviations of the central position of the measurement spot cause a temperature error due to the lower emissivity of the SiN_x membrane.

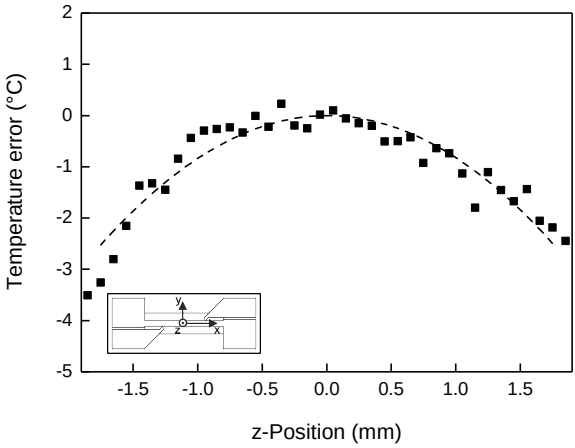

Figure A.8: Temperature errors due to the deviations of the infrared measurement spot focal plane from the sensor heating strip.

plots the measured temperature along the sensor plane normal (= z-direction). The reference temperature was 500 °C. Deviations from the focal plane of the infrared measurement spot causing only marginal temperature errors. Exemplarily, if the focal plane is ± 1mm above or below the heating strip, a temperature error of -1 °C is measured. This is caused by an increase in the infrared spot size above and below the focal plane.

A.4 Nanocalorimetry temperature calibration with thick Al samples

To prove the accuracy of the resistance temperature measurement in the case of thick samples ($d_{sample} > 1$ µm), melting experiments of Al were performed. For this purpose, a 2-µm-thick Al sample was deposited on a nanocalorimetry

sensor with a membrane thickness of 1 µm. Figure A.9 shows the temperature profile when the sample is heated with a rate of 10^4 K s^{-1}. Starting at 657 °C, the temperature signal deviates from a linear behaviour. This indicates the onset of Al melting. At a temperature of 667 °C, there is a significant decrease in the heating rate. The melting temperature of a thick Al sample is in good agreement with the previously determined temperature for thin Al samples (T_m = 660.3 ± 5.8 °C). This corroborates the accuracy of the temperature measurement.

A.5 Evaluation of the X-ray intensity

The intensity of a diffracted X-ray beam is dependent on various parameters, e.g. the crystal structure of the material or the diffraction geometry [4]. To

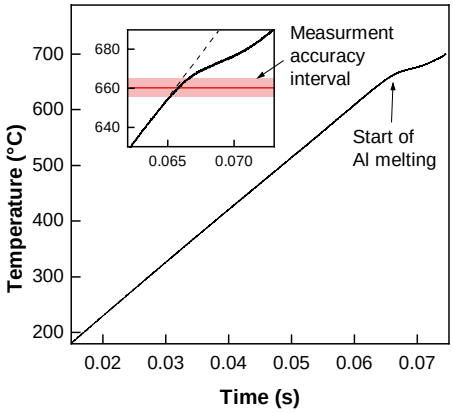

Figure A.9: Temperature signal of a nanocalorimetry sensor with a membrane thickness of 1 µm and a 2-µm-thick Al sample. The onset of melting, indicated by the deviation of the linear heating curve, is in good agreement with the reference value for Al melting (T_m = 660 °C).

use the peak intensity for the evaluation of the phase fraction, all parameters influencing the intensity have to be considered. In the case of Debye-Scherrer powder diffraction, the intensity of an X-ray beam which is diffracted at the (hkl)-plane is given by

$$I_{hkl} = I_0 \cdot K_{XRD} \cdot L(\theta) \cdot P(\theta) \cdot E_X \cdot H \cdot T^2_{coeff} \cdot A_{ab} \cdot \mid F(hkl) \mid^2 \cdot \upsilon_i \qquad \text{(A.1)}$$

where I_{hkl} is the diffracted intensity, I_0 the incoming intensity, K_{XRD} the scale factor, $L(\theta)$ the Lorentz factor, $P(\theta)$ the polarization factor, E_X extinction factor, H relative number of diffraction planes, T^2_{coeff} temperature coefficient, $\mid F(hkl) \mid^2$ the structure factor, A_{ab} the absorption coefficient and υ_i the volume concentration of phase i. If all coefficients are known, based on I_{hkl} the volume concentration of a phase can be determined [4]. Practically, the determination of all factors in an experimental setup is challenging. Therefore, in this study not the quantitative values of υ_i were determined, but the relative values $\upsilon_i/\upsilon_{i,max}$ of selected phases. If the coefficients in equation A.1 remain constant during experiment a direct correlation between υ_i and I_{hkl} is given. In the following, all coefficients which potentially change during experiment are evaluated. Coefficient which are constant due to physical reasons (K_{XRD}, H, E_X and $\mid F(hkl) \mid^2$) are not considered.

Incoming X-ray intensity I_0

For technical reasons, the X-ray photon flux of the SLS synchrotron is not constant during the experiment. Figure A.10 shows that the intensity fluctuates up to 8% during experiment. A correction factor is introduced to compensate for this. The factor is determined based on the diffusive background scattering. For this purpose, a regime of $16.8° < 2\theta < 17.6°$ was selected where no diffraction peaks are present. The factor is calculated by integrating the 2θ regime and normalize the value to the peak value.

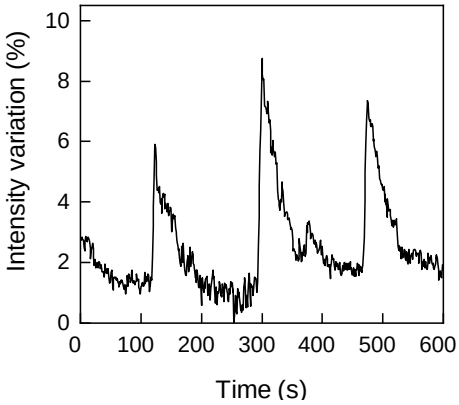

Figure A.10: The intensity of the incoming X-ray beam. Fluctuations up to 8% are compensated by determining a correction factor in a selected 2θ regime of the diffractogram.

Geometrical dependent factors $L(\theta), P(\theta)$

All diffraction-angle-dependent factors are summarized in the $LP(\theta)$ factor. This comprises the Lorentz factor and the polarization factor. These factors summarize all geometrical aspects. In the synchrotron setup used in this work, the incoming beam is horizontally polarized and the 2D area detector is correct for the polarization. Therefore, it can be assumed that $P(\theta) = 1$. For a more detailed description, it should be referred to *Spieß et al.* [4]. In the case of transmission powder diffraction, the $LP(\theta)$ factor is given by [158, 159]

$$LP(\Theta) = \frac{\cos(2\Theta - \chi)}{\sin^2(\Theta)\cos(\Theta)} \tag{A.2}$$

where θ is the diffraction angle and χ the angle between the incoming beam and the normal of the X-ray detector. For χ a value of 26.3° was determined. Figure A.11 plots the $LP(\Theta)$ coefficient in dependence of 2θ angle.
The $LP(\theta)$ coefficient decreases with increasing 2θ angle. Diffraction peaks at low 2θ angles are more pronounced. In the context of the analysis, only

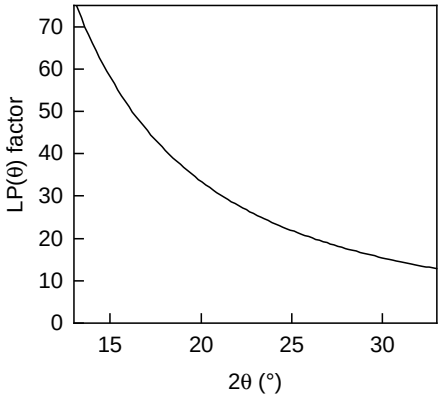

Figure A.11: Calculation of the Lorentz factor in Debye-Scherrer powder diffraction [158, 159].

the change of the peak intensity with a peak shift during the experiment is of interest. Peak shifts are caused by thermal expansion or a change of the stress state in the sample. For a conservative estimation the Al_3Ni [110]-peak at 2θ = 14.06° was selected. Typically, during cooling from 661 °C to 209 °C a shift of the peak of 0.08 ° is observed. This results in a change of the $LP(\theta)$ coefficient of 1.1 %, which is negligible.

The temperature coefficient T^2_{coeff}

The diffracted intensity is dependent on the sample temperature. The reason for this are atomic vibrations (= phonons), which cause attenuation of X-ray scattering with increasing temperature [4].

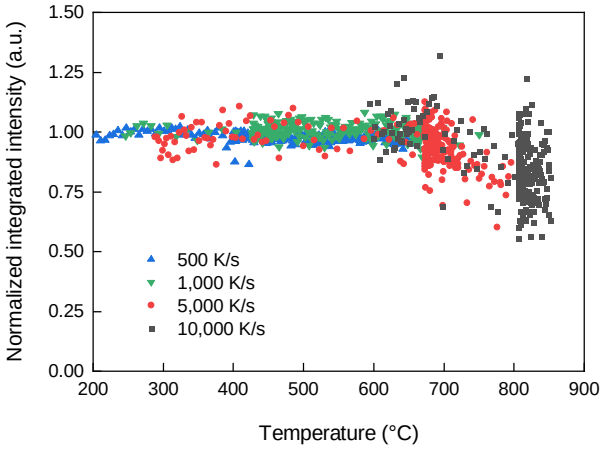

Figure A.12: Summed diffracted intensity of Al_3Ni peaks versus temperature. It was found that up to the melting temperature of excess Al, the intensity is independent of the temperature.

Physically, this phenomenon can be described with

$$T^2_{coeff} = \exp\left(-2B_{DW}\frac{\sin^2(\Theta)}{\lambda^2}\right) \tag{A.3}$$

where B_{DW} is the Debye-Waller factor, θ the diffraction angle and λ the X-ray wavelength. In the case of the intermetallic compounds investigated in this study, namely Al_3Ni and Al_9Ni_2, to the knowledge of the author, no literature values of B_{DW} are available. To overcome this, the diffracted intensity of Al_3Ni versus the temperature was evaluated. For this purpose, the *in situ* nanocalorimetry setup was used to heat a sample after the reaction. Since the amount of Al_9Ni_2 and Al_3Ni remains constant, the influence of the temperature on I_{hkl} can be estimated. Figure A.12 plots the summed normalized intensity of selected Al_3Ni diffraction peaks. Four samples were heated at different rates of $5 \cdot 10^2$ Ks^{-1}, $1 \cdot 10^3$ Ks^{-1}, $5 \cdot 10^3$ Ks^{-1} and $1 \cdot 10^4$ Ks^{-1}. Up to the melting

temperature of the excess Al, the intensity of Al_3Ni remains constant. Since the I-signal is not only influenced by the temperature coefficient but also by all other factors of equation A.1, it can be concluded that a proportional correlation between integrated intensity and amount of phase is given below the melting temperature of Al. At temperatures above 660 °C, most likely stress relaxation and the change in the absorption coefficient may lower the diffracted intensity. Because of this, the analysis of the diffracted intensity was limited to a temperature below 660 °C.

The absorption coefficient A_{ab}

An X-ray beam penetrating a sample is getting absorbed by interactions between the photons and the material. This phenomenon can be described with the Beer-Lambert law

$$A_{ab} = \frac{I}{I_0} = \exp(-(\mu/\rho d_{sample}) \tag{A.4}$$

where I_0 is the incident beam intensity, I the attenuated beam intensity by absorption, μ/ρ the mass attenuation coefficient consisting of the attenuation coefficient μ and the density ρ and the sample thickness d_{sample}. A_{ab} can be either influenced by the material or by the path length of the X-ray beam through the sample. In the case of compounds, the mass attenuation coefficient can be calculated by summation of their weighted fraction [160]

$$\frac{\mu}{\rho} = \sum_i \omega(\mu/\rho)_i \tag{A.5}$$

Here, $(\mu/\rho)_i$ is the mass attenuation coefficient of element i and ω is the fraction by weight. In the case of nanocalorimetry experiments, the overall sample composition during the experiment remains constant. The formation of intermetallic compounds does not alter the total amount of atoms contributing to

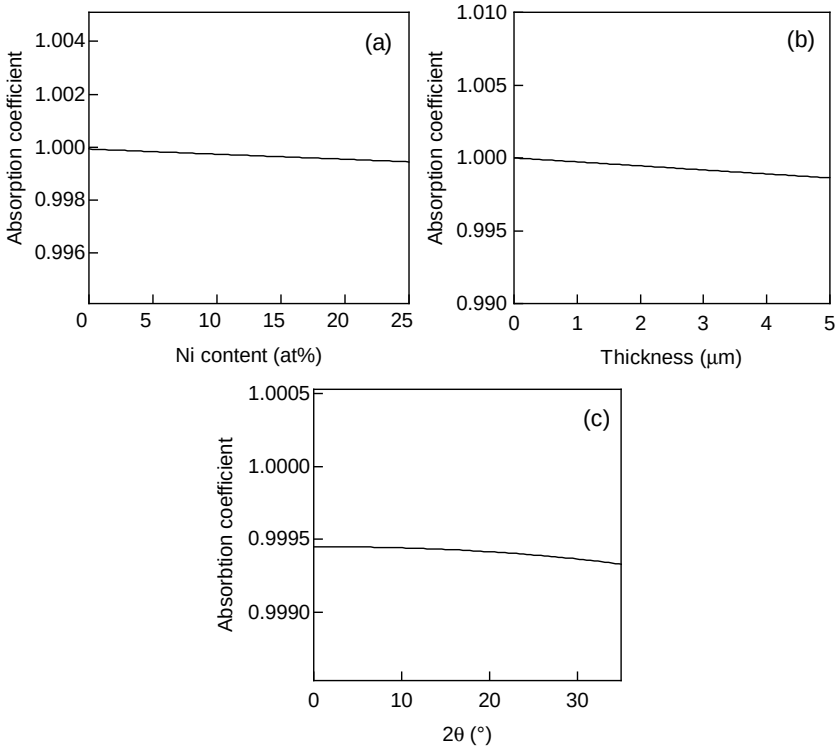

Figure A.13: The normalized X-ray absorption coefficient of an Al/Ni sample in dependence of (a) the sample composition, (b) the total sample thickness and (c) the 2θ angle.

the attenuation of the X-ray beam during heating. Therefore, a negative effect of variations in μ/ρ can be excluded. However, the variation of the Ni content, total sample thickness and 2θ angle have to be evaluated.

Figure A.13 (a) plots the adsorption coefficient versus the Ni content. The variation of the Ni content between 5 at.% and 25 at.% Ni results in a change of A_{ab} of about 0.05 %. The reason for this is the low sample thickness which does hardly influence A_{ab}. Figure A.13 (b) and (c) show the influence of the

sample thickness and 2θ angle on A_{ab}. In both cases the X-ray beam is attenuated by a extended path length through the sample. If the sample thickness is increased from 1 to 5 µm, A_{ab} is reduced by 0.13 %. A change of the 2θ angle from 0° to 35° results in a reduction of A_{ab} of about 0.01 %. Therefore, both contributions are negligible.

Crystal orientation

For a quantitative phase analysis using powder diffraction, a random distribution of the crystal within the sample is required [4]. Although the X-ray diffraction setup in this study does not allow a definite determination of the crystal orientation (multiple incidence angles of the X-ray beam are required), the given data give a strong indication for a random distribution of the Al_3Ni and Al_9Ni_2 phase. Figure A.14 (a) shows the diffractogram of a Al/Ni sample with 10 at.% Ni after isothermally heated at 276 °C. The expected peak positions of the Al_3Ni phase are indicated with black lines. It becomes evident that diffraction peaks of all lattice planes are present. Therefore, crystals with various orientations contribute to the diffractogram. In the case of a strongly textured compound, particular diffraction would not be present. This was also found for Al_9Ni_2. The diffracted intensity as a function of the 2θ and azimuthal angle is shown in Figure A.14 (b). There is an almost constant intensity of the Al_3Ni diffraction rings along the azimuthal angle. Variations are attributed to variable background intensity. This proves that the crystals are randomly rotated relative to the incoming X-ray beam direction. Both observations provide strong indications that the orientations of the Al_3Ni crystals are randomly distributed. The detailed evaluation of the components of equation A.1 leads to the conclusion that under the conditions outlined in Section 3.2.1 the variation of the intensity is negligible. The variation of the individual factors is in the range of 0.1 – 1.1%, which is well below the experimental error. In this context, a linear correlation between diffracted intensity and the amount of phase is a valid assumption.

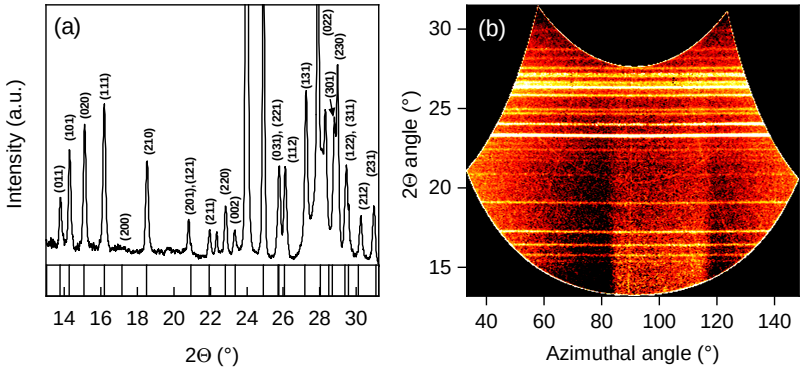

Figure A.14: X-ray diffraction of a 10 at.% Ni Al/Ni sample after isothermal heating at 276 °C. (a) The diffractogram reveals the presence of all Al_3Ni diffraction peaks. (b) With respect to the background noise, the X-ray intensity is evenly distributed over the azimuthal angle.

A.6 Master plots in kinetic analysis

Master plots are used to compare kinetic data generated under various experimental conditions. For example, master plots allow a direct comparison of isothermal and continuous heating experiments. This approach is helpful to select an appropriate kinetic model for a given solid-state transformation. Generally, extracting the kinetic parameters based on a single experimental data set is prone to errors. If multiple isothermal and non-isothermal heating experiments are used, the reliability of the extracted kinetic data is considerably improved. A common approach for master plots was introduced by *Gotor et al.* [138]. Kinetic data based on arbitrary temperature profiles can be compared. There are two ways of representing kinetic equations: (i) in the integral form $g(\alpha)$ or (ii) in the differential form $f(\alpha)$ where α is the extent of conversion. The latter one is the derivative of the integral form and can be interpreted as the rate of reaction. [73, 138]

Master plots in the differential form $f(\alpha)$

In the case of the differential form, the experimental data and the kinetic equations are generalized by using a reference point at $\alpha = 0.5$ and the concept of the generalized time ϑ. The generalized time is defined by

$$\vartheta = \int_0^t exp\left(\frac{E_a}{RT}\right) dt \tag{A.6}$$

where E_a is the activation energy, R the universal gas constant and T the absolute temperature. The combination between the general equation for the reaction rate of equation 2.21 and the equation A.6 allows to deduce the reduced-generalized reaction rate $(d\alpha/d\vartheta)/(d\alpha/d\vartheta)_{\alpha=0.5}$. To calculate the reduced-generalized reaction rate directly from the experimental data the equation

$$\frac{d\alpha/d\vartheta}{(d\alpha/d\vartheta)_{\alpha=0.5}} = \frac{d\alpha/dt}{(d\alpha/dt)_{\alpha=0.5}} \frac{exp(E_a/RT)}{exp(E_a/RT_{0.5})} \tag{A.7}$$

is used. Here, $T_{0.5}$ is the temperature at $\alpha = 0.5$. Equation A.7 is valid for an arbitrary temperature profile. In case of isothermal heating $T = T_{0.5}$ and the reduced-generalized reaction rate can be directly derived from $d\alpha/dt$ versus α. Accordingly, the kinetic equations listed in Table 2.2 can be transformed into $(d\alpha/d\vartheta)/(d\alpha/d\vartheta)_{\alpha=0.5}$ by applying

$$\frac{d\alpha/d\Theta}{(d\alpha/d\Theta)_{\alpha=0.5}} = \frac{f(\alpha)}{f(0.5)} \tag{A.8}$$

Master plots in the integral form $g(\alpha)$

In case of the intergral form the generalized time $\vartheta/\vartheta_{0.5}$ or $g(\alpha)/g(0.5)$ is plotted versus the extent of conversion. Both can be used equivalent from each other according to equation

$$\frac{\vartheta}{\vartheta_{0.5}} = \frac{g(\alpha)}{g(0.5)} \tag{A.9}$$

In the integral case, two different equations are used for isothermal heating and linear heating. In the isothermal case, the equation

$$\frac{g(\alpha)}{g(0.5)} = \frac{t}{t_{0.5}} \tag{A.10}$$

can be applied, where $t_{0.5}$ is the time at $\alpha = 0.5$. For linear heating $\vartheta/\vartheta_{0.5}$ can be calculated by

$$\frac{\vartheta}{\vartheta_{0.5}} = \frac{p(x)}{p(x_{0.5})} \tag{A.11}$$

whereas $p(x)$ cannot be expressed in a closed form. However, $p(x)$ can be approximated by applying

$$p(x) = \frac{e^{-x}}{x}\pi(x) \tag{A.12}$$

and

$$\pi(x) = \frac{x^3 + 18x^2 + 86x + 96}{x^4 + 20x^3 + 120x^2 + 240x + 120} \tag{A.13}$$

With this set of equations the kinetic experimental data and the kinetic equations can be converted into a generalized form.

A.7 STEM investigations of Al/Ni multilayers heated close to the runaway temperature

Complementary to the XRD experiments presented in Figure 4.37, electron microscopic investigations were performed. For this purpose, FIB cross-sections of the Al/Ni samples were produced. In Figure A.15 the STEM images of as-deposited (a) and a quenched sample (b) were compared. In both cases a Al/Ni multilayer sample with Λ = 166 nm was used. In the case of the quenched sample, the multilayer stack was heated to 412 °C which is close to the ignition temperature. The bright layers represent Ni, whereas the dark layers represent Al. Nucleation would be apparent by a change in the phase contrast, especially at the Al/Ni interfaces, which are known as preferred sites for phase formation.

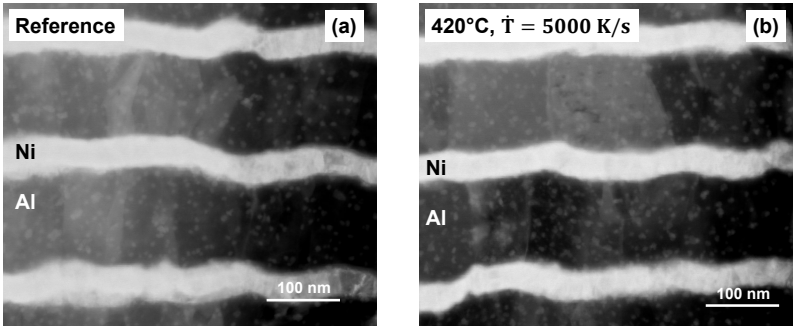

Figure A.15: STEM images of FIB cross-section of a Λ = 166 nm Al/Ni mulitlayer sample in the (a) as-deposited state and (b) after quenching close to the igntion temperature (T_{quench} = 412 °C). There are no indications for intermetallic product phase formation detectable.

However, there are no indications for the formation of intermetallic phases neither in the as-deposited state nor in the quenched state. This is in good agreement with the findings from the XRD investigations shown in Figure 4.37. The origin of the small spots within the Al layer could not be clearly identified. Whereas electron microscopy gives some evidence that the spots are copper-containing phases, XRD cannot confirm this observation. No peaks of copper phases were found in the diffractograms. However, the analysis shows that the density, as well as the shape, are not influenced by heating. Therefore, we conclude that they do not contribute to the reaction.